

UNCLASSIFIED

AD NUMBER

AD482170

LIMITATION CHANGES

TO:

Approved for public release; distribution is unlimited.

FROM:

Distribution authorized to U.S. Gov't. agencies and their contractors; Critical Technology; MAY 1966. Other requests shall be referred to Air Force Aero Propulsion Laboratory, Wright-Patterson AFB, OH 45433. This document contains export-controlled technical data.

AUTHORITY

AFAPL ltr, 29 Nov 1968

THIS PAGE IS UNCLASSIFIED

AFAPL-TR-65-107

THE MHD INDUCTION MACHINE

Edward S. Pierson

William D. Jackson

MASSACHUSETTS INSTITUTE OF TECHNOLOGY

Research Laboratory of Electronics

Cambridge, Massachusetts

TECHNICAL REPORT No. AFAPL-TR-65-107

May 1966

Air Force Aero Propulsion Laboratory
Research and Technology Division
Air Force Systems Command
Wright-Patterson Air Force Base, Ohio

482170

NOTICES

When Government drawings, specifications, or other data are used for any purpose other than in connection with a definitely related Government procurement operation, the United States Government thereby incurs no responsibility nor any obligation whatsoever; and the fact that the Government may have formulated, furnished, or in any way supplied the said drawings, specifications, or other data, is not to be regarded by implication or otherwise as in any manner licensing the holder or any other person or corporation, or conveying any rights or permission to manufacture, use, or sell any patented invention that may in any way be related thereto.

NOTICE: This document is subject to special export controls and each transmittal to foreign governments or foreign nationals may be made only with the prior approval of the Aerospace Power Division, Air Force Aero Propulsion Laboratory, Wright-Patterson AFB, Ohio.

The distribution of this report is limited because it contains technology identifiable with items on the Strategic Embargo Lists excluded from export or re-export under U. S. Export Control Act of 1949 (63STAT. 7), as amended (50 USC APP 2020.2031), as implemented by AFR 400-10.

Copies of this report should not be returned to the Research and Technology Division unless return is required by security considerations, contractual obligations, or notice on a specific document.

AFAPL-TR-65-107

THE MHD INDUCTION MACHINE

Edward S. Pierson

William D. Jackson

MASSACHUSETTS INSTITUTE OF TECHNOLOGY

Research Laboratory of Electronics

Cambridge, Massachusetts

TECHNICAL REPORT No. AFAPL-TR-65-107

May 1966

NOTICE: This document is subject to special export controls and each transmittal to foreign governments or foreign nationals may be made only with the prior approval of the Aerospace Power Division, Air Force Aero Propulsion Laboratory, Wright-Patterson AFB, Ohio.

Air Force Aero Propulsion Laboratory
Research and Technology Division
Air Force Systems Command
Wright-Patterson Air Force Base, Ohio

FOREWORD

This report was prepared by the Research Laboratory of Electronics of Massachusetts Institute of Technology under U. S. Air Force Contract No. AF33(615)-1083. The contract was initiated under Project 5350, "Plasma Dynamics," Task No. 535004, "Magnetohydrodynamics." The work was administered under the direction of the Air Force Aero Propulsion Laboratory, Research and Technology Division, 1/Lt Robert R. Barthelemy, task engineer.

This report is based on an Sc.D. thesis, Department of Electrical Engineering, Massachusetts Institute of Technology, by one of the authors (Edward S. Pierson), submitted in August 1965.

This technical report has been reviewed and approved.

ABSTRACT

The magnetohydrodynamic (MHD) induction machine is analyzed to determine the terminal properties, the power flow relations, and the steady-state performance characteristics. The theory for a machine of infinite length and width is first developed, including velocity-profile effects. Solutions are obtained for laminar (Hartmann) flow in a narrow channel, and numerical results are presented for the arbitrary-channel case. Turbulent flow is treated by using a boundary-layer theory. The influence of finite length on generator performance is also considered. In each case considered, results are presented in terms of the electrical efficiency and the power density.

The performance and design implications of the results are discussed for several examples of MHD induction generators operated on liquid-metal flows. We conclude that over-all efficiencies in the range 70-85% may be attained in practical high-power generators, but that it may not be possible to achieve the lower efficiency limit at power levels below approximately 1 megawatt.

TABLE OF CONTENTS

List of Figures	vii
List of Tables	x
Nomenclature	xi
I. INTRODUCTION	1
1.1 Description	1
1.2 Field Interaction	2
1.3 Historical Background	5
1.4 Object and Scope of This Investigation	7
II. EQUATIONS OF INDUCTION-COUPLED FLOW	9
2.1 Introduction	9
2.2 Equations	10
2.3 Exciting-Coil Terminal Voltage	14
2.4 Powers	16
III. CONSTANT FLUID VELOCITY	19
3.1 Electromagnetic Fields	19
3.2 Electrical Impedance	21
3.3 Powers	28
3.4 Skin Effect	30
3.5 Odd Excitation	32
3.6 Comparison of Even and Odd Excitation	33
3.7 Electromagnetic Field and Pressure-Gradient Profiles	37
3.8 Unbalanced Excitation	41
IV. LAMINAR FLOW	46
4.1 Introduction	46
4.2 Approximate Equations for Laminar Flow	46
4.3 Slit-Channel Solution	51
4.4 Electromagnetic Fields and Powers for a Known Velocity	55
4.5 Velocity Profile for a Known Pressure Gradient	59
4.6 An Iterative Solution	65
V. TURBULENT FLOW	71
5.1 Experimental Turbulent Hydrodynamic Velocity Profiles	71
5.2 Turbulence and DC Magnetic Fields	75
5.3 Turbulence and Traveling Electromagnetic Fields	76
5.4 Laminar Boundary-Layer Theory	78
5.5 Turbulent Boundary-Layer Theory	82

CONTENTS

VI.	THE MACHINE OF FINITE LENGTH	87
6.2	Introduction	87
6.2	Transformed Potentials	88
6.3	The Ideal Core – Fields and Impedance	91
6.4	The Ideal Core – Powers	95
6.5	Lossless-Core Machine	106
6.6	Extensions	109
VII.	DISCUSSION OF GENERATOR PERFORMANCE	110
7.1	The Model	110
7.2	Optimum Operating Regime	111
7.3	Comparison of Liquid Metals and Plasmas	112
7.4	High-Power Generator	113
7.5	Medium-Power Generator	116
VIII.	CONCLUDING REMARKS AND SUGGESTIONS FOR FURTHER STUDY	120
8.1	Concluding Remarks	120
8.2	Theoretical Extensions	120
8.3	Experimental Extensions	121
APPENDIX A	Continuity of the Tangential Electric Field in MHD Machines	122
APPENDIX B	Field Solution Retaining All Components of the Vector Potential	127
APPENDIX C	Exciting Winding of Finite Thickness	130
APPENDIX D	Viscous Power Loss	134
APPENDIX E	Numerical Methods	141
APPENDIX F	Inverse Transform	147
APPENDIX G	Conducting Channel Walls and Insulators of Finite Thickness	149
References		154

List of Figures

	<u>Page</u>
Fig. 1. Flat linear MHD induction machine.	1
Fig. 2. Vector diagram for a series RL circuit.	3
Fig. 3. Magnetic fields seen by the fluid.	3
Fig. 4. Equivalent circuit for fluid.	4
Fig. 5. Vector diagram for fluid.	4
Fig. 6. Vector diagram for pump operation.	4
Fig. 7. Vector diagram for generator operation.	5
Fig. 8. The Model.	9
Fig. 9. Steps in calculating the coil terminal voltage.	15
Fig. 10. Series resistance of the slit-channel machine as a function of s and R_{Ma} .	23
Fig. 11. Series inductance of the slit-channel machine as a function of s and R_{Ma} .	23
Fig. 12. Series resistance as a function of s and R_{Ma} .	24
Fig. 13. Series inductance as a function of s and R_{Mc} .	25
Fig. 14. Equivalent circuits.	26
Fig. 15. Normalized powers for a slit-channel machine with constant-current excitation as a function of s .	29
Fig. 16. Series resistance for even and odd excitation with $\kappa = 0$ as a function of sR_M and α .	35
Fig. 17. Series resistance for even and odd excitation with $\kappa = 1$ as a function of sR_M and α .	35
Fig. 18. Series inductance for even and odd excitation with $\kappa = 0$ as a function of sR_M and α .	36
Fig. 19. Series inductance for even and odd excitation with $\kappa = 1$ as a function of sR_M and α .	36
Fig. 20. Q for even and odd excitation with $\kappa = 0$ as a function of sR_M and α .	37
Fig. 21. Q for even and odd excitation with $\kappa = 1$ as a function of sR_M and α .	37
Fig. 22. Vector potential normalized to 1 at $y = a$ versus $\frac{y}{a}$.	39
Fig. 23. Electromagnetic-pressure gradient normalized to 1 at $y = a$ versus $\frac{y}{a}$.	39
Fig. 24. Vector potential normalized to 1 at $y = a$ versus $\frac{y}{a}$ (semilog scale).	40
Fig. 25. Series resistance of single-phase, slit-channel machine for $R_{Ma} = 1.0$.	44
Fig. 26. Series resistance of single-phase, slit-channel machine for $R_{Ma} = 10.0$.	45

List of Figures (continued)

	Page
Fig. 27. Normalized Hartmann velocity profiles.	52
Fig. 28. F_m for Hartmann profile.	54
Fig. 29. F_r for Hartmann profile.	54
Fig. 30. Generator efficiency for slit-channel machine with Hartmann profile.	55
Fig. 31. Comparison of velocity-profile solutions by two methods.	62
Fig. 32. Comparison of velocity-profile solution with Hartmann profile, $\alpha = 1$.	64
Fig. 33. Pump velocity profiles.	65
Fig. 34. Comparison of initial and final iterative solutions.	66
Fig. 35. Iterative solution for velocity, $\alpha = 1$, $R_M = 1$, FOR = 1000.	67
Fig. 36. Iterative solution for velocity, $\alpha = 1$, $R_M = 10$, FOR = 100.	68
Fig. 37. Iterative solution for velocity, $\alpha = 10$, $R_M = 1$, FOR = 1000.	69
Fig. 38. Iterative solution for velocity, $\alpha = 10$, $R_M = 1$, FOR = 10000.	70
Fig. 39. OHD turbulent velocity profiles.	72
Fig. 40. Slit-channel generator efficiency for $\left(\frac{1}{n}\right)^{th}$ -power law turbulent profile.	74
Fig. 41. Theoretical MHD turbulent velocity profiles of Harris.	76
Fig. 42. Model for boundary-layer analysis.	80
Fig. 43. $\frac{\delta^*}{a}$ as a function of R_e and M .	84
Fig. 44. Friction factors, $M = 50$.	86
Fig. 45. Friction factors, $M = 100$.	86
Fig. 46. Friction factors, $M = 500$.	86
Fig. 47. The Model.	89
Fig. 48. Finite-length, ideal-core, series-equivalent resistance and inductance for cosine coils versus n : (a) for $s = -0.01$, $R_M = 10$, $\alpha = 0.1$; (b) for $s = -0.2$, $R_M = 10$, $\alpha = 0.1$; (c) for $s = -0.5$, $R_M = 10$, $\alpha = 0.1$; (d) for $s = -1$, $R_M = 10$, $\alpha = 0.1$; (e) for $s = -1.0$, $R_M = 0.1$, $\alpha = 0.1$.	96, 97
Fig. 49. Fine-length, ideal-core, P_s and e_g versus n : (a) for $s = -0.05$, $R_M = 10$, $\alpha = 0.1$; (b) for $s = -0.2$, $R_M = 10$, $\alpha = 0.1$; (c) for $s = -0.5$, $R_M = 10$, $\alpha = 0.1$; (d) $s = -0.2$, $R_M = 1$, $\alpha = 0.1$; (e) for $s = -1$, $R_M = 0.1$, $\alpha = 0.1$; (f) P_m vs n for $s = -0.2$, $\alpha = 0.1$, $R_M = 10$ and 1 .	102, 103
Fig. 50. Graph of Eq. 217.	106
Fig. A-1. The Model.	123
Fig. C-1. $F_D F_D^*$ as a function of α_e for four sets of machine parameters.	132

List of Figures (continued)

	<u>Page</u>
Fig. D-1. Forces acting on a fluid volume extending across the channel of depth c .	134
Fig. D-2. Forces and stress acting on an elemental volume of fluid centered at (x,y,z) .	136
Fig. D-3. Viscous power loss for Hartmann profile as a function of M .	137
Fig. F-1. Sketch of poles and contours for inverse transform.	148
Fig. G-1. The Model.	150

List of Tables

	<u>Page</u>
Table 1. Electromagnetic fields for a constant fluid velocity.	21
Table 2. Multiplicative constants for vector potential and electromagnetic pressure-gradient profiles, for $ sR_M = 1$, $\kappa = 0$, and $R_{Mc} = 0$.	41
Table 3. Numerical integration results for the electromagnetic fields and powers, varying α , $\kappa = 0$.	57
Table 4. Comparison of slit-channel theory and numerical results, $ \gamma a = 1.4$, $\kappa = 0$.	58
Table 5. Numerical integration results for the electromagnetic fields and powers, varying \bar{s} , $\alpha = 1$, $\kappa = 0$.	59
Table 6. Numerical integration results for the electromagnetic fields and powers, varying \bar{s} , $\alpha = 3$, $\kappa = 0$.	60
Table 7. Iterative solution results, $\kappa = 0$.	69
Table 8. Turbulent velocity-profile information.	73
Table 9. Slit-channel generator efficiencies.	75
Table 10. δ , δ^* , and τ_0 for a laminar boundary layer.	82
Table 11. Powers attributable to finite machine length.	99
Table 12. Total powers and efficiencies for a generator 6 wavelengths long.	104
Table 13. Mechanical power coefficients from Table 11 for $\alpha = 0.1$.	105
Table 14. Roots of Eq. 217 or Fig. 50.	107
Table 15. Liquid-metal and plasma properties.	112
Table 16. High-power generator designs.	117
Table 17. Medium-power generator designs.	118
Table 18. End and profile factors, and friction factors for medium-power generators.	119
Table E. 1. Numerical solution tests of Eq. 127.	144
Table E. 2. Numerical integration tests of Eq. 133, 100 points.	145

NOMENCLATURE

Rationalized mks units are used. An arrow above a symbol indicates a vector, underlining indicates complex amplitude; *, complex conjugate; ||, magnitude or absolute value; <>, time average; and a bar above, space average. The common subscripts are f, c, e, i, and w for fluid, core, exciting winding, insulator, and channel-wall variables; and x, y, and z for the components of a vector. Variables used in a single section may not be included.

Symbol	Definition
A	Vector potential, Eq. 6
A_{fo}	Vector potential at center of channel
A'_{fo}	$A_{fo}/\mu_f N I a$
B	Magnetic flux density
D_h	Hydraulic diameter, Eq. 164
\underline{DF}	Normalized derivative of vector potential, Eq. 149
E	Electric field intensity
\underline{F}	Normalized vector potential, $\underline{A_f}/\underline{A_{fo}}$
F_D	Derating factor for vector potential, Appendices C and G
F_m	Profile factor for P_m , Eq. 141
F_r	Profile factor for P_r , Eq. 142
FOR	Force multiplier, Eq. 162
I	Exciting-current amplitude
J	Current density
K	Surface current density
L_o	Normalization constant for coil inductance, Eq. 49
L_p	Parallel-equivalent circuit inductance of coil
L_s	Series-equivalent circuit inductance of coil
L_{so}	Series-equivalent circuit inductance of coil for odd excitation
M	Hartmann number, Eq. 126
N	Turns-density amplitude
P_c	Power dissipated in core
P_e	Power dissipated in exciting winding
P_m	Mechanical power output
P_o	Normalization constant for powers, Eq. 70
P_r	Power dissipated in fluid because of finite conductivity
P_s	Power supplied to fluid by exciting system
P_v	Power dissipated in fluid owing to viscosity
Q	Quality factor
Q	Volume flow rate

R_e	Internal resistance of exciting coil, Eq. 50
R_e	Reynolds number, $R_e = \rho \bar{v} D_h / \eta$
R_M	Magnetic Reynolds number in fluid, $R_M = \mu_f \sigma_f v_s / k$
R_{Mc}	Magnetic Reynolds number in core $R_{Mc} = \mu_c \sigma_c v_s / k$
R_{MF}	Magnetic Reynolds number based on fluid velocity, $R_{MF} = \mu_f \sigma_f v / k$
$R_{M\alpha}$	Magnetic Reynolds number for slit-channel machine, $R_{M\alpha} = \left(\frac{1}{1+\kappa} \right) R_M$
R_o	Normalization constant for coil resistance, Eq. 49
R_p	Parallel-equivalent circuit resistance of coil
R_s	Series-equivalent circuit resistance of coil
R_{so}	Series-equivalent circuit resistance of coil for odd excitation
S	Poynting's vector
V	Coil terminal voltage
X_e	Leakage reactance of exciting coil
Z	Coil impedance
a	Channel half-height
b	Thickness of exciting plate
c	Machine width
e	Efficiency
e_g	Generator efficiency
e_p	Pump efficiency
f	Friction factor, Eq. D. 18
i	Order of pole for finite-length solution
\vec{i}	Unit vector
j	$\sqrt{-1}$
k	Wave number
n	Length of machine of direction of fluid flow in wavelengths
p	Pressure
p	Transform variable (Section VI)
p_{em}	Electromagnetic part of the pressure
p_o	Time-average pressure gradient
q	Electric charge density
s	Slip based on phase velocity, $s = \frac{v_s - v}{v_s}$
t	Time
u	Normalized fluid velocity, v/\bar{v}
v	Fluid velocity
v_s	Field phase velocity, $v_s = \frac{\omega}{k}$
x	Axis in direction of fluid flow
y	Axis transverse to flow

\tilde{y}	Normalized axis, y/a
y_1	$y + a$
z	Axis in direction of current flow
α	Ratio of channel width to excitation wavelength, $\alpha = ak$
γ	Spatial constant in fluid, $\gamma^2 = 1 + jsR_M$
δ	Spatial constant in core, $\delta^2 = 1 + jR_{Mc}$
δ	Boundary layer thickness (sections 5.4, 5.5)
δ^*	Displacement thickness, Eq. 178
δ_s	Electrical skin depth (Section III)
ϵ	Permittivity
η	Absolute viscosity
θ	Power-factor angle
κ	Ratio of fluid to core permeability, $\kappa = \frac{\mu_f}{\mu_c}$
λ	Wavelength
μ	Permeability
μ_o	Permeability of free space
ρ	Fluid mass density
σ	Electrical conductivity
σ	Surface charge density (Appendix A)
σ_s	Surface conductivity
τ	Shear stress caused by fluid viscosity
τ_o	Wall shear stress
ϕ	Scalar potential, Eq. 7
ω	Frequency in radians per second
∇	Vector differential operator
Δ_i	$\Delta_i = 2$ for $i \neq 0$, and 1 for $i = 0$

1. INTRODUCTION*

1.1 DESCRIPTION

The MHD induction machine, shown schematically in Fig. 1, consists of a channel containing a flowing electrically conducting fluid and a set of exciting windings that produce a traveling magnetic field. Currents are induced in the fluid because of the relative motion between the field and fluid. The force of electrical origin, on account of the interaction of the magnetic field and the fluid current, is always in a direction such that the fluid tends to travel at the same velocity as the field. If the fluid velocity v is less than the field phase velocity v_s , the force accelerates the fluid, energy is transferred to the fluid, and the device acts as a pump or accelerator. If v is greater than v_s , the force opposes the motion and the machine is a generator, converting mechanical energy to electrical energy. If v and v_s are in opposite directions, the machine is a flow damper, absorbing both mechanical and electrical energy. At synchronous speed, $v = v_s$, there is no relative motion of the fluid and field, and consequently no interaction.

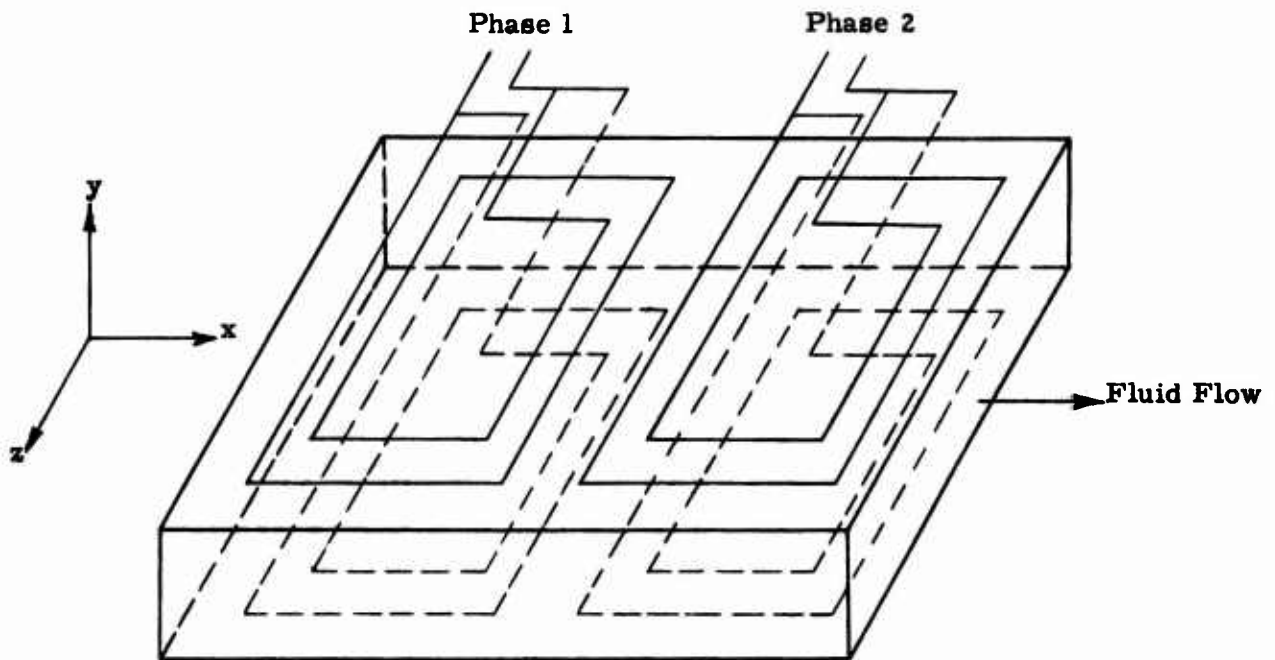


Fig. 1. Flat linear MHD induction machine

*Manuscript released by authors May 1, 1965 for publication as an RTD Technical Documentary Report.

There is no direct electrical connection to the fluid, so that all fluid currents are due to a combination of transformer and motional induction. The effect of the fluid is detected from the electrical terminals only by the change in the electrical impedance, or equivalently, the electromagnetic fields. If there is to be an appreciable energy transfer relative to the stored magnetic energy, which is required for high efficiency, the induced magnetic field attributable to the fluid currents must be comparable with the applied magnetic field. Approximate solutions for the magnetic field or complete neglect of the induced field are not valid. The real part of the terminal impedance, representing the energy transfer to or from mechanical form, is negative for operation as a generator. The imaginary part is always inductive, requiring external capacitive energy storage.

The description above is exact for a conventional rotation induction machine.^{1, 2} Consequently, previous knowledge of the rotating version can be applied to the MHD version, with appropriate modifications for the fluid and geometry. The fluid is more complex because the velocity is not a constant, and there are additional losses resulting from viscosity. The geometry is similar to linear induction motors³ or induction motors with arc-shaped stators (a stator occupying only a fraction of the rotor periphery⁴), and shares with them the distortion of the electromagnetic fields at the entrance and exit regions to the traveling-field structure. The MHD version is both harder to analyze and less efficient.

1.2 FIELD INTERACTION

Examination of the electromagnetic fields provides a better picture of the principles of operation of the MHD induction machine. The traveling magnetic field is broken up into two components, the applied field set up by the exciting winding, and the reaction field resulting from the induced currents in the fluid. The reaction field, opposing the change in the applied field, is a traveling wave displaced in space and time from the applied field. The relative location of the two waves explains both the direction of the force on the fluid and the negative resistance obtained for generator operation.

First consider the vector diagram for a series RL circuit with sinusoidal excitation (Fig. 2) as an aid in explaining the phase differences that arise. The total voltage is the sum of the voltages across the resistor and inductor. That across the resistor is in phase with the current, while the inductor voltage,

$$\underline{V_L} = j\omega L \underline{I}, \quad (1)$$

leads the current by 90°, with complex notation used. The total voltage leads the current by an angle less than 90°, and the magnetic field is in phase with the current. If the total voltage and current are more than 90° out of phase, the apparent resistance is negative.

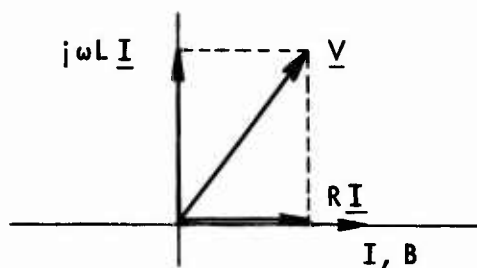


Fig. 2. Vector diagram for a series RL circuit.

The reaction field set up by the fluid must be determined in the frame fixed with respect to the fluid. For pump operation, $v < v_s$, the applied field resulting from the exciting winding, as seen by the fluid, moves in the positive x-direction with the velocity $v_s - v$ (Fig. 3). The time rate of change of the applied field causes an induced voltage in the fluid. If inductive effects in the fluid are neglected, the induced current is in phase with the induced voltage and creates a magnetic field to oppose the change in the applied magnetic field. The fluid magnetic field must be a maximum when the time rate of change of the applied field is a maximum or, as shown in Fig. 3, it lags the applied field by 90° in space. Of course, the inductive effects associated with the fluid are not negligible, so that the current and reaction field lag the applied field by more than 90° but less than 180° .

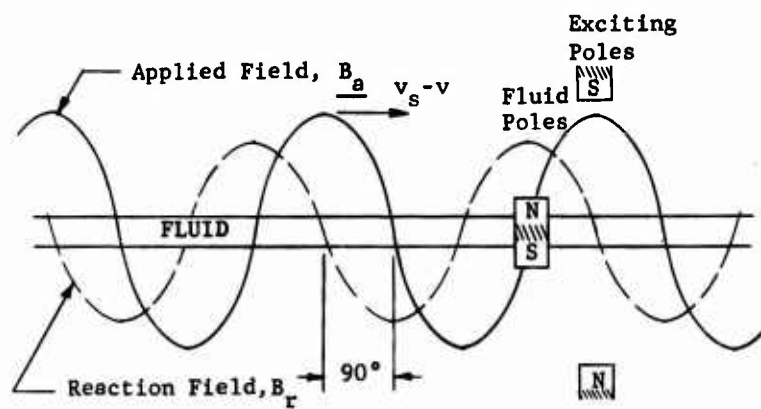


Fig. 3. Magnetic fields seen by the fluid.

The same result is obtained by thinking of the fluid as a short-circuited series RL circuit with an induced voltage that is due to the time rate of change of the applied magnetic field (Fig. 4). The induced voltage leads the applied field B_a by 90° in time (Fig. 5). The current lags the voltage, because of the inductance, as in Fig. 2, and is 180° out of phase because it flows out of the positive terminal of the inductor (the

induced voltage is internal to the inductance). Thus the reaction field \underline{B}_r lags the applied field by $90^\circ - 180^\circ$ in time. For an observer fixed with respect to the fluid, the time lag is equivalent to the space lag obtained above.

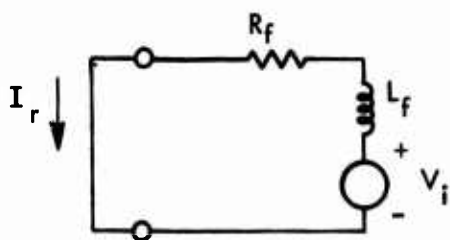


Fig. 4. Equivalent circuit for fluid.

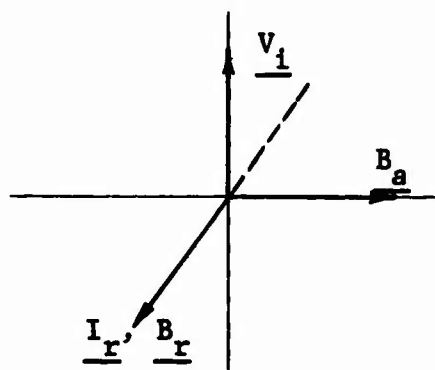


Fig. 5. Vector diagram for fluid.

Now the force and energy transfer for pump operation can be explained. The force between the two magnetic fields is in the direction to align them; it pulls the fluid along with the field or accelerates it. This is seen from the equivalent magnetic poles, shown in Fig. 3. There is an equal and opposite force on the stationary exciting system. The fluid magnetic field in the fixed frame still appears to lag the applied field by more than 90° in space, or, as seen by a fixed coil, by the same angle in time. The vector diagram for the pump (Fig. 6) shows that \underline{B}_r is in the third quadrant and its voltage \underline{V}_r , leading the flux by 90° , is in the fourth. The fluid interaction appears as an additional positive resistance in the exciting system and absorbs power.

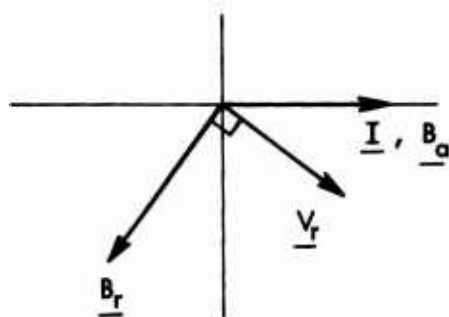


Fig. 6. Vector diagram for pump operation.

For the generator, $v > v_s$, there is only one change. The applied field, as seen by the fluid, moves in the negative x-direction with velocity $v - v_s$. The reaction field still lags the applied field, but now it is on the opposite side of the applied field. Therefore the force to align the fields acts in the opposite direction, as required for generator operation. The reaction field in the fixed frame is also on the opposite side of the applied field, or now leads it by an angle of $90^\circ - 180^\circ$. As shown in Fig. 7, this puts the reaction field in the second quadrant and its voltage in the third. The induced voltage appears from the coil terminals as a negative resistance, or supplies power to the source.

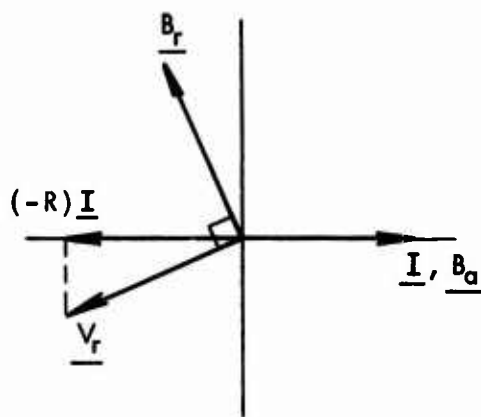


Fig. 7. Vector diagram for generator operation.

1.3 HISTORICAL BACKGROUND

The earliest application of MHD was Faraday's attempt, in 1831, to measure the voltage induced in the River Thames by its motion in the earth's magnetic field.⁵ The measurement was unsuccessful, because of polarization of the electrodes. Northrup,⁶ from 1906 and 1910, studied experimentally the interaction of a current and a magnetic field in a liquid conductor. He found that the passage of a current through mercury in an open tray caused a V-shaped depression to form in the center. Northrup mentions the use of this phenomenon for measuring large currents and achieving motion without the use of brushes or slip rings. With the work of Kolin,⁷ in 1936, the electromagnetic flowmeter (an open-circuited conduction generator producing a voltage proportional to flow rate) became the first important application of MHD. It was originally applied to blood-flow measurements, and later to the flow of liquid metals and other conducting fluids, using conduction devices.^{8,9}

An induction pump was first proposed by Chubb,¹⁰ in 1915, to pump a liquid metal by means of a rotating magnetic field in a spiral-channel induction pump. A refrigerator using sodium-potassium and a gas with an annular induction pump for the motor

was suggested, in 1928, by Einstein and Szilard.¹¹ They also suggested an annular traveling-field pump for use with alkali metals.

The development of the electromagnetic pump proceeded slowly until the need for pumps to handle liquid metals for cooling nuclear reactors created considerable interest.^{12, 13} The theory of the conduction pump (and generator) is well understood,^{14, 15} and effort has been devoted to consideration of end effects, boundary layers, turbulence, and compressibility. The theory of the induction pump, since exact solutions are not possible, is not as well developed. Design procedures based on a combination of theory, experiment, and experience from conventional rotating induction machines have been used with moderate success by Baker,¹⁶ Barnes,¹⁷ and Watt.¹⁸ This basic analysis has been extended by a number of authors^{19, 20} to include approximate velocity profiles and more detailed experimental and theoretical results, but with no apparent improvement in pump design. The efficiencies obtained are all under 50%, too low to be acceptable if the pump were to be used for power generation. Both conduction and induction pumps are commercially available.^{21, 22}

Okhremenko²³ has considered induction pumps in more detail, including: velocity profiles; the fluid entrance to a uniform traveling field; and the transient in the fluid velocity when the pump is turned on. His velocity-profile solution is approximate, assuming the profile does not modify the field; and he uses the first two terms of an unspecified power series for the profile, corresponding to the slit-channel solution of section 4.3 plus a correction term. The numerical solution of section 4.5 is probably just as simple. His entrance solution is for the velocity profile assuming a step in the electromagnetic field, whereas the important effect is the deviation in the electromagnetic field from a step.

Two theoretical studies lead up to the present investigation. Harris²⁴ studied induction-driven flows, obtaining the approximate one-dimensional velocity profile when the channel height is much less than the pole spacing (a slit channel). He also investigated the power flow in the induction machine and extended his work on turbulence to induction-driven flows. Penhune²⁵ examined the internal behavior of laminar induction-driven flows in more detail. He converted the nonlinear differential equations to an infinite set of coupled linear differential equations and solved them approximately by numerical methods. Velocity and magnetic field profiles were obtained, but power flow and terminal properties of the machine were not considered.

Concurrently with this theoretical study, two experiments have been undertaken. Reid,²⁶ using a coil system designed by Hoag²⁷ for a plasma pump, measured a small interaction with eutectic sodium-potassium alloy (NaK). A new machine, designed specifically for use with the NaK flow loop by Porter,²⁸ is now under construction. It is expected to give a larger interaction and reasonable confirmation to the theoretical results.

Considerable attention has been devoted recently to induction generators, primarily aimed at using plasmas. Most of the analyses are valid only for $sR_M \ll 1$,* which will be shown to be an impractical operating regime for energy conversion, and are restricted to an inviscid and incompressible fluid. Also, they have not determined the machine properties and the conditions for best operations, which clearly show that a plasma is not practical in an induction generator unless higher conductivities are obtainable.²⁹

Fischbeck³⁰ obtained an approximate solution for an incompressible, inviscid fluid in a slit channel, and two solutions for different models of a compressible fluid. He did not sufficiently consider the implications of his assumptions or the interpretation of his results. Fanucci et al.³¹ have made a comprehensive study of the induction generator, including an experiment.³² The theory considers compressibility and finite length, but not the basic properties necessary to design a practical machine, and is restricted to $sR_M \ll 1$. The experimental power flow was small.

Lyons and Turcotte³³ have analyzed the induction pump, using $sR_M \ll 1$ and assuming a magnetic field that is an infinitely long, exponentially damped sine wave, certainly a poor approximation to a machine of finite length. Their results for a finite-length machine differ significantly from the present investigation. Sudan³⁴ has treated the machine of finite length essentially as we have, but has not carried the interpretation through. Peschka, Kelm, and Engeln³⁵ considered the finite-length machine, but their results are also significantly different from the present study, and their paper does not include sufficient information to determine the source of this difference.

Neuringer and Migotsky³⁶ have considered skin effect with odd excitation, and conclude that skin effect is responsible for the presence of a peak in the power curves. This is treated in detail in section 3.4, and shown to be due to the reaction field of the fluid but to differ from skin effect. Lengyel³⁷ has considered a vortex-type generator geometry, using the usual inviscid incompressible fluid with a series solution in sR_M .

1.4 OBJECT AND SCOPE OF THIS INVESTIGATION

The objectives of this investigation are to extend the work of Harris and Penhune by providing a clear picture of the terminal properties of and power flow in the MHD induction machine based on practical fluid properties and machine parameters. The effects of velocity profiles, viscosity, the finite length of the machine, and the loss in setting up the excitation are included in the analysis. The scope is restricted to apply only to incompressible fluids. The analysis shows that liquid metals will provide reasonable efficiency and power density, but plasmas will not as the conductivity is too low.

* sR_M , the magnetic Reynolds number, based on the velocity difference $v_s - v$ and the wavelength, indicates the magnitude of the field-fluid interaction. The case $sR_M \ll 1$ means that the field induced in the fluid is negligible.

The basic equations for the induction machine are developed in Section II without application to a specific model for the fluid. Constant fluid velocity is considered in Section III, including a comparison of even and odd excitation and a discussion of unbalanced excitation. The constant fluid velocity allows an analytical solution to be obtained. This solution points out the major properties, the electromagnetic behavior, without consideration of the fluid. This restriction is removed in Section IV and an approximate solution is obtained for laminar flow. The velocity profile may have a large effect on the machine performance, the effect depending on the parameters. Turbulent flow is treated in Section V, but this is limited by the lack of experimental information. Boundary-layer theory presents a useful approach to handling turbulent flow.

The machine of finite length is considered in Section VI. The finite length decreases the power level of the machine, but has little effect on the efficiency for a machine several wavelengths long. The previous results are used in Section VII to examine the induction generator with practical fluid properties.

II. EQUATIONS OF INDUCTION-COUPLED FLOW

2.1 INTRODUCTION

The basic theory used to determine the performance of the induction machine is developed here without application to a specific model for the fluid behavior. Because of the coupled nonlinear partial differential equations that are obtained in section 2.2, a general solution is impossible. Thus, the material in the sequel is split into consideration of three successively more complicated fluid models:

1. A constant fluid velocity, which uncouples the equations and allows an analytical solution to be obtained.
2. A laminar fluid flow, where approximate solutions are obtained by numerical integration of the differential equations.
3. A turbulent fluid flow, where solutions are obtainable only by using approximate equations.

The basic model to be analyzed is shown in Fig. 8. The average fluid flow is in the x -direction between two parallel exciting plates of infinite extent in the x - and z -directions spaced a distance $2a$ apart. The region outside the plates is filled with

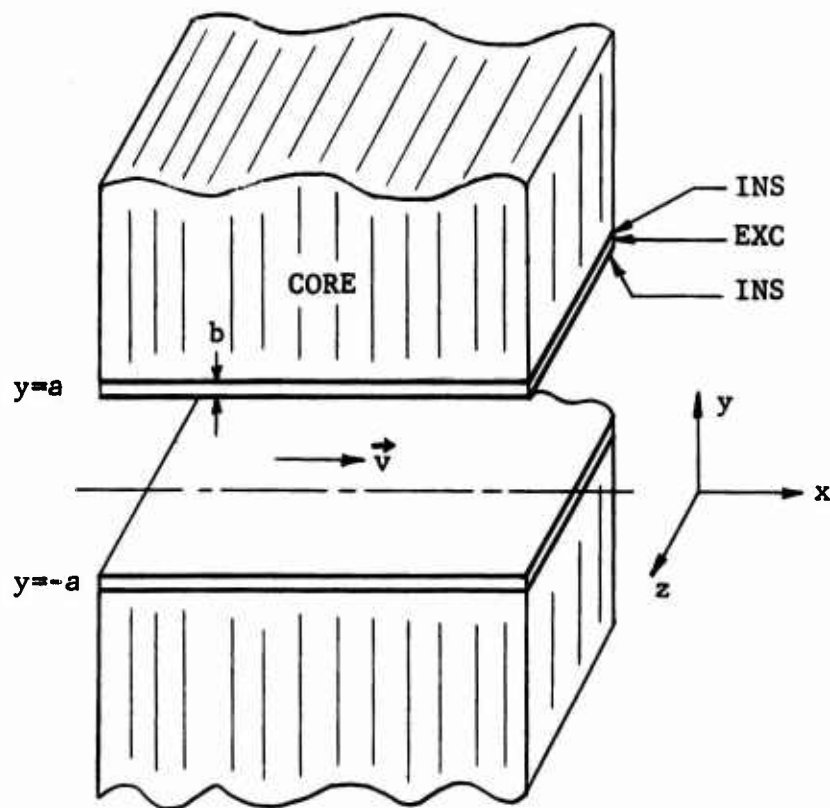


Fig. 8. The Model.

a core of arbitrary permeability μ_c and conductivity σ_c . The exciting plates, separated from the fluid and core by insulators of infinitesimal thickness to prevent current flow in the y-direction, are assumed thin so that they can be replaced by current sheets with a surface conductivity $\sigma_s = \sigma_e b$, where b is the plate thickness, and σ_e the material conductivity.* The presence of the insulators, as shown in Appendix A, allows the tangential electric field to be discontinuous across the boundary because the insulators support a dipole charge layer. The details of the excitation system are not considered.

The exciting plates are driven by a current source that gives an even or symmetric surface current density

$$\vec{K} = \vec{i}_z NI \cos(\omega t - kx). \quad (2)$$

This represents a traveling current wave of amplitude NI , frequency ω , and wavelength and velocity

$$\lambda = \frac{2\pi}{k} \quad (3)$$

and

$$v_s = \frac{\omega}{k}. \quad (4)$$

The surface current is considered to be produced by a balanced two-phase system with turns densities $N \cos kx$ and $N \sin kx$ excited by currents $I \cos \omega t$ and $I \sin \omega t$. Only two-phase excitation is considered, since, as shown by White and Woodson,³⁸ an n -phase system can be reduced to a two-phase equivalent. Excitation with odd symmetry and unbalanced excitation are treated in sections 3.5 and 3.8 as direct extensions of the symmetric, balanced case. The machine of finite length, in which the coil system has ends and the surface current may have a different x -dependence, is treated in Section VI.

2.2 EQUATIONS

The equations to be solved are Maxwell's equations for the electromagnetic field with the usual MHD approximation which neglects displacement currents, and the Navier-Stokes equation (conservation-of-momentum) for the incompressible fluid. They are

*An exciting winding of finite thickness is considered in Appendix C, and conducting channel walls and insulation in Appendix G.

$$\nabla \times \vec{B} = \mu \vec{J} \quad (5a)$$

$$\nabla \cdot \vec{B} = 0 \quad (5b)$$

$$\nabla \times \vec{E} = -\frac{\partial \vec{B}}{\partial t} \quad (5c)$$

$$\vec{J} = \sigma(\vec{E} + \vec{v} \times \vec{B}) \quad (5d)$$

$$\nabla \cdot \vec{J} = 0 \quad (5e)$$

$$\nabla \cdot \vec{E} = \frac{q}{\epsilon} \quad (5f)$$

$$\rho \left(\frac{\partial}{\partial t} + \vec{v} \cdot \nabla \right) \vec{v} = -\nabla p + \eta \nabla^2 \vec{v} + \vec{J} \times \vec{B} \quad (5g)$$

$$\nabla \cdot \vec{v} = 0 \quad (5h)$$

where

\vec{B} = magnetic flux density

μ = permeability

\vec{E} = electric field intensity

ϵ = permittivity

\vec{J} = current density

σ = electrical conductivity

\vec{v} = fluid velocity

q = electric charge density

p = pressure

η = absolute viscosity

ρ = fluid mass density

∇ = vector differential operator

Equation 5e is a consequence of neglecting displacement currents in Eq. 5a. Equation 5f serves solely to determine the required charge density, since the other equations are sufficient to determine the fields.* Equations 5d and 5h are Ohm's law and conservation of mass for the moving, incompressible fluid.

The analysis is simplified by the use of a vector potential \vec{A} defined by

$$\vec{B} = \nabla \times \vec{A} \quad (6)$$

which satisfies Eq. 5b. Equation 5c then becomes

$$\vec{E} = -\nabla \phi - \frac{\partial \vec{A}}{\partial t}, \quad (7)$$

defining the scalar potential ϕ . To complete the specification of the vector potential, its divergence is chosen to satisfy

$$\nabla \cdot \vec{A} + \mu \sigma \phi = 0, \quad (8)$$

*Equation 5f is used only in Appendix A to determine the surface charges on the fluid-insulator and excitation-insulator interfaces.

which uncouples the equations for the two potentials. Substituting Eqs. 5d, 6, and 7 in Eq. 5a and using condition (8) gives

$$\nabla^2 \vec{A} - \mu\sigma \frac{\partial \vec{A}}{\partial t} + \mu\sigma(\vec{v} \times \nabla \times \vec{A}) = 0. \quad (9)$$

Equations 8 and 9 are sufficient to determine the potentials, except in Appendices A and B, because the form chosen for \vec{A} forces ϕ to be zero.

A third equation is required in Appendices A and B. Taking the divergence of Eq. 5d and using Eq. 5e plus a vector identity gives

$$\nabla \cdot \vec{E} = \vec{v} \cdot (\nabla \times \vec{B}) - \vec{B} \cdot (\nabla \times \vec{v}). \quad (10)$$

For an infinite-width machine \vec{v} and \vec{B} are both in the xy-plane and independent of z, so that the right-hand side of the equation is zero. Using Eqs. 7 and 8 with $\nabla \cdot \vec{E} = 0$ provides the required third equation,

$$\nabla^2 \phi - \mu\sigma \frac{\partial \phi}{\partial t} = 0, \quad (11)$$

without using Eq. 5f, as a consequence of neglecting displacement currents.

The vector potential, resulting solely from currents, is also assumed to be z-directed and independent of z. Consequently,

$$\phi = 0, \quad (12)$$

from Eq. 8, for any material of nonzero conductivity. The general case of retaining all three components of the vector potential is considered in Appendix B. Obviously, the same fields must result, but the potentials are not unique,³⁹ as shown.

The two resulting coupled nonlinear vector partial differential equations are Eq. 9 and

$$\rho \left(\frac{\partial}{\partial t} + \vec{v} \cdot \nabla \right) \vec{v} = -\nabla p + \eta \nabla^2 \vec{v} - \frac{1}{\mu} (\nabla^2 \vec{A}) \times (\nabla \times \vec{A}), \quad (13)$$

obtained by writing $\vec{J} \times \vec{B}$ in terms of \vec{A} . A general solution is clearly impossible because of the nonlinear terms and two-way coupling, plus the difficulty in describing the fluid behavior. For this reason, the theory is split into consideration of the three distinct fluid models mentioned in section 2.1.

The analysis to follow will be restricted to consideration of an x-directed velocity depending on y but not time,

$$\vec{v} = \vec{i}_x v(y). \quad (14)$$

This means that the vector potential must have the same $e^{j\omega t}$ time dependence as the excitation, since the time behavior of Eq. 9 has been linearized. The electromagnetic equations are simplified by writing the vector potential in complex notation as

$$\vec{A}(x, y, t) = \text{Re} \left\{ \vec{i}_z \underline{A}(x, y) e^{j\omega t} \right\}, \quad (15)$$

in which underlining indicates complex amplitude, and \vec{A} is in the z-direction and independent of z for a machine of infinite width. In evaluating products it is necessary to take the real part before multiplying the terms together.

The equations for the complex vector potential in the fluid and core, denoted by the subscripts f and c, respectively, are

$$\nabla^2 \underline{A}_f - j R_M k^2 \underline{A}_f - \mu_f \sigma_f v \frac{\partial \underline{A}_f}{\partial x} = 0, \quad (16a)$$

and

$$\nabla^2 \underline{A}_c - j R_{Mc} k^2 \underline{A}_c = 0, \quad (16b)$$

where

$$R_M = \frac{\mu_f \sigma_f v_s}{k} \quad (17a)$$

and

$$R_{Mc} = \frac{\mu_c \sigma_c v_s}{k} \quad (17b)$$

are the fluid and core magnetic Reynolds numbers based on synchronous speed and wavelength. R_M is a partial measure of the magnitude of the field-fluid interaction; it is modified by the fluid motion. It is appropriate to use a magnetic Reynolds number for the core because it moves relative to the field with a velocity v_s . The fluid permeability μ_f must be equal to that of free space μ_0 , since there is no magnetic fluid of any importance.

Equations 16a and 16b determine the form of the solution. The constants of the solution come from the boundary conditions on the magnetic field; the electric field conditions serve solely to determine the surface charge and dipole layer densities on the insulators separating the exciting plates from the fluid and core, as shown in Appendix A. The vector potential is symmetric,

$$\underline{A}_f(x, y) = \underline{A}_f(x, -y), \quad (18)$$

from the symmetric excitation (excluding odd excitation); and the fields in the core must go to zero far from the machine,

$$\underline{A}_c(x, y) \rightarrow 0 \text{ as } y \rightarrow \infty. \quad (19)$$

At the fluid-core interface the normal magnetic field is continuous, and the discontinuity in the tangential magnetic field is proportional to the surface current. In terms of the vector potential, these are

$$\underline{A}_f = \underline{A}_c \text{ at } y = \pm a, \quad (20)$$

and

$$\frac{1}{\mu_f} \frac{\partial \underline{A}_f}{\partial y} - \frac{1}{\mu_c} \frac{\partial \underline{A}_c}{\partial y} = \pm \underline{K}(x) \text{ at } y = \pm a, \quad (21)$$

where $\underline{K}(x)$ is the complex amplitude of the exciting current.

2.3 EXCITING-COIL TERMINAL VOLTAGE

The electrical characteristics of the MHD induction machine are conveniently expressed in terms of the impedance observed at the terminals of an exciting coil. The impedance is obtained from the coil terminal voltage. Poynting's theorem can also be used,⁴⁰ but only when the machine is of infinite length and the fields have the same e^{-jkx} dependence as the exciting system.

The field equations are based on an infinite-width machine, but the voltage for a finite-width machine is desired. Care must be exercised in going from an infinite to a finite-width coil, as shown in Fig. 9, to be sure that the fields and the voltage are not changed. Initially, with no terminals, the surface current is assumed to be set up by a current source distributed in the winding. With the distributed source there is no scalar potential ϕ_e in the exciting winding, and the induced electric field is

$$\underline{E}_{ez} = -j\omega \underline{A}_f(x, y = a), \quad (22)$$

since the vector potential is continuous at $y = a$. The total electric field in the exciting winding, the sum of the induced and distributed-source electric fields, must satisfy Ohm's law. Thus, the distributed-source electric field is

$$\underline{E}_{sz} = j\omega \underline{A}_f(x, y = a) + \frac{\underline{K}}{\sigma_s}. \quad (23)$$

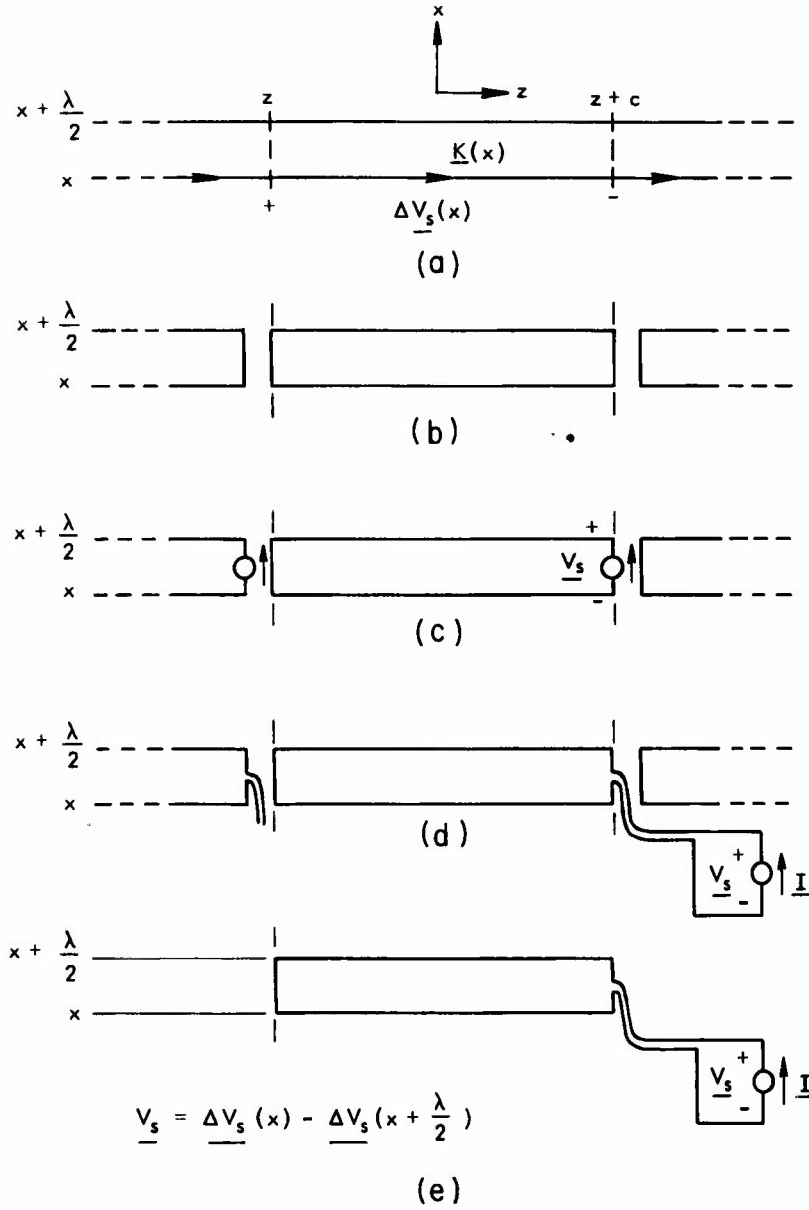


Fig. 9. Steps in calculating the coil terminal voltage.

The voltage across a length c of the distributed source,

$$\underline{\Delta V}_s(x) = \int_z^{z+c} \underline{E}_{sz} dz = j\omega c \underline{A}_f(x, y = a) + \frac{c \underline{K}(x)}{\sigma_s}, \quad (24)$$

balances the sum of the induced voltage and the resistance drop in the winding.

Since the x -component of the electric field is zero, shorting wires can be added to make a coil of width c (Fig. 9b). The oppositely directed currents in the adjacent wires cancel, so that there is no effect on the fields.

With a complete coil the distributed source can be concentrated in one of the shorting wires (Fig. 9c). The current in the exciting sheet is the same, but the electric field in the exciting sheet is changed by the addition of a scalar potential, and a dipole charge layer is required on the insulator between the fluid and the exciting sheet. There is an additional current in the fluid because of the time-variant charge on the insulator, but this is of the same order of magnitude as the displacement current and can be neglected. The total current and the magnetic field are the same. The voltage distribution around the closed coil is changed by the addition of the conservative field, but the total source voltage remains the same, balancing the induced voltage plus the resistance drop.

Removing the concentrated source from the machine by two leads brought out close together (Fig. 9d) again leaves the same net current, so that only the scalar potential is different. The final step of going from an infinite-width to a finite-width machine does change the fields and terminal voltage, because of the field distortion at the edges, but the change is small if the width is large compared with a wavelength. The effect of finite machine width is not considered.

Thus far, only one turn has been considered. The traveling field is assumed to be produced by a two-phase winding, as mentioned in section 2.1, with the individual wires connected in series to form coils. The coil terminal (source) voltage, the sum over all the wires (or integral over the turns density) of the source voltage across each wire ΔV_s , is

$$\underline{V} = 2 \int_x^{x+\lambda} [\underline{\Delta V}_s(x)] N \begin{Bmatrix} \cos kx \\ \sin kz \end{Bmatrix} dx \quad (25)$$

for a coil one wavelength long; where $\cos kx$ and $\sin kx$ are for the two phases, and \underline{V} is twice the integral because there are identical coils above and below the channel. The same result is obtained for either phase, except for a 90° phase difference, only when the fields have a simple e^{-jkx} dependence.

2.4 POWERS

Consideration is restricted to the time-average powers because of the field products involved. The time-average real power supplied to the fluid by the exciting system is

$$P_s = \text{Re} \left\{ - \oint_{\text{surf}} (\underline{\vec{S}}_f \cdot \underline{\vec{i}}_n) da \right\} , \quad (26)$$

where

$$\underline{\vec{S}}_f = \frac{1}{2\mu_f} (\underline{\vec{E}}_f \times \underline{\vec{B}}_f^*) \quad (27)$$

is the time-average complex Poynting's vector, the * denotes the complex conjugate, \vec{i}_n is a unit vector normal to the surface and outwardly directed, and the surface, located at $y = \pm a$, encloses the fluid.

The mechanical power output, the power supplied to the external fluid system by the machine, is the product of the time-average electromagnetic pressure gradient and the velocity integrated over the fluid volume,

$$P_m = \int_{vol} \langle \nabla p_{em} \rangle \cdot \vec{v} \, dx dy dz, \quad (28)$$

where

$$\langle \nabla p_{em} \rangle = \text{Re} \left\{ \frac{\vec{J}_f \times \vec{B}_f^*}{2} \right\}. \quad (29)$$

The power dissipated in the fluid, because of its finite conductivity, which is always positive, is

$$P_r = \int_{vol} \frac{\vec{J}_f \cdot \vec{J}_f^*}{2\sigma_f} \, dx dy dz. \quad (30)$$

It is the integral of $(\vec{J} \cdot \vec{J}^*)/2\sigma$, not $\text{Re} \left\{ \vec{E} \cdot \vec{J}^* / 2 \right\}$, as the latter formula would result in

$$\begin{aligned} \text{Re} \left\{ \frac{\vec{E} \cdot \vec{J}^*}{2} \right\} &= \frac{\vec{J} \cdot \vec{J}^*}{2\sigma} - \text{Re} \left\{ \frac{(\vec{v} \times \vec{B}) \cdot \vec{J}^*}{2} \right\} = \frac{\vec{J} \cdot \vec{J}^*}{2\sigma} \\ &\quad + \vec{v} \cdot \langle \nabla p_{em} \rangle. \end{aligned} \quad (31)$$

This includes both the power dissipated in the fluid and the power converted from electrical to mechanical form, and its integral gives P_s .

The efficiency including only the I^2R loss in the fluid is

$$e_g = \frac{P_s}{P_m} \quad (32g)$$

or

$$e_p = \frac{P_m}{P_s}, \quad (32p)$$

where g and p stand for generator and pump operation, and P_s and P_m are both negative for generator operation. This sets an upper limit on the obtainable machine efficiency.

The remaining powers are the losses in the core, exciting coils, and fluid viscosity. The core loss P_c is found in the same manner as P_s , except that Poynting's vector in the core is used and the surface now surrounds the core. Alternatively, it could be obtained by integrating $(\underline{J}_c \cdot \underline{J}_c^*)/2\sigma_c$ over the core volume. The coil loss is

$$P_e = 2 \int_z^{z+c} \int_x^{x+n\lambda} \frac{\underline{K}(x) \cdot \underline{K}^*(x)}{2\sigma_s} dx dz = \frac{N^2 I^2 c n \lambda}{\sigma_s} \quad (33)$$

Here, the last expression in (33) is obtained for the exciting current of Eq. 2 for a machine of length n wavelengths and width c. The fluid viscous loss P_v is considered in Appendix D.

III. CONSTANT FLUID VELOCITY

The fluid flow will in general be turbulent, so that details of the flow are of limited value. The fluid velocity is assumed to be constant, which uncouples the electromagnetic and fluid equations and allows an analytical solution to be obtained. This emphasizes the important features without obscuring them in the mathematical detail which occurs later.

3.1 ELECTROMAGNETIC FIELDS

The constant fluid velocity eliminates the need for the fluid equations and simultaneously linearizes the electromagnetic equations. The excitation, the uniform surface current of Eq. 2, can be written in complex notation as

$$\vec{K} = \vec{i}_z \operatorname{Re} \left\{ NI e^{j(\omega t - kx)} \right\} . \quad (34)$$

Since the system is linear, the vector potential must possess this same exponential dependence. Redefining the complex amplitude of Eq. 15 for this case as

$$\vec{A}(x,y,t) = \operatorname{Re} \left\{ \vec{i}_z \underline{A}(y) e^{j(\omega t - kx)} \right\} , \quad (35)$$

and substituting this in Eqs. 16 and 17, gives

$$\frac{d^2 \underline{A}_f}{dy^2} - \gamma^2 k^2 \underline{A}_f = 0 \quad (36)$$

and

$$\frac{d^2 \underline{A}_c}{dy^2} - \delta^2 k^2 \underline{A}_c = 0 , \quad (37)$$

where

$$\gamma^2 = 1 + jsR_M \quad (38a)$$

$$\delta^2 = 1 + jR_{Mc} \quad (38b)$$

$$s = \frac{(v_s - v)}{v_s} , \quad (38c)$$

and R_M and R_{Mc} are defined in Eqs. 17. The slip based on synchronous (field) speed s represents the motion of the field relative to the fluid. The magnitude of the field-fluid interaction is indicated by sR_M , which is based on the velocity difference $v_s - v$, rather than by R_M alone.

The form of the potentials, from Eqs. 37 and 38, is

$$\underline{A}_f = \underline{A}_{f1} \cosh \gamma ky + \underline{A}_{f2} \sinh \gamma ky \quad (39)$$

and

$$\underline{A}_c = \underline{A}_{c1} e^{-\delta k |y|}, \quad (40)$$

since \underline{A}_c must approach zero far from the core. The vector potential is symmetric, from the symmetric excitation, so that $\underline{A}_{f2} = 0$. By applying the boundary conditions at the fluid-core interface, Eqs. 20 and 21, the solution is

$$\underline{A}_f = \frac{\mu_f NI \cosh \gamma ky}{k(\gamma \sinh \gamma a + \kappa \delta \cosh \gamma a)} \quad \text{for } |y| \leq a \quad (41)$$

and

$$\underline{A}_c = \frac{\mu_f NI e^{-\delta k(|y| - a)}}{k(\gamma \tanh \gamma a + \kappa \delta)} \quad \text{for } |y| \geq a, \quad (42)$$

in which

$$a = ak \quad (43a)$$

and

$$\kappa = \frac{\mu_f}{\mu_c} \quad (43b)$$

are the ratios, respectively, of the channel width to the excitation wavelength and the fluid to core permeability. The electromagnetic fields, determined from the potentials through Eqs. 6 and 7, are listed in Table 1.

Table 1. Electromagnetic fields for a constant fluid velocity.

$$\underline{\vec{B}}_f = \frac{\mu_f NI (\vec{i}_x \gamma \sinh \gamma ky + \vec{i}_y j \cosh \gamma ky)}{\gamma \sinh \gamma a + \kappa \delta \cosh \gamma a} \quad (44a)$$

$$\underline{\vec{E}}_f = - \frac{\vec{i}_z j v_s \mu_f NI \cosh \gamma ky}{\gamma \sinh \gamma a + \kappa \delta \cosh \gamma a} \quad (44b)$$

Table 1. Electromagnetic fields for a constant fluid velocity (Cont.).

$$\underline{\vec{J}}_f = - \frac{\vec{i}_z j k s R_M NI \cosh \gamma ky}{\gamma \sinh \gamma a + \kappa \delta \cosh \gamma a} \quad (44c)$$

$$\underline{\vec{B}}_c = \frac{\mu_f NI (-\vec{i}_x \delta + \vec{i}_y j) e^{-\delta k(|y| - a)}}{\gamma \tanh \gamma a + \kappa \delta} \quad (44d)$$

$$\underline{\vec{E}}_c = - \frac{\vec{i}_z j v_s \mu_f NI e^{-\delta k(|y| - a)}}{\gamma \tanh \gamma a + \kappa \delta} \quad (44e)$$

$$\underline{\vec{J}}_c = - \frac{\vec{i}_z j k \kappa R_{Mc} NI e^{-\delta k(|y| - a)}}{\gamma \tanh \gamma a + \kappa \delta} \quad (44f)$$

3.2 ELECTRICAL IMPEDANCE

The impedance observed at the terminals of an exciting coil one wavelength long, obtained from the terminal voltage of section 2.3, is broken up into series and parallel equivalent circuits for the machine. The formulas are then discussed and simplified for a narrow-channel machine.

The terminal voltage for a constant fluid velocity is determined from Eq. 25 to be

$$\underline{V} = \frac{2\pi N^2 c}{k} \left(\frac{1}{\sigma_s} + \frac{j v_s \mu_f}{\gamma \tanh \gamma a + \kappa \delta} \right) \underline{I} . \quad (45)$$

The same result is obtained for either phase, except for a 90° phase shift which has no effect on the impedance. The series-equivalent-circuit resistance and inductance per coil, from

$$\underline{V} = (R_s + j \omega L_s) \underline{I} , \quad (46)$$

are

$$R_s = R_e - R_o I_m \left\{ \frac{1}{\gamma \tanh \gamma a + \kappa \delta} \right\} \quad (47)$$

and

$$L_s = L_o \operatorname{Re} \left\{ \frac{1}{\gamma \tanh \gamma a + \kappa \delta} \right\} , \quad (48)$$

where

$$R_o = \omega L_o = \frac{2\pi \mu_f v_s N_c^2}{k}, \quad (49)$$

and

$$R_e = \frac{2\pi N_c^2}{k \sigma_s} \quad (50)$$

is the internal resistance of the coil, because of its finite conductivity. Excluding R_e , the normalized ratios R_s/R_o and L_s/L_o depend only on the dimensionless parameters s , R_M , R_{Ma} , α , and κ .

The formulas above can be simplified for the case of a narrow or slit channel, $\gamma\alpha \ll 1$, with a lossless core and exciting coils ($R_{Mc} = 0$, $R_e = 0$), to

$$\frac{R_s}{R_o} = \left(\frac{1}{\kappa + \alpha} \right) \frac{s R_{Ma}}{1 + s^2 R_{Ma}^2}, \quad (51)$$

and

$$\frac{L_s}{L_o} = \left(\frac{1}{\kappa + \alpha} \right) \frac{1}{1 + s^2 R_{Ma}^2}. \quad (52)$$

Here,

$$R_{Ma} = \left(\frac{1}{1 + \frac{\kappa}{\alpha}} \right) R_M \quad (53)$$

is the pertinent magnetic Reynolds number. These equations clearly show the dependence of the circuit elements on machine parameters without the interference of complicated equations and secondary losses. The appropriate magnetic Reynolds number R_{Ma} is based on the exciting wavelength and fluid permeability for a good core, $\kappa < \alpha$, and on the channel width and core permeability for a poor core, $\kappa > \alpha$.

The slit-channel resistance and inductance are plotted in Figs. 10 and 11 versus s (or v) with R_{Ma} as a parameter. The extremes of $(\kappa + \alpha) R_s/R_o$ are $\pm 1/2$ and occur at the values $s R_{Ma} = \pm 1$. Any R_{Ma} can be compensated for by varying s to hold the resistance or power level constant, but increasing the magnitude of s lowers the efficiency, as shown in section 3.3, so that R_{Ma} should be as large as possible. Since $R_{Ma} \leq R_M$, machine operation is always best with an ideal iron core because the smaller reluctance of the magnetic circuit results in larger applied and reaction fields. Note that maximum resistance corresponds to maximum power only for constant-current excitation.

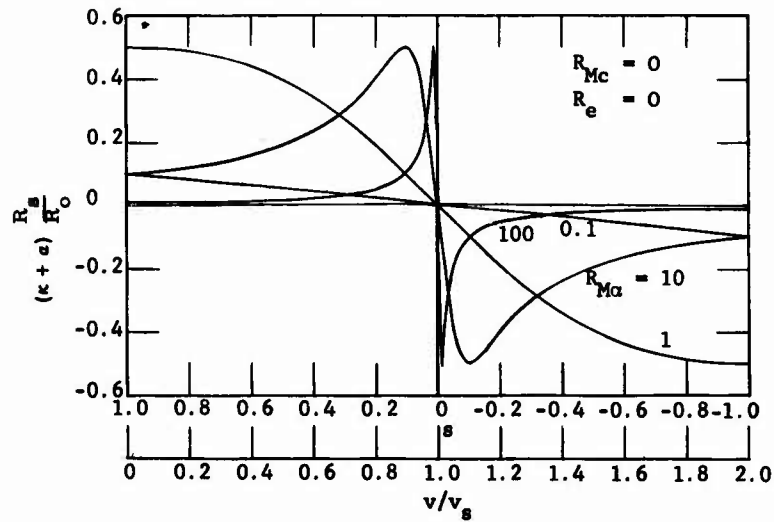


Fig. 10. Series resistance of the slit-channel machine as a function of s and R_{Ma} .

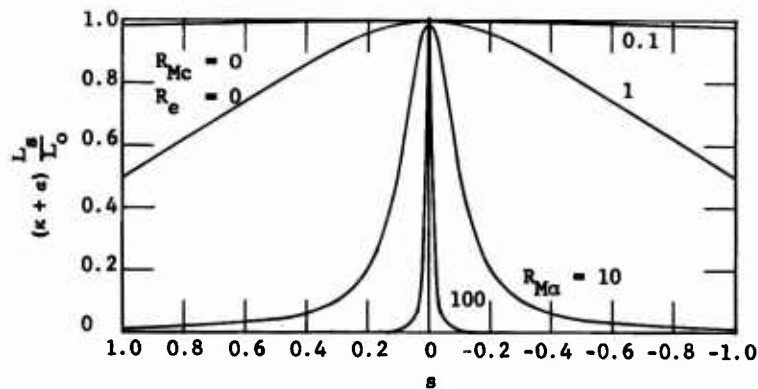


Fig. 11. Series inductance of the slit-channel machine as a function of s and R_{Ma} .

The slit-channel equations show that increasing the channel height a (or α) results in less interaction. For an ideal core, $\kappa = 0$, the magnetic field varies as $1/a$; and the power density, which is proportional to the magnetic field squared, goes as $1/a^2$. Since the volume is proportional to a , the total power varies as $1/a$. The variation is decreased for $\kappa \neq 0$, but it is still true that a (or α) should be as small as possible, and that κ should also be as small as possible.

Approximate expressions can also be found for large γa , $\text{Re} \{ \gamma a \} \geq 3$, so that $\tanh \gamma a \approx 1$. Then, for a lossless exciting coil,

$$\frac{R_s}{R_o} = -\operatorname{Im} \left\{ \frac{1}{\gamma + \kappa \delta} \right\} = \pm \frac{1}{\sqrt{2 |s R_M|}} \text{ for } s \begin{matrix} > \\ < \end{matrix} 0, \quad (54)$$

and

$$\frac{L_s}{L_o} = \operatorname{Re} \left\{ \frac{1}{\gamma + \kappa \delta} \right\} = \frac{1}{\sqrt{2 |s R_M|}}. \quad (55)$$

The second expressions, valid for $|s R_M| \gg 1$ and a lossless core, show that this case is not good for constant-current excitation because the resistance and power are small.

The general formulas, containing additional variables, are harder to visualize. Increasing either κ or α will still decrease the interaction. The location of the maxima of R_s/R_o will move, but the general shape of the curves remains the same. The addition of core loss will shift the point where $R_s = 0$ away from $s = 0$, since the fluid must supply the core loss before any net power output is obtained. The ratios R_s/R_o and L_s/L_o are plotted in Figs. 12 and 13 versus s with R_{Mc} as a parameter to show this. They are an extreme case for demonstration purposes, with both κ and R_{Mc} large. If the core loss δ is appreciable, κ will be much less than one for any reasonable core. The shape of the curves is determined by R_{Ma} , not R_M , because $\kappa > \alpha$.

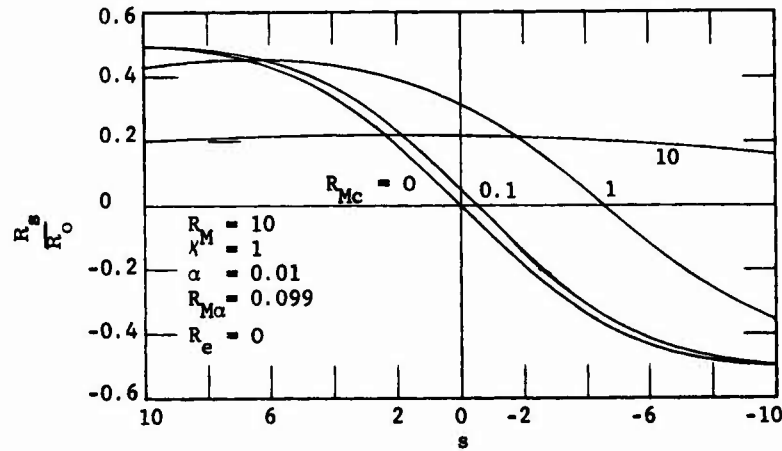


Fig. 12. Series resistance as a function of s and R_{Mc} .

A series-equivalent circuit is derived as a natural consequence of the inductive system, but a parallel version may be more useful in studying the practical aspects of the MHD induction machine. In terms of the series elements, the parallel values are

$$R_p = \frac{R_s^2 + \omega^2 L_s^2}{R_s}, \quad (56)$$

and

$$L_p = \frac{R_s^2 + \omega^2 L_s^2}{\omega^2 L_s} . \quad (57)$$

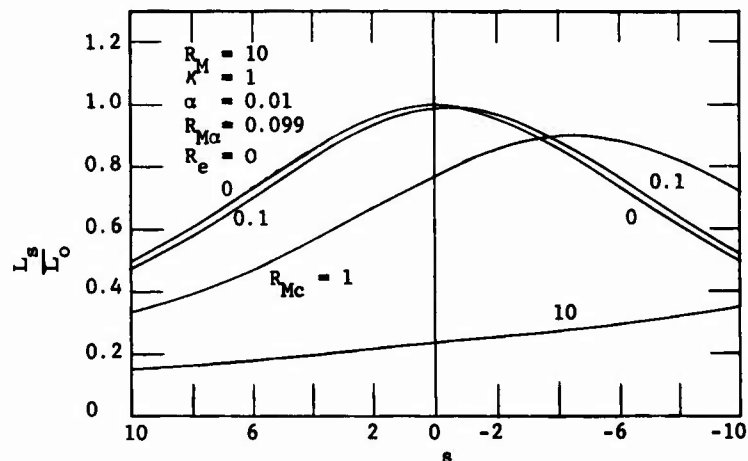


Fig. 13. Series inductance as a function of s and R_{Mc} .

First, considering the coil resistance R_e separately, the equivalent circuit of Fig. 14b is obtained, where

$$\frac{R_p}{R_o} = \frac{1}{\text{Im} \{ \gamma \tanh \gamma a + \kappa \delta \} } , \quad (58)$$

and

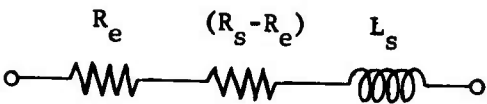
$$\frac{L_p}{L_o} = \frac{1}{\text{Re} \{ \gamma \tanh \gamma a + \kappa \delta \} } . \quad (59)$$

These equations differ from the series results in that the real and imaginary parts are in the denominator. This makes a significant difference in the circuit values, as is shown by the slit-channel equations for a lossless core,

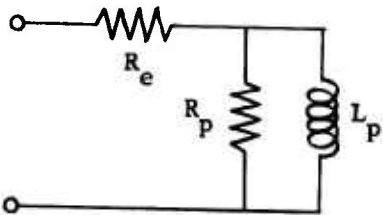
$$\frac{R_p}{R_o} = \left(\frac{1}{\kappa + \alpha} \right) \frac{1}{s R_{Ma}} , \quad (60)$$

and

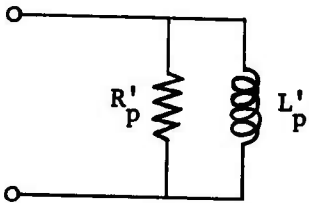
$$\frac{L_p}{L_o} = \frac{1}{\kappa + \alpha} \tag{61}$$



(a) Series Equivalent With R_e Separated



(b) Parallel Equivalent With R_e Separated



(c) Total Parallel Equivalent

Fig. 14. Equivalent circuits.

For large $\gamma \alpha$, $\text{Re} \left\{ \gamma \alpha \right\} \geq 3$, the approximate equations are

$$\frac{R_p}{R_o} = \frac{1}{\text{Im} \left\{ \gamma + \kappa \delta \right\}} = \pm \sqrt{\frac{2}{|sR_M|}} \text{ for } s > 0 \tag{62}$$

and

$$\frac{L_p}{L_o} = \frac{1}{\text{Re} \{ \gamma + \kappa \delta \}} = \sqrt{\frac{2}{|sR_M|}}, \quad (63)$$

where the second expressions are for $|sR_M| \gg 1$ and a lossless core.

From the parallel equivalent circuit, it is seen that the field-fluid interaction increases without limit with increasing $|sR_{Ma}|$ if the voltage is held constant, as opposed to constant-current excitation where there is a peak. For constant-current excitation the reaction current of the fluid reduces the net current and thus the field for large $|sR_{Ma}|$, so that less interaction occurs. For constant-voltage excitation the flux linkage or magnetic field is held constant, so that the current increases with $|sR_{Ma}|$ and no peak occurs. The same results are obtained for either equivalent circuit, but the series one naturally corresponds to constant current, the parallel one to constant voltage. Constant-voltage excitation is closer to actual operating conditions.

Including the coil resistance R_e greatly increases the complexity because it is not related to the other terms and the equations do not simplify. It can be left in series with the parallel combination of R_p and L_p (Fig. 14b) or a new total parallel equivalent (Fig. 14c) can be found.

Adding R_e plus the leakage reactance^{*} X_e to the discussion changes the conclusions. The voltage that was previously held constant was the internal induced voltage, corresponding to operation at magnetic saturation. For a generator, as the current increases with $|sR_{Ma}|$ the total generated power increases, but the power output eventually decreases as the external load becomes small compared with the internal impedance of the winding, R_e and X_e . If the terminal voltage is held constant as in a large power system, the internal voltage and interaction decrease with increasing current, because of the voltage drop across R_e and X_e . In either case a peak in the output power occurs, and that peak is controlled by R_e and X_e .

The Q of the induction machine, the amount of reactive power required to obtain a specified real power, is

$$Q = \frac{\omega L_s}{R_s} = \frac{1}{sR_{Ma}}, \quad (64)$$

where the second form is valid only for a slit channel and a lossless core. To make the reactive power small compared with the real power, $|sR_{Ma}|$ should be large, but this in turn may result in less energy transfer, the result depending on the exciting conditions. The power factor is

^{*}Leakage reactance, caused by flux set up by the exciting current that does not link the fluid, has been neglected in the idealized model.⁴¹

$$\cos \theta = \frac{R}{\sqrt{ZZ^*}} = \frac{sR_{Ma}}{\sqrt{1 + s^2 R_{Ma}^2}}, \quad (65)$$

where the second expression is again for a slit channel and a lossless core. These results are used in Section VII to discuss practical aspects of the induction machine.

3.3 POWERS

The time-average powers are calculated from the equations of section 2.4. Poynting's vector in the fluid is

$$\vec{S}_f = \frac{\mu_f v_s N^2 I^2}{2(\gamma \sinh \gamma a + \kappa \delta \cosh \gamma a)} \frac{(\vec{i}_x \cosh \gamma ky \cosh \gamma^* ky - \vec{i}_y \gamma^* \cosh \gamma ky \sinh \gamma^* ky)}{(\gamma^* \sinh \gamma^* a + \kappa \delta^* \cosh \gamma^* a)}, \quad (66)$$

The x component represents a constant power flow; it makes no contribution to the power supplied to the fluid. The powers for a machine n wavelengths long in the x-direction and of depth c in the z-direction are

$$P_s = \frac{P_o I_m}{(\gamma \tanh \gamma a + \kappa \delta) (\gamma^* \tanh \gamma^* a + \kappa \delta^*)} \quad (67)$$

$$P_m = (1 - s) P_s \quad (68)$$

$$P_r = s P_s, \quad (69)$$

where

$$P_o = \mu_f v_s N^2 I^2 c n \lambda = I^2 R_o (n). \quad (70)$$

The second form of P_o points out the relation between the powers and the impedance. For a slit channel and lossless core, P_s becomes

$$\frac{P_s}{P_o} = \left(\frac{1}{\kappa + a} \right) \frac{s R_{Ma}}{1 + s^2 R_{Ma}^2}. \quad (71)$$

Note that P_s differs from the electrical power input to the machine by the power loss in the coils and core. These results for P_s , P_m , and P_r are identical to the power-flow relations for a rotating induction machine.^{1,2}

One set of power curves is plotted in Fig. 15 for a slit-channel, lossless-core machine with constant-current excitation. The three regions of operation are shown: pump, generator, and damper.

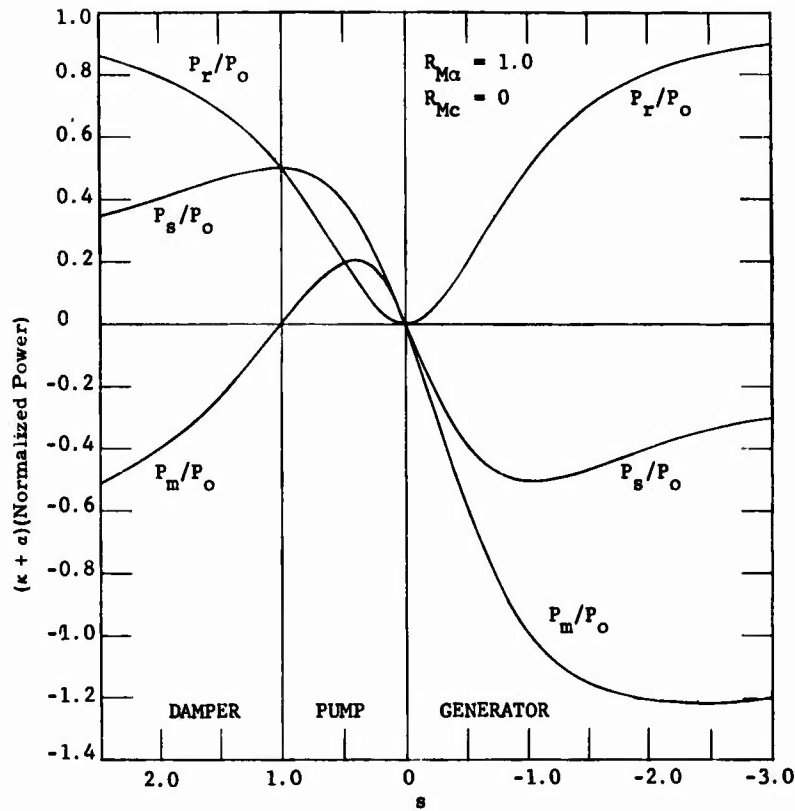


Fig. 15. Normalized powers for a slit-channel machine with constant-current excitation as a function of s .

The induction machine requires power loss in the fluid for its operation. Equation 69 shows that if P_r is zero, P_s must be zero. This is also seen from the field picture described in section 1.2. If the fluid resistance is zero, the fluid current lags the induced voltage by 90° , because of the inductance, and the reaction field lags the applied field by 180° . Thus, referring to Fig. 3, the equivalent fluid magnetic poles lie midway between two pairs of exciting poles, and the net electromagnetic force is zero.

For operation at constant induced voltage, corresponding to saturation of the iron core, P_s for a slit-channel machine can be rewritten in terms of the constant transverse magnetic field,

$$\underline{B}_{fy} = \frac{j\mu_f NI}{(1 + jsR_M) \alpha + \kappa \delta}, \quad (72)$$

as

$$P_s = \frac{\alpha v_s \cosh \lambda}{\mu_f} \underline{B_{fy}} \underline{B_{fy}^*} s R_M. \quad (73)$$

This expression, valid for any core, again shows the steady rise in power transferred to (or from) the fluid at constant induced voltage.

The electrical efficiency, including only the power loss in the fluid conductivity, is

$$e_g = \frac{1}{1-s} \text{ for } s < 0 \quad (74g)$$

or

$$e_p = 1 - s \text{ for } s > 0. \quad (74p)$$

This represents the upper limit to the attainable efficiency inherent in the induction machine.

The power loss in the core is

$$P_c = \frac{P_o \kappa \operatorname{Im} \{ \delta \}}{(\gamma \tanh \gamma \alpha + \kappa \delta) (\gamma^* \tanh \gamma^* \alpha + \kappa \delta^*)}. \quad (75)$$

If the exciting coil and fluid viscous losses are negligible, the generator and pump efficiencies are

$$e'_g = \frac{1}{1-s} \left\{ 1 + \frac{\operatorname{Im} (\kappa \delta)}{\operatorname{Im} (\gamma \tanh \gamma \alpha)} \right\} \text{ for } s < 0 \quad (76g)$$

and

$$e'_p = (1-s) \left\{ \frac{1}{1 + \frac{\operatorname{Im} (\kappa \delta)}{\operatorname{Im} (\gamma \tanh \gamma \alpha)}} \right\} \text{ for } s > 0. \quad (76p)$$

The terms in brackets, always less than or equal to one, represent the decrease in efficiency, because of core loss.

3.4 SKIN EFFECT

The vector potential for a constant fluid velocity, Eq. 39, can also be written in the form

$$e^{\pm \frac{y}{\delta}} s [\cos \epsilon_s y + j \sin \epsilon_s y], \quad (77)$$

where

$$\delta_s = \frac{1}{\text{Re } \{\gamma k\}} \quad (78)$$

and

$$\epsilon_s = \text{Im } \{\gamma k\} . \quad (79)$$

The electromagnetic field decays exponentially from the surface with the space constant δ_s , which is called the skin or penetration depth. The exponential spatial dependence resulting from finite electrical conductivity, represented by the time derivative in Eq. 9, is a familiar trademark of skin effect. In this case there is an exponential dependence even if no conducting material is present, $\sigma_f = 0$. This is a property of the two-dimensional solution of Laplace's equation,⁴² and is referred to here as the geometrical skin effect. The remaining term of Eq. 9, involving the fluid velocity, represents the effect of motion on the field. It modifies the skin depth caused by the conductivity, as seen in Eq. 81, but differs from the conventional electrical skin effect in changing the phase angle, as discussed in section 1.2.

The two sources of the exponential dependence cannot be treated independently, since they interact. The space constant for the geometrical skin effect, with $\sigma_f = 0$, is

$$\delta_g = \frac{1}{k} , \quad (80)$$

while the purely electrical skin depth is^{*}

$$\delta_e = \sqrt{\frac{2}{\omega \mu \sigma}} = \frac{1}{k} \sqrt{\frac{2}{|s R_M|}} . \quad (81)$$

In the second form, written for the fluid, the slip s appears because the frequency seen by the fluid is not the exciting frequency ω , but the reduced frequency $s \omega$, because of the relative motion between the fluid and the traveling field. The skin depth δ_s simplifies to δ_g for $|s R_M| \ll 1$, and δ_e for $|s R_M| \gg 1$. For the intermediate region Eq. 78 can be rewritten as

$$\frac{1}{\delta_s} = \text{Re} \left\{ \sqrt{\frac{1}{\delta_g^2} + \frac{2j}{\delta_e^2}} \right\} . \quad (82)$$

The ratio δ_g/a determines the importance of the skin effect. If the ratio is of the order of or less than one, only the fluid adjacent to the excitation takes part in the

*As an indication of the numbers involved, δ_e is 0.85 cm for copper, and 2 cm for liquid sodium at 60 cps.

interaction. Otherwise, the field penetrates the full channel width, and the power density is almost constant across the channel. As an example, for $\alpha = 0.1$, $(\delta_s/a) = 1$ when $|sR_M| = 200$, and the field and power density at the center of the channel are 77% and 59%, respectively, of their values at the edge. These are increased to 92% and 85% for $|sR_M| = 100$, and to 99.4% and 98.8% for $|sR_M| = 10$. For the values of $|sR_M|$ expected in a practical machine, skin effect is important only for $\alpha > 0.1$, a relatively wide channel.

The series resistance R_s and the constant-current power P_s (Figs. 10 and 15) have maximum values at or near $|sR_{Ma}| = 1$, and decrease for larger $|sR_{Ma}|$. This drop in power level, as explained in section 3.2, occurs when the reaction current in the fluid becomes comparable in magnitude to the exciting current, decreasing the net current and magnetic field. It does not occur at all for constant-voltage excitation. This is not caused by skin effect, although the two are related because both indicate appreciable reaction fields, as is shown by a slit-channel machine in which the decrease occurs even though there is no variation in the fields across the channel.

The separate consideration of skin effect complements the material of sections 3.1 through 3.3 and leads to a better understanding of the machine. It is included in the previous theory but not explicitly considered. Its effect is small, provided α is small, because of practical limitations on $|sR_M|$. Skin effect is used in comparing even and odd excitation in section 3.6, and is seen in section 3.7 in which field profiles are plotted and discussed. The shape of the curves can be roughly predicted by Eq. 78.

3.5 ODD EXCITATION

With odd or antisymmetric excitation the currents in the two exciting sheets are in opposite directions,

$$\vec{K} = \pm \vec{i}_z NI \cos(\omega t - kx) \text{ at } y = \pm a \quad (83)$$

This corresponds to wrapping the exciting winding around the machine as in a traveling-wave tube. The conventional rotating machine, with the coils imbedded in the face of the magnetic structure, is an example of even excitation. Qualitatively, the magnetic field produced by even excitation is primarily perpendicular to the flow for a narrow channel, while for odd excitation it is primarily parallel to the flow. Since only the perpendicular component interacts with the fluid, even excitation is to be preferred for energy conversion. A machine with odd excitation may be considerably easier to build, particularly for a round channel.

The model and equations for odd excitation differ only in that the exciting current of Eq. 83 is used. Consequently, the symmetry conditions on the field components are reversed. The form of the vector potential in the fluid is the same as for even excitation, Eq. 39, but now only the $\sinh \gamma ky$ term is retained, because of the odd symmetry.

The only change from the even-excitation solution is the interchange of sinh and cosh in all the equations. For example, the series-equivalent resistance and inductance are

$$R_{so} = R_e - R_o \operatorname{Im} \left\{ \frac{1}{\gamma \coth \gamma a + \kappa \delta} \right\}, \quad (84)$$

and

$$L_{so} = L_o \operatorname{Re} \left\{ \frac{1}{\gamma \coth \gamma a + \kappa \delta} \right\}, \quad (85)$$

where R_e , R_o , and L_o are defined in Eqs. 49 and 50, and an o subscript is added to distinguish between the two excitations.

3.6 COMPARISON OF EVEN AND ODD EXCITATIONS

Comparison of even and odd excitations is difficult because it is hard to visualize how tanh and coth of complex arguments vary. Roughly, the difference should be large for a narrow channel, $\gamma a \ll 1$, and small when skin effect becomes appreciable, $\gamma a \gg 1$. The comparison is split into three regions, for γa smaller than, larger than, and of the order of one. Only impedances are compared. It is not necessary to do the powers separately, since they are included in the resistance. Field and force profiles for both excitations are plotted and discussed in section 3.7.

For $\gamma a \ll 1$ the slit-channel approximation can be used for odd excitation. Then, for a lossless core and exciting coils, Eqs. 84 and 85 become

$$\frac{R_{so}}{R_o} = 0, \quad (86)$$

and

$$\frac{L_{so}}{L_o} = \frac{a}{1 + \kappa a}, \quad (87)$$

to first-order in γa . There is no interaction between the fluid and the electromagnetic field, and no energy conversion. To be consistent with this there must be no electromagnetic pressure gradient in the fluid. The magnetic field for odd excitation is

$$\vec{B}_{fo} = \frac{\mu_f NI (\vec{i}_x \gamma \cosh \gamma ky + \vec{i}_y \sinh \gamma ky)}{(\gamma \cosh \gamma a + \kappa \delta \sinh \gamma a)} \quad (88)$$

The pressure gradient, depending on the transverse magnetic field squared, is proportional to $(\gamma a)^2$ and y^2 for a slit channel, as compared with that for even excitation which is proportional to $1/(\gamma a)^2$ and independent of y . The pressure gradient is zero to first-order in γa , which agrees with the resistance.

The energy density and power output with odd excitation are smallest for small γa , while for even excitation they are largest. The best operating condition is even excitation for small γa , which is clearly superior to odd excitation by many orders of magnitude. Only for γa of the order of or greater than one, when skin effect becomes appreciable, are the two excitations comparable.

For large γa ,

$$\operatorname{Re} \{ \gamma a \} \geq 3, \quad (89)$$

approximate expressions can be used because $\tanh \gamma a$ and $\coth \gamma a$ are both equal to one with an error of less than $\pm 1/2 \%$ for each, and a difference of less than 1% in their real parts or magnitudes. Then,

$$R_{so} = R_e - R_o \operatorname{Im} \left\{ \frac{1}{\gamma + \kappa \delta} \right\}, \quad (90)$$

and

$$L_{so} = L_o \operatorname{Re} \left\{ \frac{1}{\gamma + \kappa \delta} \right\}, \quad (91)$$

which are identical with Eqs. 54 and 55 for even excitation. The circuit elements for both excitations are the same, and are independent of a . Comparison with Eq. 78 shows that

$$\frac{\delta_s}{a} \leq \frac{1}{3}, \quad (92)$$

or that skin effect is pronounced. The fields do not penetrate into the fluid, so that the interaction is confined to thin strips adjacent to the walls. Thus the electromagnetic fields and powers do not depend on the type of excitation or the channel width (a), and neither do the circuit elements. This case is poor for energy conversion, because of the low power density.

For the intermediate region, γa of the order of one, there are no approximate expressions. Curves of the series resistance for both excitations are plotted against sR_M with a and κ as parameters in Figs. 16 and 17. Only one quadrant is shown because of symmetry. When the curves for $a = 0.1$ or less are not shown, it is because those for even excitation are too large for the graph, while those for odd excitation amount to only a few per cent of full scale. It is evident that for small a , as mentioned previously, even excitation is preferable to odd excitation or to either case for larger a . For $a \geq 3$, Eq. 89 is satisfied for any value of sR_M and the curves are independent of a or the type of excitation. They still exhibit the familiar shape with a peak in the resistance curve due to the dependence of γ on sR_M .

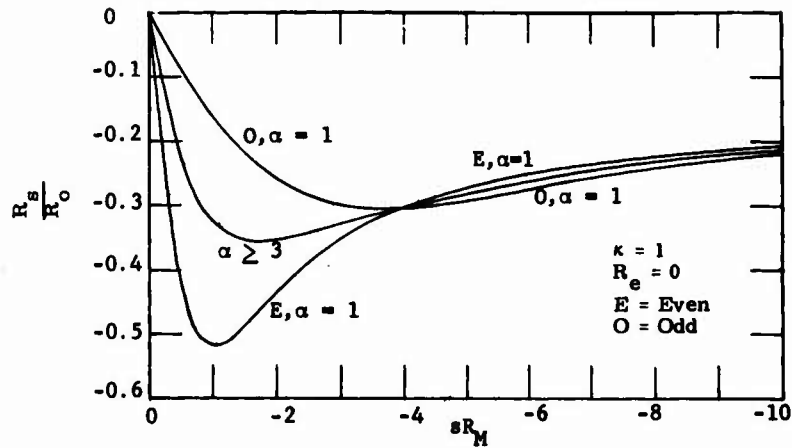


Fig. 16. Series resistance for even and odd excitation with $\kappa = 0$ as a function of sR_M and α .

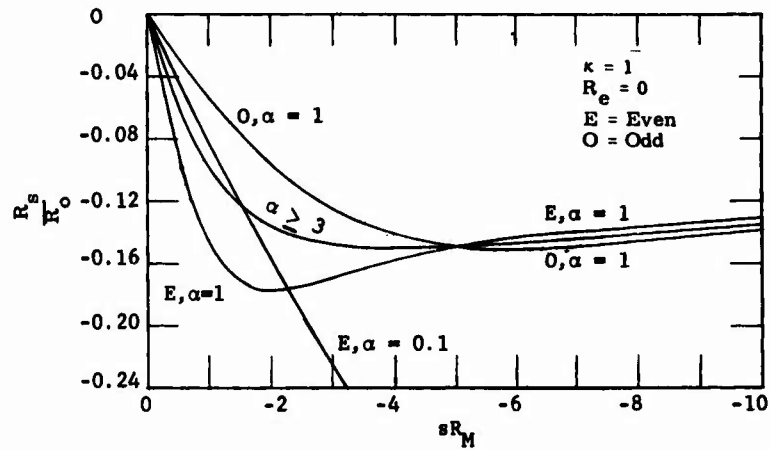


Fig. 17. Series resistance for even and odd excitation with $\kappa = 1$ as a function of sR_M and α .

For α around one, so that skin effect is large but not dominant, the difference between the two excitations is small. For $\alpha = 1$ and $\kappa = 0$ (Fig. 16), the even peak power is approximately twice the odd peak power, but there is a range past the peaks where odd excitation is approximately 10% better. For $\alpha = 1$ and $\kappa = 1$, (Fig. 17) the general behavior is the same except that both differences are less because the κ term in the denominator partially obscures the excitation effects. For large $|sR_M|$ the curves merge, with Eq. 89 satisfied at $|sR_M| = 17$.

The crossover of the even and odd excitation curves cannot be easily predicted from examination of the equations. In that region both $\tanh \gamma a$ and $\coth \gamma a$ differ from one

by less than $\pm 7\%$, so that the shape of the curves is controlled mainly by γ , as shown by the nearness to the $\alpha \geq 3$ curve. It is only the small differences that are important, with the result independent of whether $\tanh \gamma \alpha$ is greater or less than one. The field profiles for $\alpha = 1$ and $sR_M = -10$, if plotted, would show that the odd field is larger to account for the higher energy density. This region is not good for energy conversion, because of the low energy density, which can be improved for either case by decreasing $|sR_M|$.

Curves of inductance and Q , plotted in Figs. 18 – 21, exhibit the same general behavior, including the crossover, as shown by the resistance.

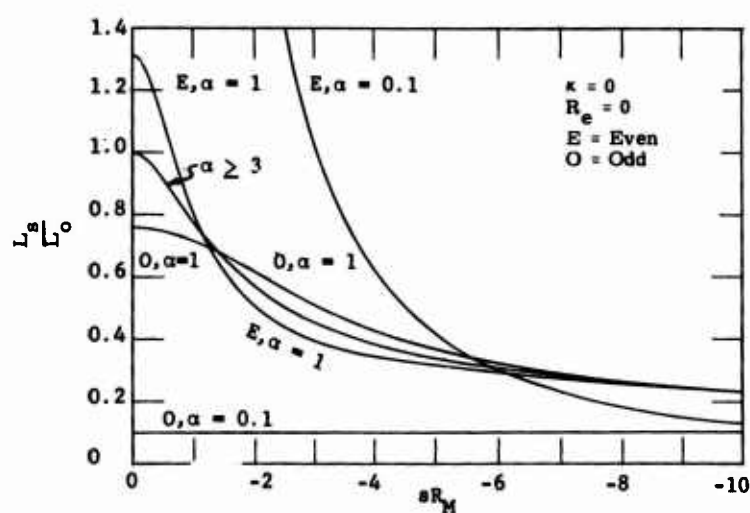


Fig. 18. Series inductance for even and odd excitation with $\kappa = 0$ as a function of sR_M and α .

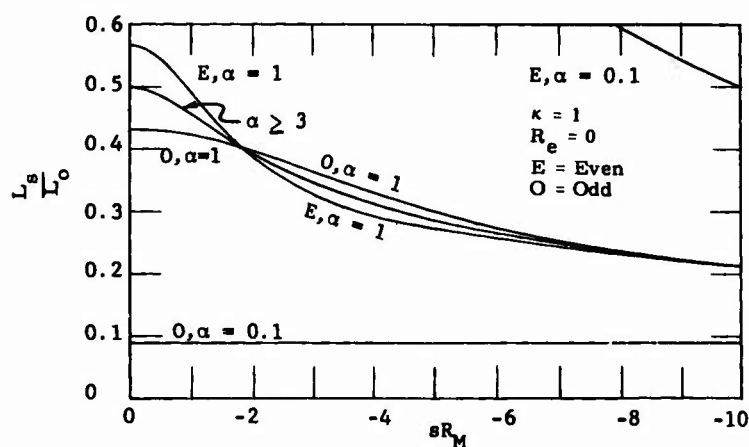


Fig. 19. Series inductance for even and odd excitation with $\kappa = 1$ as a function of sR_M and α .

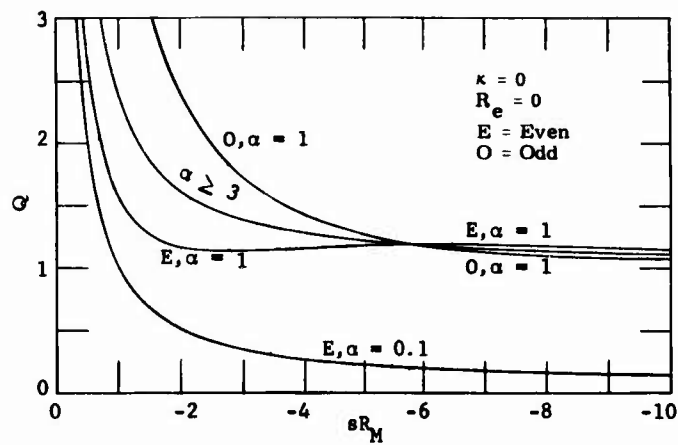


Fig. 20. Q for even and odd excitation with $\kappa = 0$ as a function of sR_M and α .

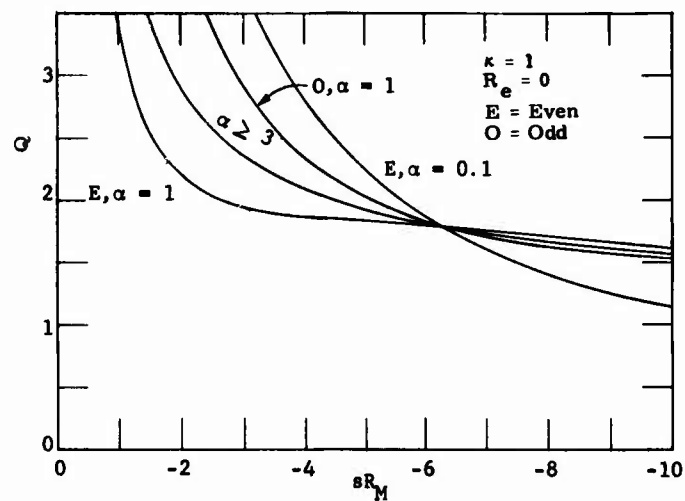


Fig. 21. Q for even and odd excitation with $\kappa = 1$ as a function of sR_M and α .

The discussion above shows that even excitation with small α is preferable for energy conversion. They may not be true for other applications, such as induction flowmeters, for which simplicity of construction is more important than efficiency or power density. Further comparison is brought out by the profile curves of section 3.7.

3.7 ELECTROMAGNETIC FIELD AND PRESSURE-GRADIENT PROFILES

The electromagnetic field and pressure-gradient or force profiles determined in sections 3.1 and 3.5 for a constant fluid velocity are plotted and discussed. They are

used to study skin effect, compare even and odd excitation, and to examine fluid velocity profiles in Section IV.

The electromagnetic field components are related to the vector potential by

$$\underline{B}_{fx} = \frac{\partial \underline{A}_f}{\partial y} \quad (93)$$

$$\underline{B}_{fy} = jk \underline{A}_f \quad (94)$$

$$\underline{E}_{fz} = -j \omega \underline{A}_f \quad (95)$$

$$\underline{J}_{fz} = -j \sigma_f (\omega - vk) \underline{A}_f. \quad (96)$$

The time-average electromagnetic force or pressure gradient is

$$\left\langle \frac{\partial p_{em}}{\partial x} \right\rangle = \sigma_f k (\omega - vk) \frac{\underline{A}_f \underline{A}_f^*}{2}. \quad (97)$$

For either excitation all field components are proportional to the vector potential except \underline{B}_{fx} , which is proportional to the vector potential for the opposite excitation. Plotting \underline{A}_f for both even and odd excitation will show how all components vary across the channel.

The magnitude and the magnitude squared of \underline{A}_f are plotted on a linear scale in Figs. 22 and 23 for several values of α , all for $|\underline{sR}_M| = 1$.^{*} The magnitude is also plotted on a semi-log scale in Fig. 24 to illustrate the exponential behavior. The magnitude squared, if plotted on a semi-log scale, would be identical to the magnitude but with twice the slope.

The curves are normalized to one at the edge of the channel to show the relative shape without considering absolute values. The constants by which each normalized curve is multiplied to obtain the absolute value, given in Table 2, vary so widely as to make it impractical to compare the un-normalized curves on one graph. Only the constants depend on the core properties.

For small $\gamma \sigma$, where the slit-channel approximation is valid, the even-excitation field is constant across the channel and the odd field is linear in y . This is valid for $\alpha \leq 0.1$ and $|\underline{sR}_M| \leq 10$ within 1%. At $\alpha = 0.1$ and $|\underline{sR}_M| = 10$ skin effect is negligible, $\delta_s/a = 4.3$.

For large α , skin effect becomes important. At $\alpha = 1.0$ and $|\underline{sR}_M| = 1$, $\delta_s/a = 0.91$, the even field has decreased at the center of the channel to 62% of its value at the edge.

^{*}The magnitude does not depend on the sign of \underline{sR}_M . Changing the sign reverses the angle only.

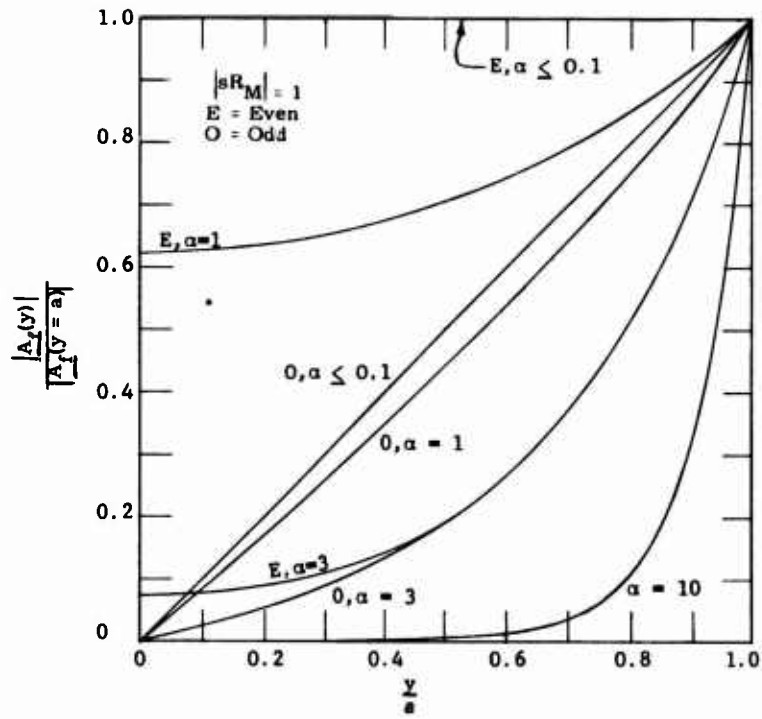


Fig. 22. Vector potential normalized to 1 at $y = a$ versus y/a .

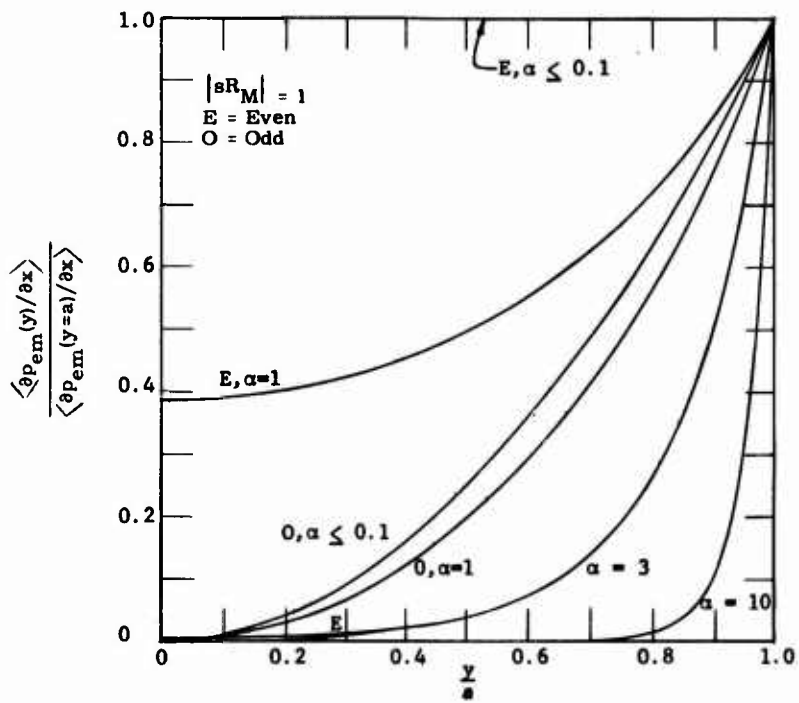


Fig. 23. Electromagnetic-pressure gradient normalized to 1 at $y = a$ versus y/a .

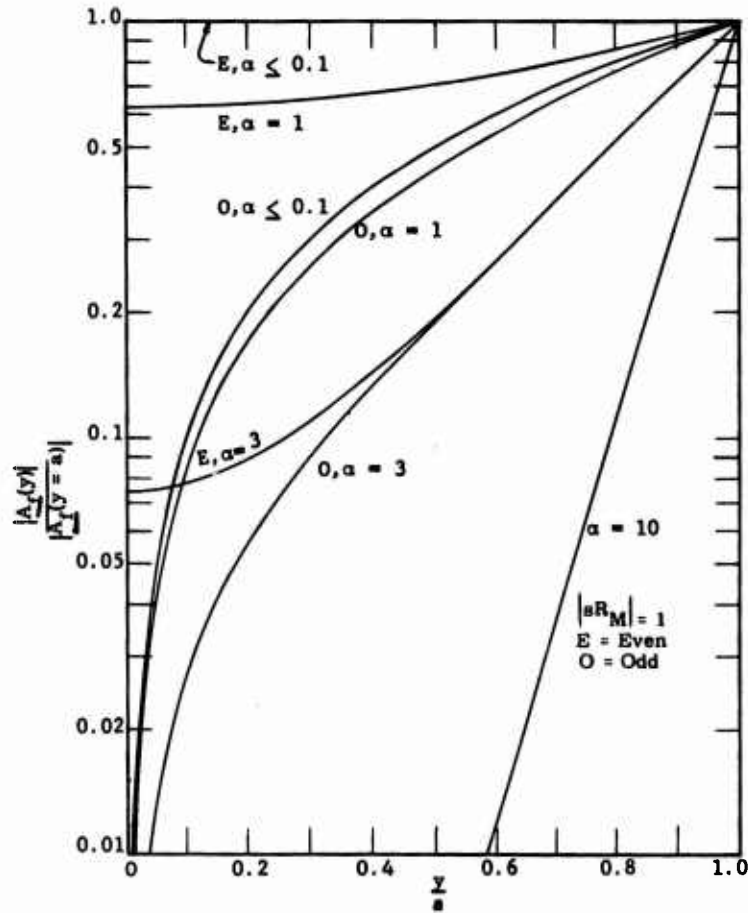


Fig. 24. Vector potential normalized to 1 at $y = a$ versus y/a (semi-log scale).

There has been little change in the odd field because the contributions from the two exciting windings subtract, so that the decreases partly cancel and the total field is not changed as much. For even excitation they add, and the change is doubled. The semi-log curves for this case are not linear because the contributions from the two windings have to be considered, and the sum of two exponentials does not plot linearly. This is seen from Fig. 24 because the even and odd-excitation curves do not start with the same slope, as they do for larger α when only one excitation term is important at the edge.

For $\alpha \geq 3$ Eq. 89 is satisfied for any sR_M , $(\delta_s/a) \leq (1/3)$, and skin effect dominates the machine behavior. The field attenuation is large, so that the fluid sees only the field attributable to the nearer exciting plate, and only a strip along each exciting plate

enters the interaction. The profiles are the same for either excitation except near the center, where the fields from the two windings become of the same magnitude. Since it is no longer necessary to consider both contributions, the semi-log curves are linear except near the center. For $\alpha = 3$ and $|sR_M| = 1$, $(\delta_s/a) = 0.3$ and the magnitude of A_f has decreased to $1/d$ of its value at the edge at $(y/a) = 0.7$, as expected. A similar result is obtained for $\alpha = 10$.

The multiplicative constants for each curve (Table 2) also provide information about machine performance. The average value of the pressure gradient from Fig. 23 multiplied by the appropriate constant is proportional to the power level of the machine. The best results are obtained for even excitation and small α , the worst for odd excitation and small α , while for large α the two become identical. This agrees with the conclusions of section 3.6.

Table 2. Multiplicative constants for vector potential and electromagnetic pressure-gradient profiles, all for $|sR_M| = 1$, $\kappa = 0$, and $R_{Mc} = 0$.

α	Magnitude		Pressure	
	Even	Odd	Even	Odd
0.01	7071.3	1.0	50.0	1.00×10^{-6}
0.1	70.9	0.997	5.03	9.93×10^{-4}
1.0	0.963	0.734	0.927	0.539
3.0	0.280	0.281	2.11	2.13
10.0	0.084	0.084	7.07	7.07

In addition, multiply magnitude by $(\mu_f NIa)$, pressure by $\left(\frac{\mu_f (NI)^2}{2a} \right)$.

3.8 UNBALANCED EXCITATION

Unbalanced excitation, when the two exciting phases of the MHD induction machine are not equal, is an important practical consideration. Unbalance may exist because of unequal generator loads or nonidentical coil structures for the two phases. The single-phase machine, with only one exciting phase, is a special case. Unbalanced excitation is treated as a direct extension of the previous work by superposition of oppositely traveling fields. The space and time-average powers are orthogonal and, therefore, additive. The general solution is obtained and specialized to the single-phase machine.

Consider two unequal exciting phases with turns densities $N_1 \cos kx$ and $N_2 \sin kx$ excited by currents $I_1 \cos \omega t$ and $I_2 \sin \omega t$. The total surface current is

$$\vec{K} = \vec{i}_z K_+ \cos (\omega t - kx) + \vec{i}_z K_- \cos (\omega t + kx), \tag{98}$$

where

$$K_+ = \frac{N_1 I_1 + N_2 I_2}{2} \quad (99)$$

$$K_- = \frac{N_1 I_1 - N_2 I_2}{2} \quad (100)$$

The unbalanced surface current is represented by forward and backward traveling waves with sum and difference amplitudes, where + and - subscripts are used for the two traveling waves, and 1 and 2 for the two phases.

Superposition applies to the field solution, since the model is linear; the field is the sum of the responses resulting from the forward and backward excitations with the appropriate amplitudes and slips. Superposition also applies to the space-average power even though it involves products. To see this, consider the time-average "power" product of

$$F = \text{Re} \left\{ \underline{F}_+ e^{j(\omega t - kx)} + \underline{F}_- e^{j(\omega t + kx)} \right\} \quad (101)$$

and

$$G = \text{Re} \left\{ \underline{G}_+ e^{j(\omega t - kx)} + \underline{G}_- e^{j(\omega t + kx)} \right\}, \quad (102)$$

which is

$$\langle P \rangle = \frac{\underline{F} \underline{G}^*}{2} = \frac{\underline{F}_+ \underline{G}_+^*}{2} + \frac{\underline{F}_- \underline{G}_-^*}{2} + \frac{\underline{F}_+ \underline{G}_-^*}{2} e^{-j2kx} + \frac{\underline{F}_- \underline{G}_+^*}{2} e^{j2kx}, \quad (103)$$

where F and G may be any periodic quantities. Averaging this over any multiple of a half-wavelength causes the cross terms to drop out.

Unbalanced excitation is easily handled by superimposing the previous results. For the excitation of Eq. 98, the vector potential in the fluid is

$$A_f = \text{Re} \left\{ \underline{A}_{f+} e^{j(\omega t - kx)} + \underline{A}_{f-} e^{j(\omega t + kx)} \right\}, \quad (104)$$

where

$$\underline{A}_{f\pm} = \frac{\mu_f K_{\pm} \cosh \gamma_{\pm} ky}{k(\gamma_{\pm} \sinh \gamma_{\pm} a + \kappa \delta \cosh \gamma_{\pm} a)} \quad (105a)$$

$$\gamma_{\pm}^2 = 1 + js_{\pm} R_M \quad (105b)$$

$$s_{\pm} = \frac{v_s \mp v}{v_s}, \quad (105c)$$

and δ depends only on the magnitude of synchronous speed, not the direction. All other field quantities can be determined from A_f .

The slips for the two waves are symmetric about $s = 1$, which corresponds to $v = 0$. For $s > 1$ the machine acts as a pure loss or damper, dissipating both mechanical and electrical input powers in the fluid conductivity. Thus, the backward wave will oppose the forward wave, decreasing the power and efficiency. Its effect may be small, because of the difference in slip, if R_M is large. The opposition of the two waves is also seen from the field-fluid interaction, since the force tries to drag the fluid along with the field.

The impedance calculation is slightly more complicated because the voltages and turns densities are different for the two coils. The voltages, from Eq. 25, are

$$\underline{V}_1 = \frac{2\pi cN_1^2 I_1}{k\sigma_s} + j \frac{R_{o1}}{N_1} \left[\frac{K_+}{\gamma_+ \tanh \gamma_+ \alpha + \kappa\delta} + \frac{K_-}{\gamma_- \tanh \gamma_- \alpha + \kappa\delta} \right] \quad (106)$$

and

$$\underline{V}_2 = \frac{2\pi cN_2^2 I_2}{jk\sigma_s} + \frac{R_{o2}}{N_2} \left[\frac{K_+}{\gamma_+ \tanh \gamma_+ \alpha + \kappa\delta} - \frac{K_-}{\gamma_- \tanh \gamma_- \alpha + \kappa\delta} \right] \quad (107)$$

From these,

$$R_{si} = \frac{2\pi cN_i^2}{k\sigma_s} - \frac{R_{oi}}{N_i I_i} \operatorname{Im} \left\{ \frac{K_+}{\gamma_+ \tanh \gamma_+ \alpha + \kappa\delta} \pm \frac{K_-}{\gamma_- \tanh \gamma_- \alpha + \kappa\delta} \right\} \quad (108)$$

and

$$L_{si} = \frac{L_{oi}}{N_i I_i} \operatorname{Re} \left\{ \frac{K_+}{\gamma_+ \tanh \gamma_+ \alpha + \kappa\delta} \pm \frac{K_-}{\gamma_- \tanh \gamma_- \alpha + \kappa\delta} \right\}, \quad (109)$$

where

$$R_{oi} = \omega L_{oi} = \frac{2\pi \mu_f v_s cN_i^2}{k}, \quad (110)$$

and i is either 1 or 2 for the two coils. This reduces to the balanced impedance for

$$N_1 I_1 = N_2 I_2 = NI. \quad (111)$$

The impedance can be simplified for a slit-channel machine as was done previously.

The single-phase machine, a special case, has only one phase or winding, so that the two traveling current wave amplitudes are equal. The fields are not equal, however, because of the difference in slip. The equivalent circuit values are

$$R_s = R_e - \frac{R_o}{2} \operatorname{Im} \left\{ \frac{1}{\gamma_+ \tanh \gamma_+ a + \kappa \delta} + \frac{1}{\gamma_- \tanh \gamma_- a + \kappa \delta} \right\} \quad (112)$$

and

$$L_s = \frac{L_o}{2} \operatorname{Re} \left\{ \frac{1}{\gamma_+ \tanh \gamma_+ a + \kappa \delta} + \frac{1}{\gamma_- \tanh \gamma_- a + \kappa \delta} \right\}, \quad (113)$$

where R_e , R_o , and L_o are the same as in the two-phase case. The best that can be done, if the backward wave is negligible, is 1/4 of the two-phase power output because the forward wave is half the previous value and there is only one set of coils

The single-phase series resistance is plotted in Figs. 25 and 26 as a function of fluid speed for two values of R_{Ma} . Coil and core losses are neglected, and the slit-channel approximation is used. The separate forward and backward-wave contributions are also shown. The two sets of curves clearly demonstrate that the effect of the backward wave becomes smaller as R_{Ma} increases.

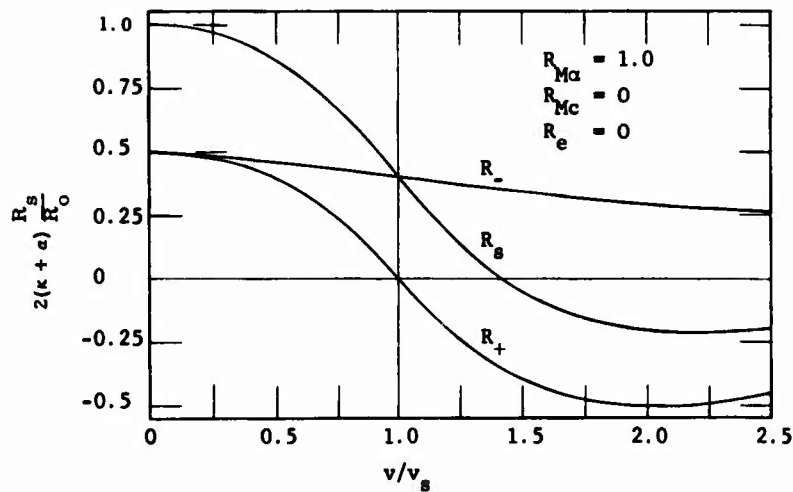


Fig. 25. Series resistance of single-phase, slit-channel machine for $R_{Ma} = 1.0$.

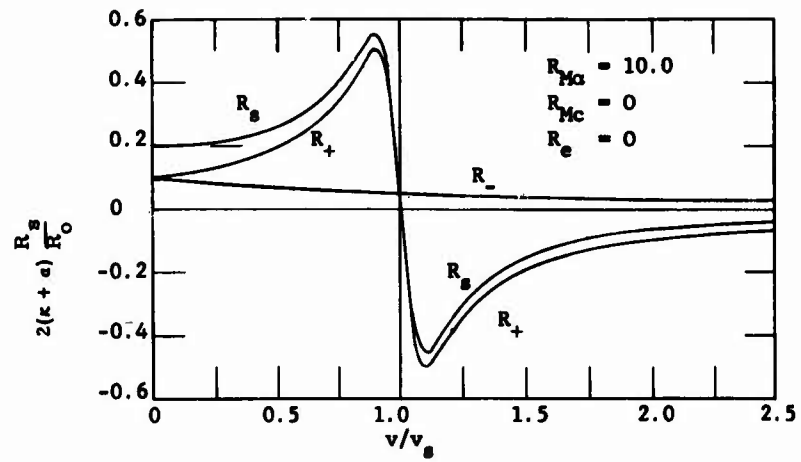


Fig. 26. Series resistance of single-phase, slit-channel machine
for $R_{Ma} = 10.0$.

IV. LAMINAR FLOW

4.1 INTRODUCTION

In the previous analysis of the MHD induction machine only constant fluid velocity has been considered to illustrate the principles of operation. The fluid velocity profile and viscosity will have important effects for two reasons:

1. The velocity profile may drastically alter the power flow.
2. The viscous losses may be large.

An exact consideration of profile effects is impossible, but a solution is obtained for laminar flow with reasonable approximations.

The laminar-flow solution gives insight into the mutual interaction. The flow in a practical machine, however, will probably be highly turbulent, because of the high velocities or (hydraulic) Reynolds numbers R_e required to achieve reasonable power densities. Turbulence in induction-driven flows is not fully understood, so that the limits on R_e for laminar flow as a function of the applied magnetic field and flow parameters are unknown. A qualitative idea of turbulence, the turbulent velocity profile, and the effect of turbulence on machine performance are discussed in Section V.

The fluid velocity and electromagnetic field are determined from Eqs. 9 and 13. The equations can be solved only for laminar flow, as little is known about solutions for turbulent flows either with or without a magnetic field. Even then an analytical solution is clearly impossible, because of the nonlinear terms and the two-directional coupling, so that a reasonable approximation is made – that the fluid velocity is laminar, in the x-direction, and independent of x and t. This approximation and the resulting equations are discussed in section 4.2. An analytical solution of the simplified equations is obtained for a slit channel in section 4.3. In general, even the simplified equations can only be solved numerically because the nonlinear terms and the two-directional coupling remain. The numerical techniques and results are discussed in sections 4.4, 4.5, and 4.6.

4.2 APPROXIMATE EQUATIONS FOR LAMINAR FLOW

To solve Eqs. 9 and 13, they must be simplified, because of the product type of nonlinearities. Linearization with the constant-velocity solution used as the starting point is not valid for two reasons: the constant velocity does not match the boundary conditions, and the perturbations are not small. A power-series solution in the magnetic Reynolds number is not desired because it would be limited to small R_M , which does not include the range of interest for power generation. Writing \vec{v} and \vec{A}_f as Fourier series in $e^{jn(\omega t - kx)}$, because of the simple $e^{j(\omega t - kx)}$ excitation of the current sheets, gives an infinite number of completely coupled equations that still involve products and derivatives with respect to y. These equations are not amenable to solution.

The equations are simplified by assuming the velocity to be completely in the x-direction. The model implied by this assumption replaces the fluid by many thin strips which slide over each other with friction but do not move in the y-direction; that is, there is no mixing. The continuity equation, (5), then requires \vec{v} to be independent of x. The electromagnetic pressure gradient on each strip, $(\vec{J}_f \times \vec{B}_f)_x$, consists of a constant term plus a second harmonic in $(\omega t - kx)$, since \vec{J}_f and \vec{B}_f vary as $e^{j(\omega t - kx)}$ for a velocity independent of x and t. The total force on a strip per wavelength in the x-direction is a constant, so that \vec{v} should not have any time dependence for an incompressible fluid. Thus,

$$\vec{v} = \vec{i}_x v(y) \quad (114)$$

is a consistent and reasonable approximation to the actual flow, provided that the transverse fluid velocity is small compared with the velocity along the machine.

An idea of the relative sizes of v_x and v_y is obtained from the equations. The velocity can be written in the form

$$\vec{v} = \vec{i}_x v_0(y) + \vec{v}_1(x, y, t), \quad (115)$$

since the transverse velocity can have no average value. Here v_0 is the average flow, and \vec{v}_1 is the moving vortex-type motion induced by the electromagnetic force, because of its nonzero curl and x- and t-dependence. The driving terms for the velocity, the x and y components of $\vec{J}_f \times \vec{B}_f$, have the ratio

$$\left| \frac{(\vec{J}_f \times \vec{B}_f)_y}{(\vec{J}_f \times \vec{B}_f)_x} \right| = \frac{B_{fx}}{B_{fy}} = \gamma \tanh \gamma a, \quad (116)$$

where the last expression is for the constant-velocity fields. The ratio is small for a slit channel, $\gamma a \ll 1$. Also, the effect of the y force component is diminished because its time average does not cause a time-average velocity.

Penhune⁴³ showed that the fluid behaves like a lowpass filter; that is, for equal applied DC and AC forces the AC velocity is small compared with the DC velocity.^{*} This means that $v_{1x} \ll v_0$; and, since the y component of the force is small for a slit channel, v_{1y} is small compared with v_{1x} and thus with v_0 , as assumed. The approximation becomes worse for a wide channel, where B_{fx} and B_{fy} are of the same order of magnitude and the y variations of the field are large. This case is poor for energy conversion, as shown in Section III and section 4.6.

*For mercury in a channel 2 cm wide ($a = 1\text{cm}$) driven by a DC and an equal-amplitude AC force at a frequency of 120 cps (the second-harmonic force of a 60-cps machine), Penhune found the ratio of the AC rms velocity to the DC velocity, both averaged over the channel, to be 3.5×10^{-6} .⁴⁴

With this one approximation (Eq. 114) the equations become

$$\frac{d^2 \underline{A}_f}{dy^2} - k^2 \left[1 + jR_M \left(1 - \frac{v}{v_s} \right) \right] \underline{A}_f = 0, \quad (117)$$

and

$$\eta \frac{d^2 v}{dy^2} = \frac{\partial p}{\partial x} + J_{fz} B_{fy}, \quad (118)$$

where complex notation is used in (117), the vector potential has only a z component and varies as $e^{j(\omega t - kx)}$ as before, and J_{fz} and B_{fy} are determined in terms of \underline{A}_f . The left-hand side of Eq. 118 is independent of x and t, but the electromagnetic pressure gradient consists of a constant plus a second harmonic in $(\omega t - kx)$. The pressure gradient must absorb the second harmonic, but the total pressure across a wavelength of the machine is a constant because the second harmonic integrates to zero. The pressure difference across the machine, supplied by the fluid source, does not depend on t and must also be independent of y. The time average or the space average over x (the two are equivalent) of the pressure gradient is a constant,

$$\langle \frac{\partial p}{\partial x} \rangle = p_o. \quad (119)$$

Averaging Eq. 118 with respect to x or t and eliminating J_{fz} and B_{fy} gives

$$\eta \frac{d^2 v}{dy^2} = p_o - \sigma_f k^2 (v_s - v) \frac{\underline{A}_f \underline{A}_f^*}{2}. \quad (120)$$

The equations are put in a more tractable form by defining the normalized variables

$$\tilde{y} = \frac{y}{a} \quad (121)$$

$$u(y) = \frac{v(\tilde{y})}{\bar{v}} \quad (122)$$

$$\underline{F}(\tilde{y}) = \frac{\underline{A}_f(\tilde{y})}{\underline{A}_{fo}}, \quad (123)$$

where a is the channel half-height, \bar{v} is the space-average velocity, and \underline{A}_{fo} , the vector potential at the center of the channel, is determined by the boundary conditions. In terms of v_s and the average slip \bar{s} ,

$$\bar{v} = (1 - \bar{s}) v_s, \quad (124)$$

which is considered to be a constant of the solution.

The Hartmann number for DC flows is

$$M_o^2 = \frac{\sigma_f a^2}{\eta} B_o^2, \quad (125)$$

where B_o is the transverse magnetic field. Defining an effective Hartmann number $M(\tilde{y})$ for the induction machine,

$$M^2 = \frac{\sigma_f a^2}{\eta} \frac{A_f A_f^*}{2}, \quad (126)$$

in terms of the rms transverse magnetic field, the normalized equations become

$$\frac{d^2 \underline{F}}{dy^2} - a^2 \left[1 + jR_M - jR_M (1 - \bar{s}) u \right] \underline{F} = 0, \quad (127)$$

and

$$\frac{d^2 u}{d\tilde{y}^2} - M^2 u = \frac{a^2 p_o}{\eta (1 - \bar{s}) v_s} - \frac{M^2}{(1 - \bar{s})}. \quad (128)$$

Here, M is a function of \tilde{y} , and becomes a constant only for a slit channel. All terms are symmetric except \underline{F} , which is symmetric or antisymmetric for even or odd excitation.

Equation 128 is identical to the Hartmann profile equation for a DC generator in terms of the loading factor

$$K_{dc} = \frac{-E}{\bar{v} B_o} = \frac{R_o}{R_i + R_o}, \quad (129)$$

where R_i and R_o are the internal fluid and external load resistances. The equivalent loading factor for the induction generator is

$$K_{ind} = \frac{P_s}{P_s - P_r} = \frac{1}{1 - \bar{s}}. \quad (130)$$

In both generators K varies from 0 for a short circuit or large interaction to 1 for an open circuit or no interaction.

The original set of equations has been simplified to two coupled nonlinear ordinary differential equations. An analytical solution, possible only for a slit channel, is given in section 4.3. Equation 127 can be solved for $\underline{F}(\tilde{y})$ if the velocity $u(\tilde{y})$ is specified. The equation is linear but with a varying coefficient, so that analytical techniques are not available and numerical methods must be used. Likewise, Eq. 128 can be solved for u if \underline{A}_f is specified, again numerically. The techniques used to obtain the numerical solutions and some of the results are discussed in sections 4.4 and 4.5. Both methods are tested against known cases. The techniques developed to solve the equations separately are then coupled together to obtain an exact numerical solution for laminar flow by an iterative procedure in section 4.6.

The solution could also be obtained by series techniques. Penhune* used a power series in R_M after making the same assumptions about the velocity. The resulting infinite set of equations can be solved term by term to the desired accuracy. For energy conversion, solutions are desired for large R_M , so that the series approach may not be valid.⁴⁶ The present approach is easier to use and more flexible, as it can handle turbulence to a limited extent.

The electromagnetic powers, determined from Eqs. 26, 28, and 30, are rewritten in terms of the normalized variables as

$$\frac{P_s}{P_o} = - \frac{A'_{fo}}{A'_{fo}} \frac{A'^*_{fo}}{A'^*_{fo}} \alpha \operatorname{Im} \left\{ \underline{F} \frac{d\underline{F}^*}{d\tilde{y}} \right\} \bigg|_{\tilde{y}=1} \quad (131)$$

$$\frac{P_m}{P_o} = \frac{A'_{fo}}{A'_{fo}} \frac{A'^*_{fo}}{A'^*_{fo}} \alpha^3 R_M (1 - \bar{s}) \int_0^1 \left[1 - (1 - \bar{s}) u \right] u \underline{F} \underline{F}^* d\tilde{y} \quad (132)$$

$$\frac{P_r}{P_o} = \frac{A'_{fo}}{A'_{fo}} \frac{A'^*_{fo}}{A'^*_{fo}} \alpha^3 R_M \int_0^1 \left[1 - (1 - \bar{s}) u \right]^2 \underline{F} \underline{F}^* d\tilde{y}. \quad (133)$$

Here,

$$\underline{A'_{fo}} = \frac{A_{fo}}{\mu_f N l a} \quad (134)$$

is the normalized vector potential with the excitation magnitude removed, chosen for convenience in later work. The simple power relations of Eq. 68 and 69 are replaced

*Penhune solved for the magnetic field rather than the vector potential, but the equations are similar.⁴⁵

by a relation between the integrals. In general, P_r and P_m are increased over their constant-velocity values for a generator, because of the circulating currents set up, since the velocity drops below synchronous speed near the walls. This region acts as a pump, and the net behavior of the machine may be changed from a generator to a pump or damper.

4.3 SLIT-CHANNEL SOLUTION

For a slit channel, $\gamma a \ll 1$, the equations of section 4.2 can be simplified to yield an analytical solution. The electromagnetic field and the vector potential are independent of y , and the total current in the fluid at a given value of x is thus

$$\int_{-a}^a \underline{J_{fz}} dy = -j 2\sigma_f a (v_s - \bar{v}) \underline{A_f}, \quad (135)$$

which is independent of the velocity profile. This means that the vector potential can be determined first, and then the profile and powers. The vector potential must be calculated from the integral form of Eq. 5a, as in Appendix G, because of the neglected y -dependence of the field. Noting that the form of $\underline{A_c}$, Eq. 40, is unchanged by the approximation, and using boundary condition Eq. 20 and Eq. 135, gives

$$\underline{A_f} = \frac{\mu_f NI}{k(\gamma^2 a + \kappa \delta)}, \quad (136)$$

where γ^2 now depends on the average slip \bar{s} . This is the same as the slit-channel field found in Section III for a constant velocity.

The normalized velocity, obtained from Eq. 128 for M constant, is the Hartmann profile,

$$u(\tilde{y}) = \frac{\left(1 - \frac{\cosh M\tilde{y}}{\cosh M}\right)}{\left(1 - \frac{\tanh M}{M}\right)}; \quad (137)$$

so that, for a slit channel and laminar flow, the profile for the induction machine is identical to that for a DC machine with a Hartmann number based on the rms transverse magnetic field. The pressure gradient p_0 does not affect the profile shape. It is not an independent constant, but has to be adjusted to provide the specified flow rate \bar{v} . The Hartmann profile is plotted in Fig. 27 for several values of M . The curve for $M = 0$ is the parabolic profile of laminar hydrodynamic flow.

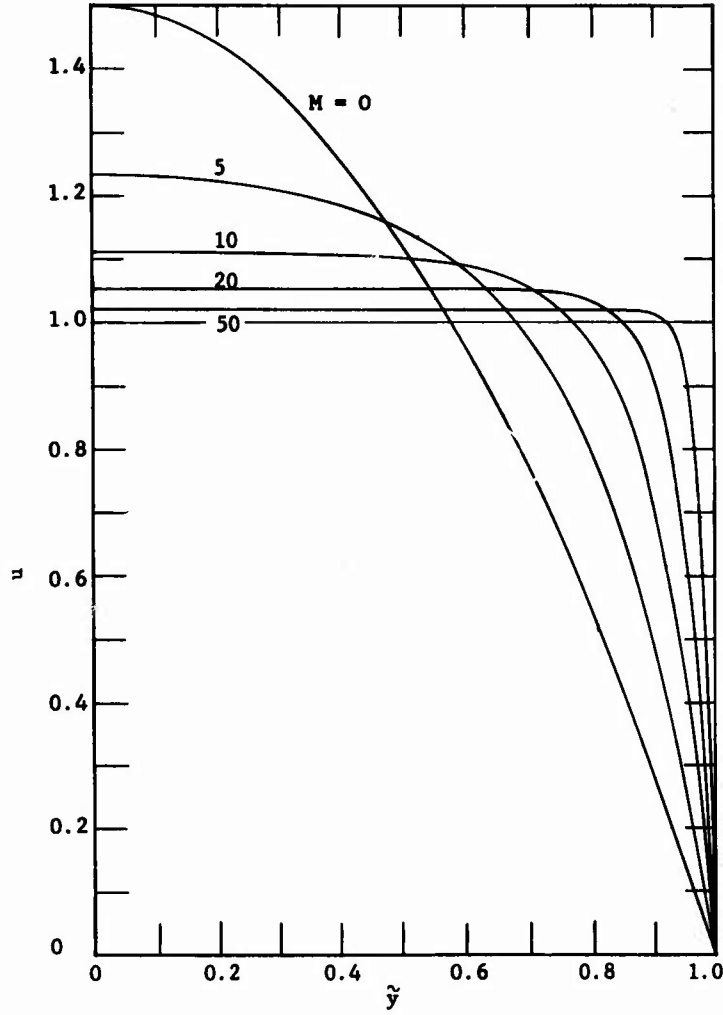


Fig. 27. Normalized Hartmann velocity profiles.

The powers for the slit-channel machine, from Eqs. 131 – 134, are

$$P_s = P_o \frac{\alpha \bar{s} R_M}{(\gamma^2 \alpha + \kappa \delta) (\gamma^{*2} \alpha + \kappa \delta^*)}, \quad (138)$$

$$P_m = (1 - \bar{s}) P_s F_m(u), \quad (139)$$

$$P_r = \bar{s} P_s F_r(u). \quad (140)$$

Here, P_s is independent of the profile, since it depends only on the fields. The equations are identical with the results of section 3.3, except for the profile factors

$$F_m(u) = \frac{1}{\bar{s}} \left[1 - (1 - \bar{s}) \overline{u^2} \right] \quad (141)$$

and

$$F_r(u) = \frac{1}{\bar{s}^2} \left[2\bar{s} - 1 + (1 - \bar{s})^2 \overline{u^2} \right], \quad (142)$$

where

$$\overline{u^2} = \int_0^1 (u(\tilde{y}))^2 d\tilde{y}, \quad (143)$$

the average of the velocity squared, is always ≥ 1 . For a generator, F_m and F_r are ≥ 1 , and the I^2R losses are increased for the same power output. For a pump, $F_m \leq 1$.

The profile factors for a Hartmann profile are

$$F_m = \frac{1}{\bar{s}} \left[1 - \frac{(1 - \bar{s})}{\left(1 - \frac{1}{M}\right)^2} \left(1 - \frac{3}{2M}\right) \right], \quad (144)$$

and

$$F_r = \frac{1}{\bar{s}^2} \left[2\bar{s} - 1 + \frac{(1 - \bar{s})^2}{\left(1 - \frac{1}{M}\right)^2} \left(1 - \frac{3}{2M}\right) \right], \quad (145)$$

using the approximations for $M > 4$. The exact expressions, plotted in Figs. 28 and 29 for several negative values of \bar{s} , show that the factors increase as $|\bar{s}|$ decreases and as the profile deviates from a constant. This is to be expected for a generator because, as \bar{s} approaches zero or as the profile becomes more rounded, the size and relative importance of the positive-slip region near the wall increases. In this region the machine is acting as a pump, so that the losses resulting from circulating currents are increased.

The factors for a parabolic profile, corresponding to $M = 0$, are

$$F_m = \frac{6}{5} - \frac{1}{5\bar{s}}, \quad (146)$$

and

$$F_r = \frac{6}{5} - \frac{2}{5\bar{s}} + \frac{1}{5\bar{s}^2}, \quad (147)$$

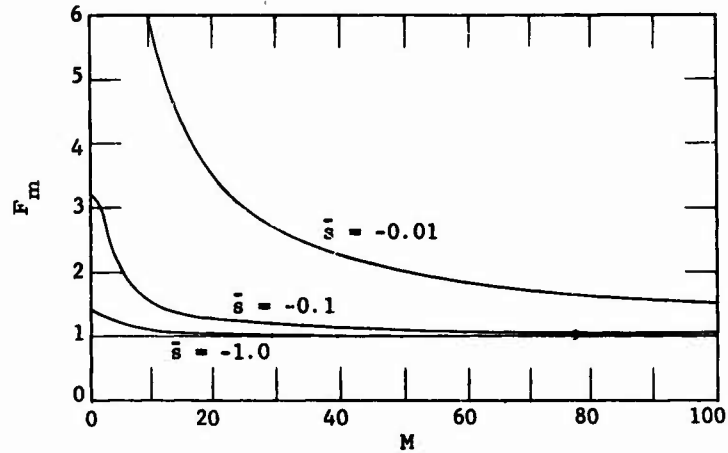


Fig. 28. F_m for Hartmann profile.

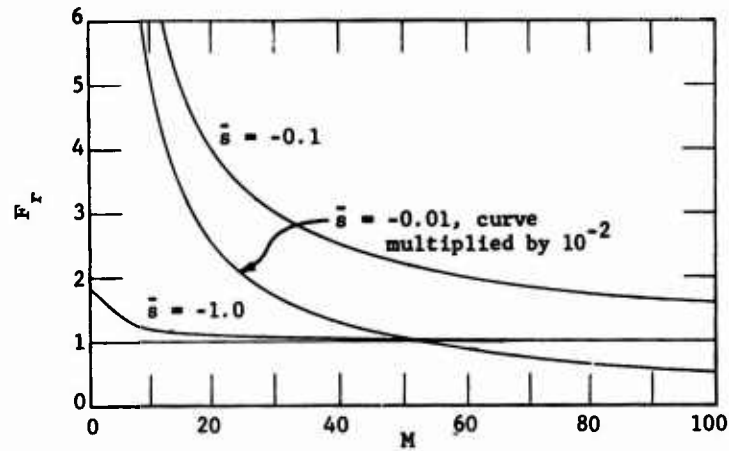


Fig. 29. F_r for Hartmann profile.

which are worse than for the Hartmann profile, as shown in Figs. 28 and 29. The factors for several turbulent profiles, discussed in section 5.1, are close to Hartmann because they are relatively flat.

The generator efficiency is

$$e_g = \frac{1}{(1 - \bar{s}) F_m}, \quad (148)$$

since P_s is unchanged but the input power is increased by F_m . At $\bar{s} = 0$ there is no power output, but the circulating currents still exist, there is power input, and the efficiency is zero. There is a peak in the efficiency, so that decreasing $|\bar{s}|$ further results in a poorer efficiency because more of the fluid is pumped, in contrast to the

constant-velocity case where e_g approaches one as \bar{s} approaches zero. Curves of e_g versus \bar{s} for several values of M are shown in Fig. 30.

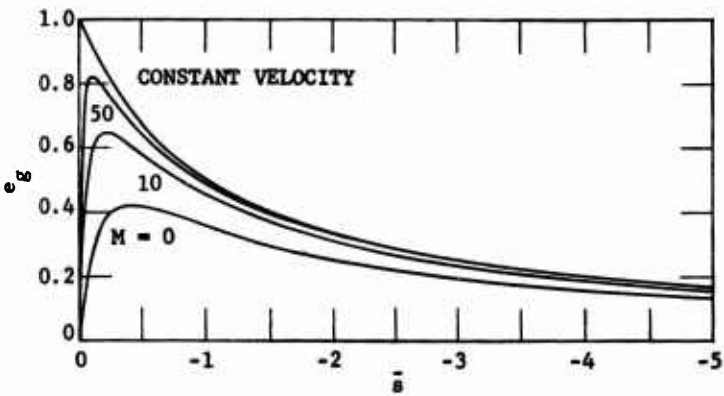


Fig. 30. Generator efficiency for slit-channel machine with Hartmann profile.

The viscous loss for laminar flow can be found once the velocity profile is known. This is done in Appendix D, and the results are plotted in Fig. D-3 for the Hartmann profile. The viscous loss increases with M , so that the improvement in F_m is not free, but this is not serious, provided the viscous loss is small as it must be for a practical machine. The viscous power cannot be compared directly with P_m until the exciting surface current NI is specified.

These results, derived by assuming $\gamma\alpha \ll 1$, are valid for a much larger range than expected. Comparison with the numerical results of sections 4.4–4.6 shows good agreement for α as large as 0.1; that is, errors of a few per cent for $\alpha = 0.1$ and $|sR_M|$ up to 100.

4.4 ELECTROMAGNETIC FIELDS AND POWERS FOR A KNOWN VELOCITY

The vector potential in the fluid is determined from Eq. 127 when the velocity is specified. The result when the profile for ordinary hydrodynamic flow, either laminar or turbulent, is used in the approximate solution when the electromagnetic force is small compared with the viscous force. Otherwise the result may not correspond to an actual flow, but still gives information on the dependence of the fields and powers on the velocity profile.

Equation 127 is a linear homogeneous second-order differential equation for $\underline{F}(\tilde{y})$ in terms of $u(\tilde{y})$ and the machine parameters \bar{s} , R_M , and α . The core properties and excitation appear only in the normalization constant A_{fo} , which is determined from the boundary conditions. The best approach, both for finding the powers and for coupling the two equations together in an iterative procedure, is to solve the equation numerically. Several numerical methods are discussed in Appendix E, and the preferred method, method four, is chosen by testing on the case $u(\tilde{y}) = 1$, for which the exact solution is known.

The solution of Eq. 127 is a boundary-value problem with conditions at $\tilde{y} = \pm 1$, but the numerical method requires two initial values for the second-order equation. Considering only even excitation,* and using symmetry to solve for only half the field and flow pattern, one initial value is that the derivative is zero at the center of the channel. For the second initial value $\underline{F}(0)$ is taken to be unity, hence the definition of \underline{A}_{fo} as the vector potential at the center. Since Eq. 127 is homogeneous, this procedure gives no difficulty, and the numerical solution is simply scaled to match the boundary conditions.

Defining a new variable,

$$\underline{DF}(\tilde{y}) = \frac{d\underline{F}(\tilde{y})}{d\tilde{y}} \quad , \quad (149)$$

the initial conditions are

$$\underline{DF}(0) = 0 \quad (150)$$

$$\underline{F}(0) = 1 \quad . \quad (151)$$

The boundary conditions at $\tilde{y} = 1$ (Eqs. 20 and 21) and the form of the vector potential in the core, Eq. 40, are independent of the velocity profile, so that the constants are

$$\underline{A}_{fo} = \frac{\mu_f N I a}{\underline{DF}(1) + \alpha \kappa \delta \underline{F}(1)} \quad (152)$$

and

$$\underline{A}_{c1} = \frac{\mu_f N I a \underline{F}(1) e^{\delta \alpha}}{\underline{DF}(1) + \alpha \kappa \delta \underline{F}(1)} \quad (153)$$

where $\underline{F}(1)$ and $\underline{DF}(1)$ are determined from the numerical solution. For the numerical results \underline{A}'_{fo} , defined in Eq. 134 as the vector potential with the excitation magnitude $\mu_f N I a$ removed, is used because $\mu_f N I a$ is purely a scale factor.

The powers are determined from Eqs. 131 – 133 by using the known field solution. The integrations for P_m and P_r are performed numerically by using the techniques of Appendix E.

The numerical integration procedures were applied to the parabolic and Hartmann profiles, with the constant-velocity case used as a check on the accuracy. Several turbulent profiles were also used. Graphical presentation of the results for $\underline{F}(y)$ is

*For odd excitation the initial values are interchanged to satisfy the antisymmetry of $\underline{F}_o(\tilde{y})$. Otherwise, the procedure remains the same.

inconvenient because the profile change is small for small $\gamma\alpha$, while for large $\gamma\alpha$, \underline{F} varies by many orders of magnitude, so that comparison is restricted to tabulation. Since \underline{F} and \underline{DF} are always the same at $\tilde{y} = 0$, the change with profile is conveniently represented in terms of the values at $\tilde{y} = 1$, tabulated as $\underline{F}\underline{F}^*|_{\tilde{y}=1}$ and $\underline{A}'_{fo} \underline{A}'^*_{fo} = (1/\underline{DF} \underline{DF}^*)|_{\tilde{y}=1}$ for $\kappa = 0$. Here, \underline{A}'_{fo} is used because it determines the power level of the machine. The powers are presented by using P_s/P_o and the generator efficiency. Viscous losses are not considered.

The effect of varying α is shown in Table 3, where all data are for $\bar{s} = -1$, and $R_M = 1$. Those for $\alpha = 0.01$ and 0.1 agree with the slit-channel theory within 1%. Surprisingly, the slit-channel results are valid to a much larger $\gamma\alpha$ than expected; all cases tested for $\alpha = 0.1$ are close to the slit-channel predictions. Even for the extreme case of $\alpha = 0.1$, $\bar{s}R_M = -200$, and $|\gamma\alpha| = 1.4$ (Table 4), the powers are within 10% of the slit-channel theory and the efficiencies are even closer, despite the field variation across the channel. Also P_s and e_g for $\alpha = 1$ (Table 3) are within 10%, except for the parabolic profile. Still to be checked for small $\gamma\alpha$ is the difference of the velocity profile from Hartmann.

Table 3. Numerical integration results for the electromagnetic fields and powers, varying α , $\kappa = 0$.

\bar{s}	R_M	α	Profile [†]	$\underline{F}\underline{F}^* _{\tilde{y}=1}$	$\underline{A}'_{fo} \underline{A}'^*_{fo}$	P_s/P_o	$e_g\%$
- 1.0	1.0	0.01	C	1.00	5.00×10^7	- 50.0	50.0
			P	1.00	5.00	- 50.0	35.7
			H-10	1.00	5.00	- 50.0	45.5
			H-50	1.00	5.00	- 50.0	49.0
- 1.0	1.0	0.1	C	1.01	4.98×10^3	- 5.00	50.0
			P	1.01	4.98	- 4.98	35.7
			H-10	1.01	4.98	- 4.99	45.5
			H-50	1.01	4.98	- 5.00	49.0
- 1.0	1.0	1.0	C	2.58	0.359	- 0.518	50.0
			P	2.91	0.336	- 0.350	33.2
			H-10	2.67	0.356	- 0.456	45.2
			H-50	2.60	0.359	- 0.504	49.0
- 1.0	1.0	10.0	C	8.73×10^8	8.10×10^{-12}	- 0.322	50.0
			P	2.61×10^9	3.22×10^{-12}	0.297	Pump
			H-10	1.32×10^9	7.22×10^{-12}	0.131	Damper
			H-50	9.83×10^8	8.53×10^{-12}	- 0.160	43.6

† CODE: C = constant velocity
P = parabolic profile
H - M = Hartmann profile, M = M

Table 4. Comparison of slit-channel theory and numerical results, $|\gamma\alpha| = 1.4$, $\kappa = 0$.

\bar{s}	R_M	α	Profile	$\frac{FF^*}{\tilde{y}=1}$	$\frac{A'_{fo}}{A'^*_{fo}}$	P_s/P_o	$e_g\%$
- 1.0	200	0.1	S. C. Theory	1.00	0.250	- 0.0500	50.0
			C	1.68	0.239	- 0.0543	50.0
			P	2.78	0.244	- 0.0471	32.8
			H-10	1.99	0.242	- 0.0527	45.2
			H-50	1.74	0.239	- 0.0539	49.0

For large $\gamma\alpha$ the changes become more dramatic because the fields decrease rapidly away from the channel walls, as shown in section 3.7, and the boundary layer controls the behavior of the machine. If the field has decayed appreciably before the fluid velocity becomes greater than v_g , the machine will operate as a pump even though the average slip is negative because the interaction of the central core is negligible. When both pump and generator effects are appreciable the machine may be a damper, but only when the fluid velocity rises quickly to the negative-slip region does the machine operate as a generator. The operating regime switches from pump to damper to generator as the profile becomes flatter and as the average slip becomes more negative because the size of the positive-slip boundary region decreases. The actual velocity profile will not be Hartmann for this case, as discussed in sections 4.5 and 4.6, because of the large field variations.

The numerical results presented in Tables 3 through 6 illustrate these points. For a fixed α , R_M , and profile as \bar{s} becomes more negative the machine is successively a pump, damper, and generator. The transition occurs at smaller $|\bar{s}|$ as the profile becomes flatter, and at larger $|\bar{s}|$ as α is increased. The power densities for all large $\gamma\alpha$ cases are small and the profile effects are large, so that this region is to be avoided for energy conversion.

The two cases shown for $\bar{s} = -10$ are unusual because the power density and efficiency are higher for the nonconstant profiles. This occurs when the field variation and slip are both large. Then, since the fluid has not reached its maximum velocity before the field becomes negligible, the average slip seen by the field is less than the average for the fluid. This may result in a higher efficiency, but it is not of practical significance because P_s/P_o and e_g are both low.

The numerical integration procedure for the electromagnetic fields and powers works well, as shown by these results. It is used again in section 4.6, where the iterative procedure gives the fields, powers, and velocity profiles.

Table 5. Numerical integration results for the electromagnetic fields and powers, varying \bar{s} , $\alpha = 1$, $\kappa = 0$.

\bar{s}	R_M	α	Profile	$\frac{FF^*}{y=1}$	$\frac{A'_{fo}}{A^*_{fo}}$	P_s/P_o	$e_g\%$
- 0.04	25	1.0	C	2.58	0.359	- 0.518	96.2
			P	22.7	0.00399	0.247	Pump
			H-10	5.12	0.0815	0.325	Damper
			H-50	2.86	0.328	- 0.273	52.5
			H-80	2.74	0.347	- 0.374	68.7
- 0.1	25	1.0	C	3.67	0.0944	- 0.389	90.9
			P	31.9	0.00307	0.253	Pump
			H-10	8.28	0.0428	0.201	Damper
			H-50	4.32	0.0930	- 0.291	68.6
			H-80	4.06	0.0945	- 0.334	77.3
- 0.4	25	1.0	C	27.3	0.00359	- 0.206	71.4
			P	125	0.00109	0.264	Pump
			H-10	52.0	0.00401	- 0.0205	8.58
			H-50	31.7	0.00383	- 0.187	63.9
			H-80	30.0	0.00375	- 0.195	66.8
- 1.0	25	1.0	C	340	1.18×10^{-4}	- 0.139	50.0
			P	991	1.73×10^{-4}	0.176	Damper
			H-10	574	1.72×10^{-4}	- 0.0974	35.5
			H-50	389	1.30×10^{-4}	- 0.134	48.6
			H-80	370	1.25×10^{-4}	- 0.136	49.1
- 10	25	1.0	C	1.34×10^9	2.98×10^{-12}	- 0.0446	9.09
			P	1.97×10^9	1.66×10^{-11}	- 0.0669	20.2
			H-10	2.15×10^9	6.01×10^{-12}	- 0.0563	15.0
			H-50	1.65×10^9	3.66×10^{-12}	- 0.0464	10.7
			H-80	1.55×10^9	3.40×10^{-12}	- 0.0454	10.1

4.5 VELOCITY PROFILE FOR A KNOWN PRESSURE GRADIENT

Equation 128 is solved for the fluid velocity profile when the vector potential is specified. The profile obtained is the small sR_M solution if the field with no fluid present is used, corresponding to the case when the field is not appreciably affected by the fluid. More important, this serves as the second step in an iterative procedure to obtain the electromagnetic field and velocity profile for arbitrary parameters. For small $\gamma\alpha$ the solution will be close to the Hartmann profile, while for large $\gamma\alpha$ the field does not penetrate into the fluid, causing unusual profiles.

Table 6. Numerical integration results for the electromagnetic fields and powers, varying, $\bar{s} \alpha = 3$, $\kappa = 0$.

\bar{s}	R_M	α	Profile	$\underline{FF}^* _{\tilde{y}=1}$	$\underline{A}_{fo}' \underline{A}_{fo}'^*$	P_s/P_o	$e_g\%$
- 0.04	25	3	C	182	4.30×10^{-4}	- 0.322	96.2
			P	1.77×10^5	2.67×10^{-8}	0.149	Pump
			H-10	2.26×10^3	3.44×10^{-6}	0.227	Pump
			H-50	311	1.89×10^{-4}	0.397	Pump
			H-80	253	3.14×10^{-4}	0.239	Damper
- 0.1	25	3	C	869	4.76×10^{-5}	- 0.342	90.9
			P	3.33×10^5	1.42×10^{-8}	0.149	Pump
			H-10	7.93×10^3	1.14×10^{-6}	0.245	Pump
			H-50	1.50×10^3	3.74×10^{-5}	0.191	Damper
			H-80	1.23×10^3	4.81×10^{-5}	- 0.0319	11.4
- 0.4	25	3	C	3.33×10^5	3.32×10^{-8}	- 0.212	71.4
			P	7.36×10^6	6.46×10^{-10}	0.157	Pump
			H-10	1.23×10^6	1.32×10^{-8}	0.296	Pump
			H-50	5.03×10^5	4.41×10^{-8}	- 0.117	40.0
			H-80	4.36×10^5	4.08×10^{-8}	- 0.170	55.2
- 1.0	25	3	C	6.26×10^8	7.09×10^{-12}	- 0.139	50.0
			P	2.01×10^9	3.00×10^{-12}	0.191	Pump
			H-10	1.49×10^9	1.50×10^{-11}	0.182	Damper
			H-50	8.94×10^8	1.00×10^{-11}	- 0.122	44.0
			H-80	7.97×10^8	8.88×10^{-12}	- 0.131	47.0
- 10.0	25	3	C	3.89×10^{28}	1.14×10^{-32}	- 0.0446	9.09
			P	1.12×10^{28}	9.86×10^{-31}	- 0.0239	8.39
			H-10	5.31×10^{28}	6.14×10^{-32}	- 0.0693	21.2
			H-50	5.72×10^{28}	1.97×10^{-32}	- 0.0530	13.6
			H-80	5.30×10^{28}	1.67×10^{-32}	- 0.0496	12.1

The solution of the nonhomogeneous Eq. 128 is more complicated than the solution of the homogeneous Eq. 127. Before there was only a homogeneous solution for specified initial conditions, which was scaled to match the boundary conditions. Now there is a homogeneous solution and one or two particular solutions, depending on the approach used. Initial conditions are specified, and then a linear combination of the solutions is used to match the boundary conditions. This is harder because of the additional numerical solutions, and the linear combination at the channel wall involves the small difference between large numbers, limiting both the accuracy and the range over which the procedure will work.

The pressure gradient applied to the machine, p_o , is not an independent constant. The average fluid slip \bar{s} must be the same as is used in calculating the electromagnetic field, and p_o is adjusted to satisfy this condition. There are two constants of the homogeneous solution plus p_o to be determined, and two boundary conditions plus the average slip to be satisfied. The external fluid source is assumed to supply the necessary pressure across the machine.

Several approaches to solving Eq. 128 were tested. The equation can be rewritten as

$$\frac{d^2 \left(\frac{v}{v_s} \right)}{dy^2} = \frac{a^2 p_o}{\eta v_s} - M^2 s, \quad (154)$$

where v/v_s is the normalized velocity based on v_s rather than \bar{v} , and $s(\tilde{y})$ is the local slip. If $s(\tilde{y})$ is replaced by \bar{s} , an approximate analytical solution can be obtained for $v(\tilde{y})$ by using the constant-velocity field for M^2 . This is the simplest approach, but it is unsatisfactory because the electromagnetic pressure gradient does not reverse sign for $v(\tilde{y}) < v_s$, or the pump region never exists. This leads to unreasonable profiles, with the velocity reversing direction near the walls. A typical solution for large γa is shown in Fig. 31 along with a later solution. This is not valid even in the slit-channel limit; it gives the wrong profile – parabolic instead of Hartmann – because the right-hand side of Eq. 154 becomes a constant.

To solve directly for the velocity requires two particular solutions because of the two driving terms. Converting Eq. 128 into an equation for $s(\tilde{y})$ gives

$$\frac{d^2 s}{d\tilde{y}^2} - M^2 s = - \frac{a^2 p_o}{\eta v_s}. \quad (155)$$

The homogeneous solutions for s and u are the same, except for the constants, but solving for s requires only one particular solution.

The numerical techniques used to solve Eq. 155 are the same as before. The homogeneous solution s_h is found by using the initial value one, with zero slope from symmetry. The initial values for the particular solution are that both s_p and its derivative are zero at the center, and

$$P_1 = \frac{a^2 p_o}{\eta v_s} \quad (156)$$

is taken as unity for the solution. Since P_1 will be scaled, $s_p(0)$ must be zero to avoid difficulty. The solution is

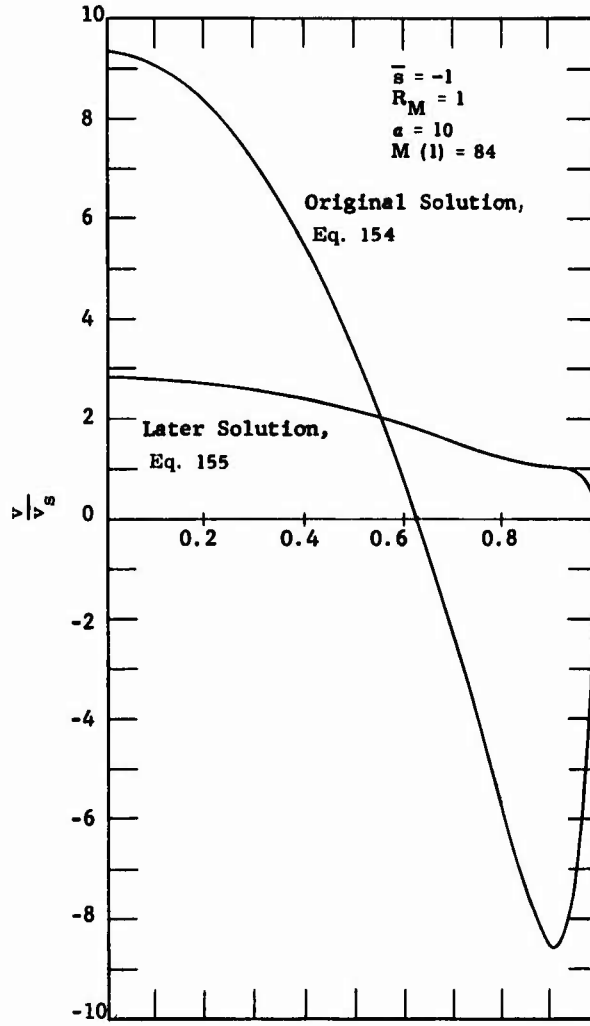


Fig. 31. Comparison of velocity-profile solutions by two methods.

$$s(\tilde{y}) = P_1 (A s_h + s_p). \quad (157)$$

The conditions still to be satisfied are that the average slip is \bar{s} and that the slip at the wall is unity. These give

$$A = \frac{(\bar{s}_p - \bar{s} s_p(1))}{(\bar{s} s_h(1) - \bar{s}_h)} \quad (158)$$

and

$$P_1 = \frac{\bar{s}}{(A \bar{s}_h + \bar{s}_p)}. \quad (159)$$

Difficulty occurs in evaluating the constants because the small difference between large numbers is required, since both the particular and homogeneous solutions are growing exponentials. The addition of double precision, allowing the computer to carry

16 figures of accuracy, extends the range over which the solution will work but does not solve the basic problem. Different equations for the constants were tested with no improvement. The maximum Hartmann number at the wall for which the program works depends on the machine parameters. For $\bar{s} = -1$ and $R_M = 1$, the largest values of $M(1)$ tested successfully were 22.4 for $\alpha = 0.1$, 30.4 for $\alpha = 1$, and 266 for $\alpha = 10$. The marked variation occurs because for large α , M drops off rapidly into the fluid, so that the homogeneous and particular solutions at the wall are much smaller for the same $M(1)$. The program normally fails if the wall values of s_h and s_p are greater than $\sim 10^{15}$, but this upper limit is adequate to show the important effects.

The difficulty with the previous solution is the exponential-like behavior. Defining a new variable

$$g(\tilde{y}) = e^{-M(1)\tilde{y}} s(\tilde{y}) \quad (160)$$

removes the growing exponential. The new equation is

$$\frac{d^2 g}{d\tilde{y}^2} + 2M(1) \frac{dg}{d\tilde{y}} + (M(1)^2 - M^2) g = P_1 e^{-M(1)\tilde{y}}, \quad (161)$$

where $g(\tilde{y})$ is roughly a decaying exponential because M decreases toward the center of the channel. The numerical method used in the other cases, method four, is unstable under these conditions, and method five must be substituted, as discussed in Appendix E. This change of variables does not solve the basic problem, and the results are worse than for the previous solution.

The Hartmann profile is obtained for small $\gamma\alpha$, as predicted in section 4.3, since the field does not vary appreciably across the channel. All of the $\alpha = 0.1$ cases tested agreed with the Hartmann profile based on $M(0)$.

For $\alpha = 1$ the profile shape is changed from Hartmann, as shown in Fig. 32. For this case M^2 varies by a factor of three from the center to the edge of the channel. The velocity is plotted as v/v_s because $(v/v_s) = 1$ is where the force reverses direction. The quantity specified in the numerical computation is the normalized exciting current squared or force multiplier,

$$FOR = \frac{\mu_f (NI)^2 a}{2\eta v_s}, \quad (162)$$

which is dimensionally $M^2/\alpha R_M$. Then $M(1)$ is determined from the boundary conditions and the fluid properties.

For large $\gamma\alpha$ the field does not penetrate into the fluid. The flow consists of two regions: a central core where the electromagnetic force is negligible and the profile is parabolic, and a region near the wall where the profile is Hartmann-like, with a sharp rise from zero velocity to synchronous velocity. This is shown by the iterative-solution profiles of section 4.6, which differ little from the profiles obtained here.

Curves for $\alpha = 10$ and $R_M = 1$ are shown in Figs. 37 and 38 for two different values of M^2 at the wall. Both exhibit the same shape, with a much sharper rise for the higher- M case. Comparison with the electromagnetic pressure gradient (Fig. 23) shows that M^2 is down by one order of magnitude at $\tilde{y} = 0.9$, after which the electromagnetic effects become negligible, which agrees with the figures. Each graph has curves for three values of \bar{s} , all with the same exciting current. The wall shapes are practically identical, and only the central region is different to satisfy the average-velocity condition.

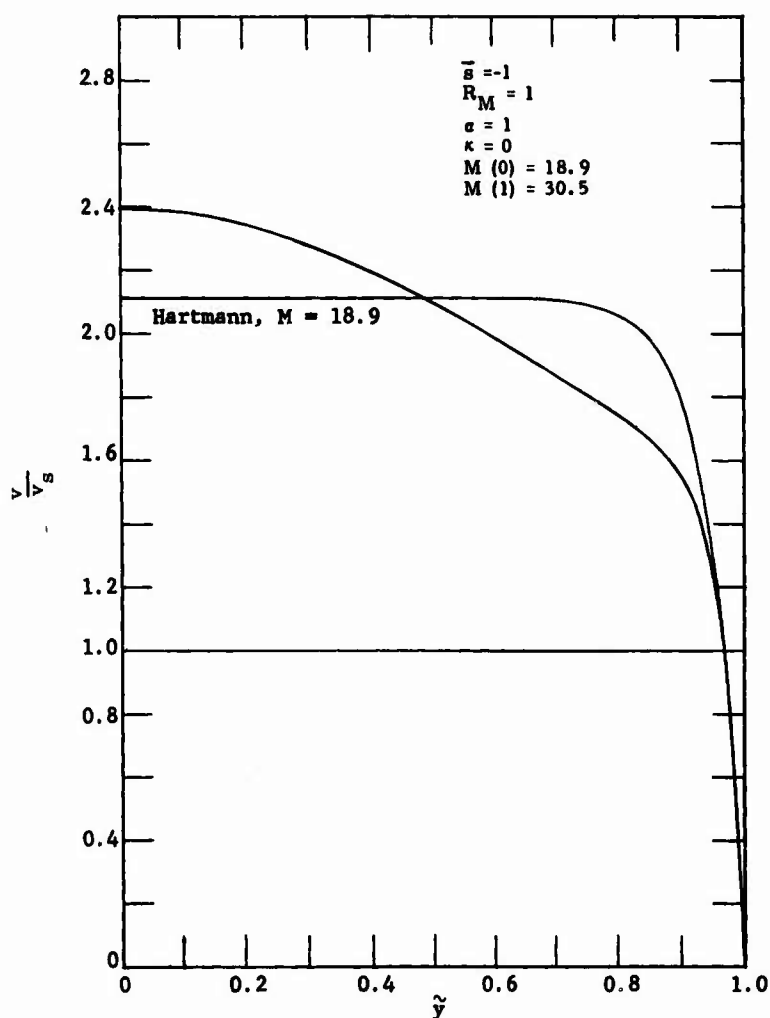


Fig. 32. Comparison of velocity-profile solution with Hartmann profile, $\alpha = 1$.

Three curves for pump operation are plotted in Fig. 33. Curves 1 and 2 show the effect of increasing $M(1)$ for $\alpha = 10$, while curve 3 is for $\alpha = 1$. For large α the velocity virtually locks into synchronous speed near the wall, as occurred for \bar{s} negative.

The shape for the 5 to 10% of the channel half-width near the wall depends primarily on α and $M(1)$, and is almost independent of \bar{s} . This suggests that the iterative solution of section 4.6 will give powers with little dependence on \bar{s} for large $\gamma\alpha$, since only the wall region enters into the energy transfer.

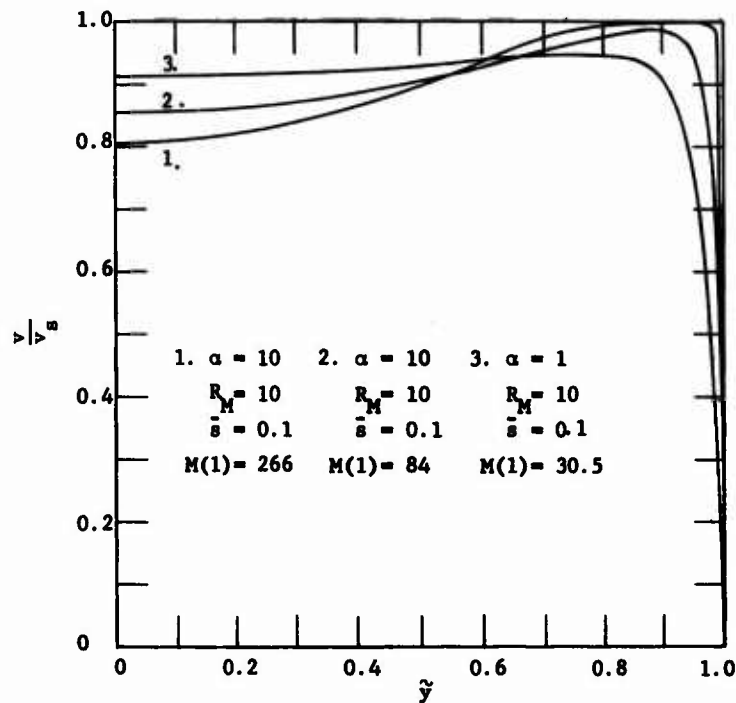


Fig. 33. Pump velocity profiles.

The velocity profiles presented illustrate the important behavior patterns despite the limitations imposed by the numerical procedure. Additional velocity profiles are shown in section 4.6.

4.6 AN ITERATIVE SOLUTION

The techniques developed for solving Eqs. 127 and 128 are combined to obtain an exact solution for laminar flow by iterating. The electromagnetic field for a constant fluid velocity is used as the starting point, and Eqs. 128 and 127 are solved repetitively for the new velocity and field in that order, as in sections 4.5 and 4.4, until the solution converges to the desired accuracy. The convergence is good for R_M small, but becomes worse as R_M increases because the fluid profile has more effect on the field.

All of the $\alpha = 0.1$ cases tested with the iterative procedure checked with the slit-channel results of section 4.3, except for $sR_M = -250$, where M^2 varied by a factor of three across the channel and the profile was no longer Hartmann. The small $\gamma\alpha$ case is excluded from further consideration here as it is better treated by the methods discussed in section 4.3.

Some of the results for large γa are given in Figs. 34 through 38 and in Table 7. The velocity profiles are similar to those of section 4.5, but the powers are different from those of section 4.4, because of the large profile changes. The initial and final iterations for the velocity profile are compared in Fig. 34 for one set of parameters. The difference is small, so that the profiles of section 4.5 are approximately correct, but it may increase for larger R_M . The number of iterations required for convergence to five figures is given in Table 7, where $>$ means that the result is close, but more than the number tried were required. The number increases with increasing \bar{s} and R_M .

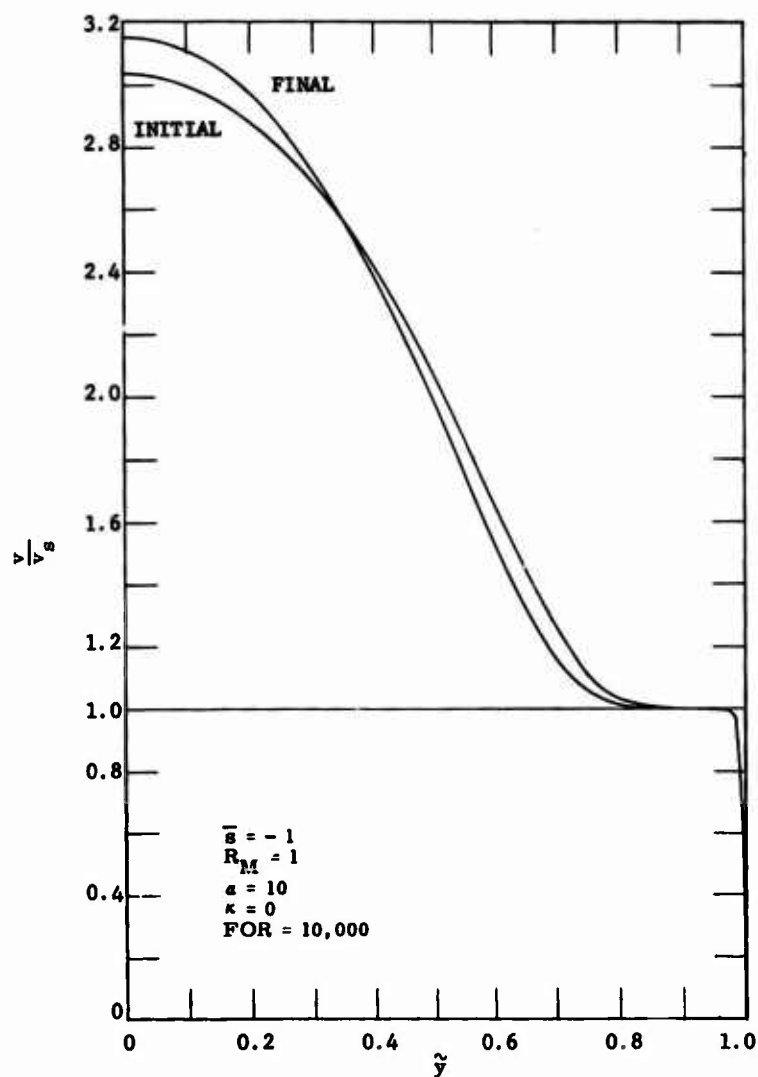


Fig. 34. Comparison of initial and final iterative solutions.

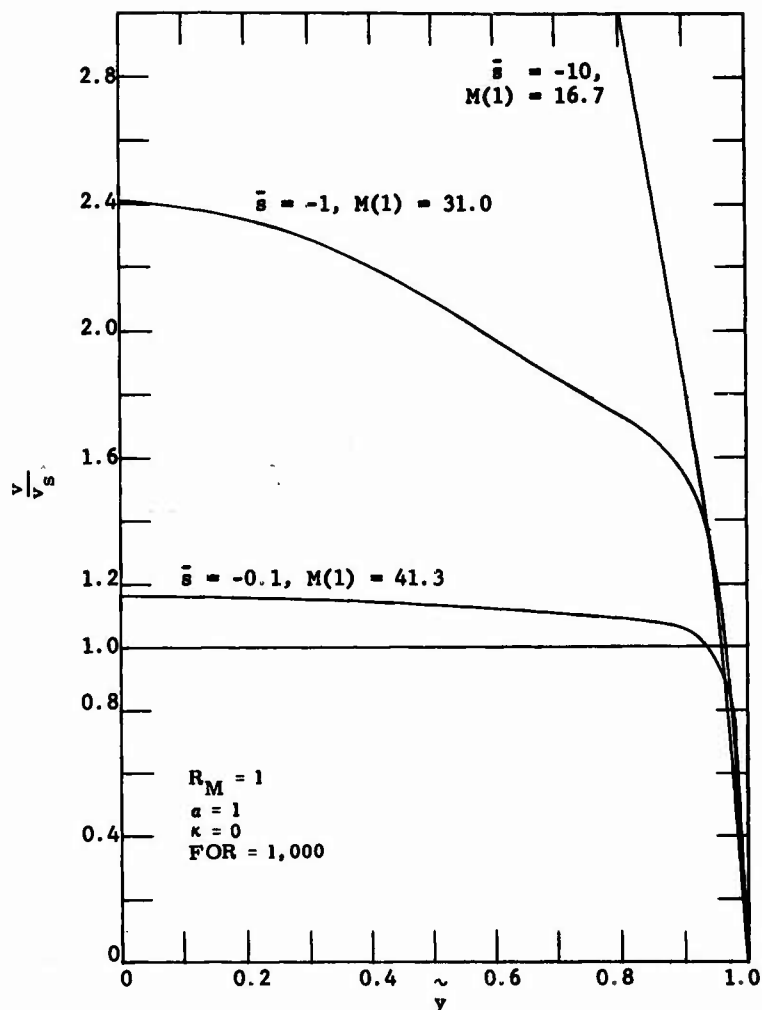


Fig. 35. Iterative solution for velocity, $\alpha = 1$,
 $R_M = 1$, FOR = 1000.

The velocity profiles for $\alpha = 1$, $R_M = 1$ and 10, are plotted in Figs. 35 and 36 for $\bar{s} = -0.1$, -1 , and -10 . The $R_M = 1$, $\bar{s} = -1$ curve is almost identical with the initial solution (Fig. 32) except for a slight dip around $\tilde{y} = 0.6$. As $\gamma\alpha$ increases this dip becomes more pronounced, as is shown by the other figures. The two $\bar{s} = -0.1$ curves look similar, but are quite different near the walls. The power density and efficiency for $\bar{s} = -10$ are still greater than for a constant fluid velocity, as occurred in section 4.4.

The profiles for $\alpha = 10$ and $R_M = 1$, Figs. 37 and 38, illustrate the effect of increasing the exciting current. Both sets of curves show the strong field influence at the wall, but the electromagnetic dominance is more pronounced for the larger excitation and extends farther into the fluid. None of the tested $\alpha = 10$ cases will operate as a generator, since the pumping of the boundary layer dominates, as shown in Table 7.

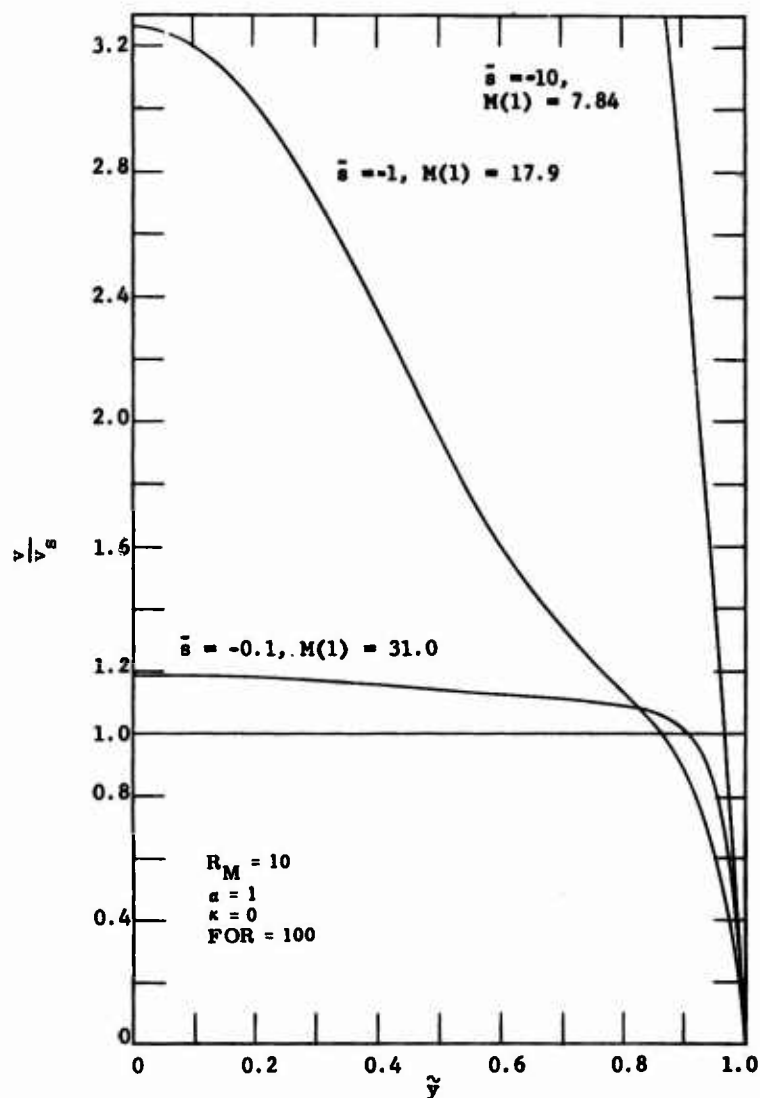


Fig. 36. Iterative solution for velocity, $\alpha = 1$,
 $R_M = 10$, $FOR = 100$.

This concludes the laminar-flow solution for the induction machine. The exact solution has been obtained for several sets of parameters, and can be extended to others if desired. One important result is to eliminate the large $\gamma\alpha$ machine from further consideration. Not only is the power density low, as shown in Section III, but it will not operate as a generator. Odd excitation is also eliminated since $\gamma\alpha \gg 1$ is the only regime where it appeared attractive. The slit-channel results will be used in Section VII to obtain predicted performance characteristics.

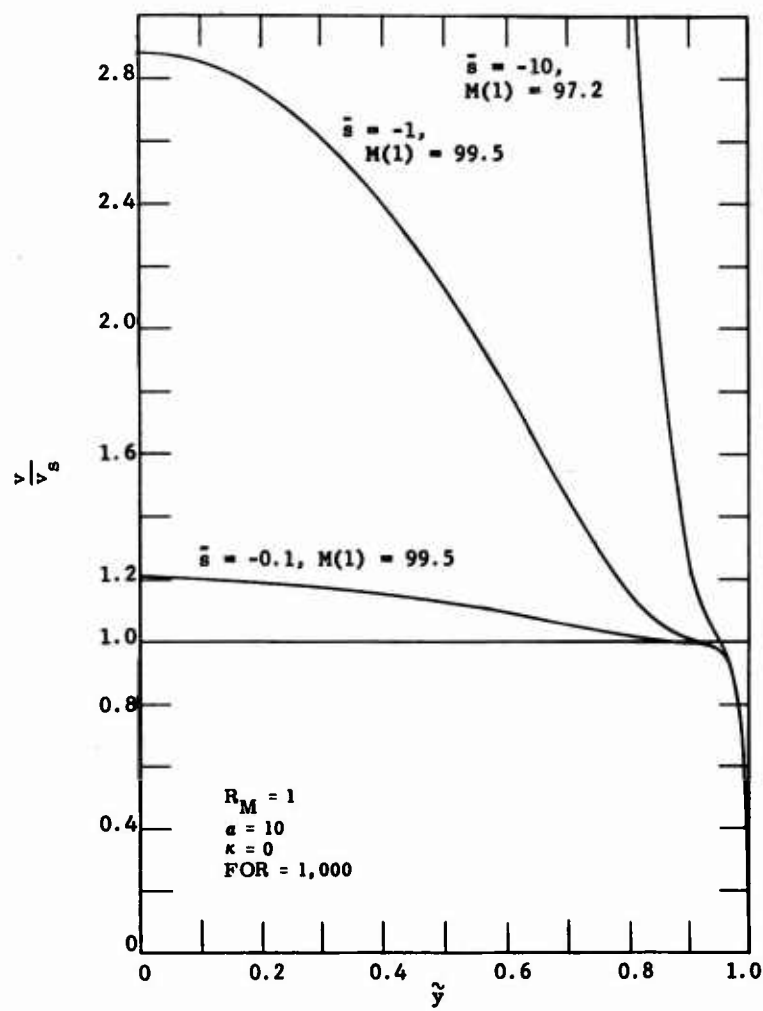


Fig. 37. Iterative solution for velocity, $\alpha = 10$, $R_M = 1$, $FOR = 1000$.

Table 7. Iterative solution results, $\kappa = 0$.

Reference	\bar{s}	R_M	α	FOR	$M(1)$	P_s/P_o	$e_g\%$	Required Number of Iterations
Fig. 35	- 0.1	1	1	1000	41.3	- 0.0753	69.9	2
	- 1				31.0	- 0.456	47.1	4
	- 10				16.7	- 0.168	10.3	> 5
Fig. 36	- 0.1	10	"	100	31.0	- 0.287	57.3	> 3
	- 1				17.9	- 0.0388	13.8	> 5
	- 10				7.84	- 0.0957	17.8	> 5

Table 7. Iterative solution results, $\kappa = 0$ (Cont.).

Reference	\bar{s}	R_M	α	FOR	M(1)	P_s/P_o	$e_g\%$	Required Number of Iterations
Fig. 37	- 0.1	1	10	1000	99.5	0.0937	Pump	2
	- 1				99.5	0.0885	Pump	5
	- 10				97.2	0.0443	Damper	> 6
Fig. 38	- 0.1	1	"	10000	316	0.0310	Pump	3
	- 1				316	0.0302	Pump	5
	- 10				315	0.0238	Damper	> 5

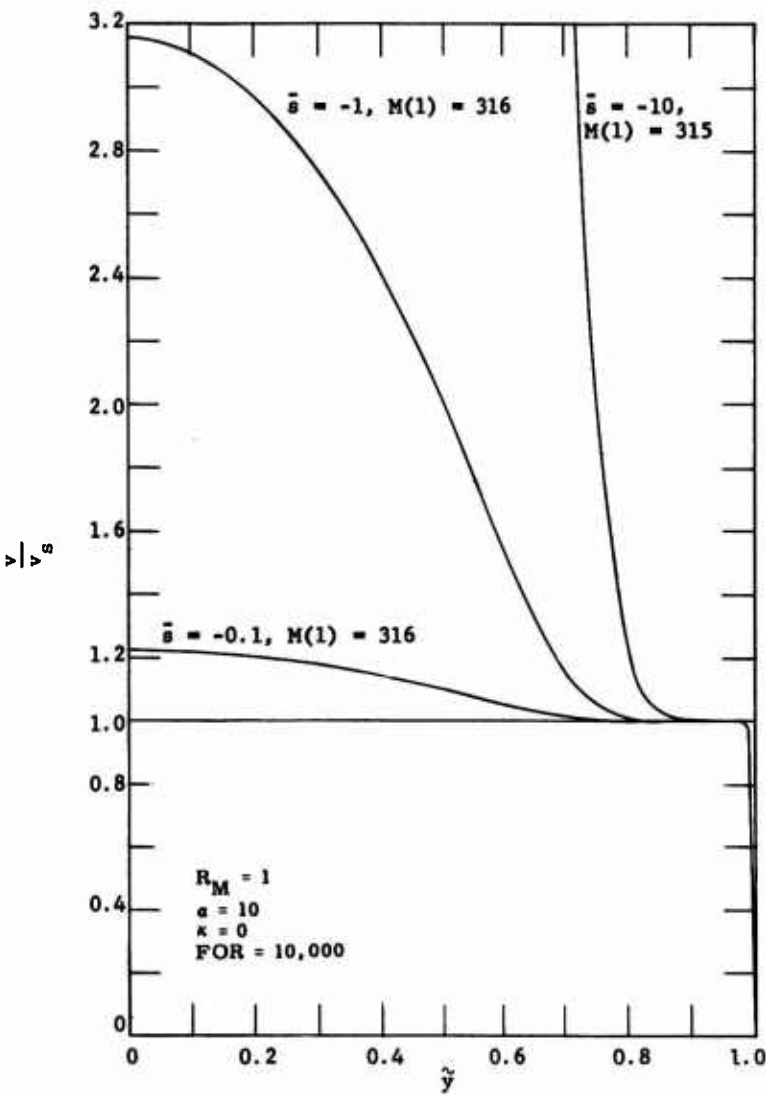


Fig. 38. Iterative solution for velocity, $\alpha = 10$, $R_M = 1$, $FOR = 10000$.

V. TURBULENT FLOW

The flow in a practical MHD induction machine will probably be turbulent, because of the large velocities and Reynolds numbers R_e required to obtain a reasonable power density. The laminar-flow analysis of Section IV is important because turbulent flow is not susceptible to the same kind of analysis; solutions have not been obtained even for the simplest OHD (ordinary hydrodynamic) channel flows. Turbulent OHD flows are discussed in section 5.1, and the techniques of Section IV are used to examine the behavior of the induction machine in the limit of small electromagnetic forces, when the velocity profile is that of OHD turbulent flow. The available information on turbulent MHD flows with a DC transverse magnetic field is summarized in section 5.2. The effect of a traveling electromagnetic field on turbulent flow is considered briefly in section 5.3, but is hampered by the lack of experimental information. Finally, boundary-layer theory is applied in sections 5.4 and 5.5 to laminar and turbulent flows. This has been established as a valuable technique for handling OHD flows, and is shown to be useful for induction-coupled MHD flows.

5.1 EXPERIMENTAL TURBULENT HYDRODYNAMIC VELOCITY PROFILES

In turbulent flow the simple picture of laminar flow or flow in layers is no longer valid. Instead there is violent eddying and momentum transfer in the direction perpendicular to the average flow, and this has the effect of **averaging the velocities or reducing the velocity gradient over the central part of the flow**. Near the walls there are sharp gradients as the wall velocity is zero. This flow pattern causes a marked increase in the viscous loss for the same flow rate over that with laminar flow conditions if laminar flow could be attained.

Although OHD turbulent channel flow has not yielded to analysis, sufficient experimental data are available to obtain a good picture of the structure of the flow and the velocity profile. A description, which is due to Harris,⁴⁷ follows.

There is a central core occupying perhaps 90 per cent of the channel volume in which the mean velocity varies slowly with position, the velocity fluctuations are only a few per cent of the mean velocity, and dissipation effects are practically negligible. There is a very thin laminar region near the wall [known as the laminar sub-layer] where dissipation effects are controlling; the mean velocity increases linearly with distance from the wall, and fluctuations are small or nonexistent. This region usually occupies less than 1 per cent of the channel volume. In between is the transition region, an area of great activity where the velocity fluctuations are comparable to the mean velocities and where most of the power driving the flow is dissipated.

The shape of the OHD turbulent profile, Fig. 39, is similar to the Hartmann profile except for the transition region. Three equations that fit the experimental profile data are presented and compared, and then tested by using the techniques of Section IV.

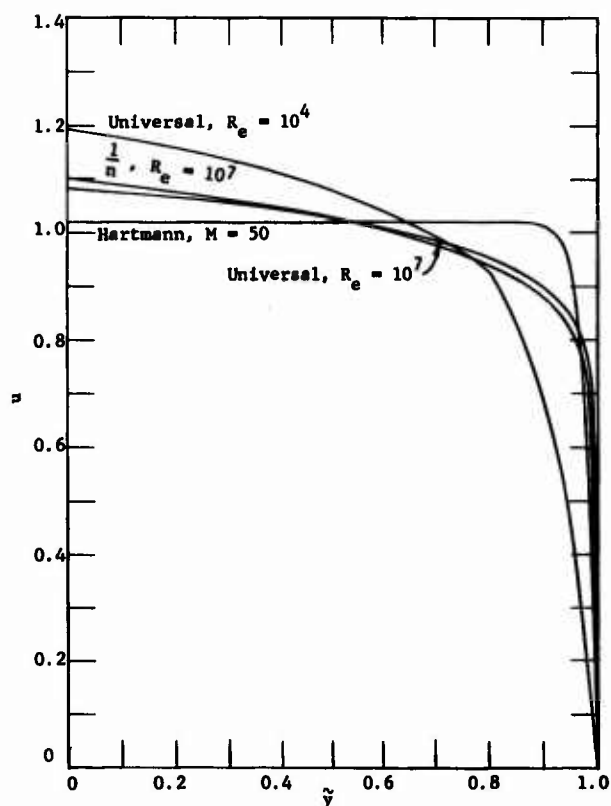


Fig. 39. OHD turbulent velocity profiles.

The transition between OHD laminar and turbulent flow is determined by the Reynolds number

$$R_e = \frac{\rho \bar{v} D_h}{\eta}, \quad (163)$$

where

$$D_h = \frac{4 \text{ (cross-section area of flow)}}{\text{(wetted perimeter)}} \quad (164)$$

is the hydraulic diameter for a channel of arbitrary cross section. For flow between two parallel plates of infinite width spaced a distance $2a$ apart, $D_h = 4a$. The flow is turbulent for R_e greater than approximately 2000.

The simplest velocity profile with a reasonable fit to the experimental data is the $(1/n)^{\text{th}}$ -power law.⁴⁸

$$u(\tilde{y}) = \left(\frac{n+1}{n} \right) (1 - \tilde{y})^{\frac{1}{n}}, \quad (165)$$

retaining the normalized notation of Section IV where n , a function of R_e , is often taken to be 7, although it varies from 6 to 10 as shown in Table 8. The numbers are approximate because the values of R_e considered here do not correspond exactly to the experimental measurements. This profile is not valid near the center of the channel because the slope is not zero, and at the edge the slope becomes infinite.

A better profile, obtained by fitting a different curve to each of the three regions mentioned earlier, is the "universal velocity distribution" law. The equations are⁴⁹

$$v = \xi \qquad \qquad \qquad \xi < 5 \qquad \qquad \qquad (166a)$$

$$v = 5.0 \ln(\xi) - 3.05 \qquad \qquad \qquad 5 < \xi < 30.569 \qquad \qquad \qquad (166b)$$

$$v = 2.5 \ln(\xi) + 5.5 \qquad \qquad \qquad 30.569 < \xi \qquad \qquad \qquad (166c)$$

for the laminar sublayer, transition region, and turbulent core, respectively, where

$$\xi = \frac{R_e}{8} \sqrt{\frac{f}{2}} (1-\tilde{y}) \qquad \qquad \qquad (167)$$

depends on the distance from the channel wall, $(R_e/8)(\sqrt{f/2})$ is the "friction Reynolds number" based on wall shear stress, and \ln denotes the natural logarithm. The velocity has to be normalized by numerically calculating \bar{v} and dividing Eq. 166 by \bar{v} . The friction factor f , defined in Eq. D.18, is found as a function of R_e from the experimental data of Moody.⁵⁰ Several typical values are given in Table 8. The slope at the center of the channel is again not zero.

Table 8. Turbulent velocity profile information.

R_e	n ⁴⁸	f ⁵⁰	$\frac{R_e}{8} \sqrt{\frac{f}{2}}$
10^4	6.8	0.0305	1.5×10^2
10^5	7	0.0178	1.2×10^3
10^6	8.8	0.0117	9.6×10^3
10^7	10	0.0082	8.0×10^4

A third profile is obtained by neglecting the transition region of the previous profile. Only Eqs. 166a and 166c are used, with the intersection of the two curves at $\xi = 11.63$. For the numerical values of interest, large R_e , the difference between the two profiles is negligible because the transition to the turbulent core occurs in less than 1% of the channel half-width for $R_e > 10^6$. Therefore this profile is not considered further.

The normalized velocity profiles for the $(1/n)^{\text{th}}$ -power law and the "universal velocity distribution" law are compared in Fig. 39 for $R_e = 10^7$. The difference is quite small, and is certainly less than the change caused by adding a magnetic field. A better comparison is shown in Schlichting,⁵¹ where both the various approximate equations and the experimental points are plotted on a log scale. Also shown in Fig. 39 is the Hartmann profile for $M = 50$, which is flatter in the center but has a smaller slope at the wall. The fourth curve is the universal profile for $R_e = 10^4$. As R_e is decreased the profile becomes more rounded. The sharp discontinuity in the slope near $\tilde{y} = 0.8$ is due to the transition between the two logarithmic equations.

The velocity profile is not changed significantly from the OHD turbulent profile if the electromagnetic force is small. In this limit, which is not of practical interest except in MHD flowmeters, these known profiles can be used with the methods of section 4.4 to find the electromagnetic fields and powers. The techniques are the same, but care must be used with the turbulent profiles in numerical calculations: 100 points across the channel half-width is not sufficient, 1000 points appears to be a minimum, and more are desirable.

The profile factors and generator efficiency for a slit channel can be evaluated as in section 4.3. The results for e_g are shown in Fig. 40 for the $1/n$ profile and in Table 9 for both profiles for several values of the average slip. Values of e_g for the universal curve are not plotted because of the lack of a general equation. The universal profile is slightly flatter for large R_e and gives a higher efficiency, but the reverse is true for small R_e . The results agree well with the Hartman profile for large M ; the $n = 10$ case is virtually identical to $M = 60$ despite the different shapes.

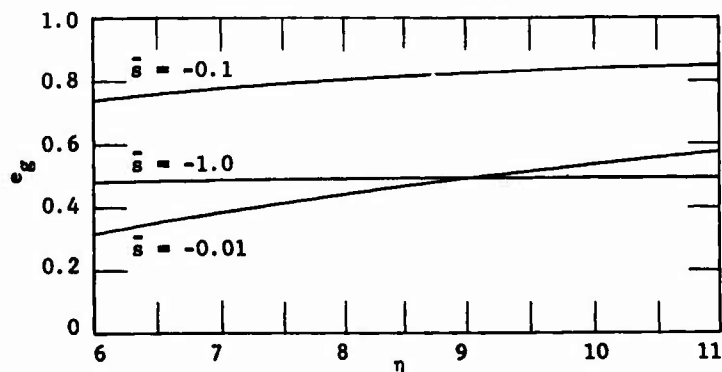


Fig. 40. Slit-channel generator efficiency for $(1/n)^{\text{th}}$ -power law turbulent profile.

Table 9. Slit-channel generator efficiencies.

Universal Velocity Distribution Law					$(1/n)^{\text{th}}$ -Power Law			
$\bar{s} \backslash R_e$	10^4	10^5	10^6	10^7	10^4	10^5	10^6	10^7
-0.01	0.159	0.354	0.500	0.599	0.338	0.380	0.480	0.538
-0.1	0.579	0.760	0.822	0.849	0.751	0.774	0.815	0.833
-1.0	0.453	0.483	0.491	0.494	0.482	0.485	0.490	0.492

5.2 TURBULENCE AND DC MAGNETIC FIELDS

The presence of a transverse DC magnetic field tends to suppress turbulence. There are two possible mechanisms for this: damping of the random eddying motion caused by induced currents and forces, and the change in the velocity profile due to the MHD body force. Murgatroyd⁵² found experimentally that the flow is turbulent for $R_e/M > 900$, which for large M represents a considerable increase in the range of R_e for laminar flow.

The change in the viscous loss with the transition from laminar to turbulent flow is of considerable interest. For OHD flows there is a marked increase. For MHD flows the only experimental measurements available are for the total pressure drop across the channel length, including both viscous and circulating-current losses, with no way to separate them until the velocity profile is measured. The total pressure increases with the transition from laminar to turbulent flow, but it is not possible to determine the ratios of the viscous losses for the MHD laminar, MHD turbulent, and OHD turbulent cases. The small-scale circulating currents induced by turbulence, which do not contribute either to the viscous loss or to the circulating-current loss resulting from the time-average velocity, should also be considered. The present theory includes the circulating current loss in P_r , so that only the viscous and turbulent-current losses are desired.

Harris⁵³ has studied turbulent MHD flow using semiempirical techniques and the experimental results of Hartmann and Lazarus,⁵⁴ and Murgatroyd.⁵² He obtained an equation for the friction factor for the total pressure drop with no external electrical connection to the fluid, given in Eq. D.24. He also derived the theoretical time-average velocity profiles for turbulent flow shown in Fig. 41. The shape is determined by the "friction Reynolds number" and "friction velocity" based on the wall shear stress τ_0 as in OHD flows, and also by M . For small M the profile is the OHD turbulent profile, while for large M it approaches the Hartmann shape, but a much larger M is required for the same degree of flatness. The more rounded profile means increased I^2R losses. As the curves are bounded by the OHD turbulent and Hartmann profiles, they do not add much additional information, and are not considered using the techniques of Section IV. There is some question as to their general validity because they are based on the same

analysis as the friction factor predictions made by Harris, and these do not extrapolate from the earlier data to fit a more recent experiment.⁵⁶ Experimental studies of velocity profiles are needed to check his results.

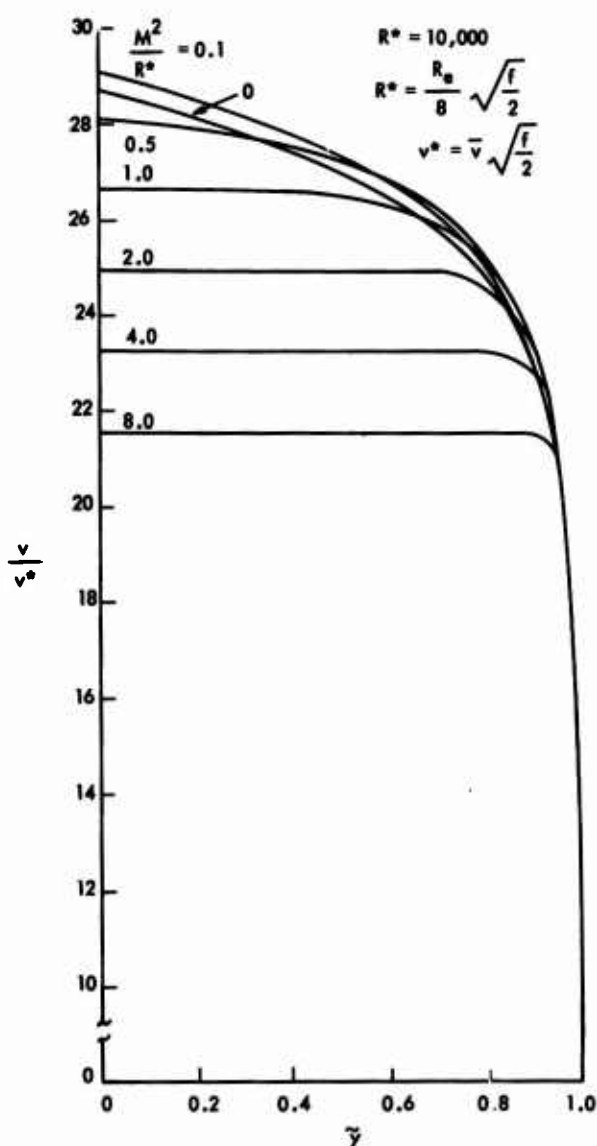


Fig. 41. Theoretical MHD turbulent velocity profiles of Harris.

5.3 TURBULENCE AND TRAVELING ELECTROMAGNETIC FIELDS

The situation is more complex for a traveling electromagnetic field, and there are no experimental results available. The electromagnetic force acting on the fluid changes

both magnitude and direction with time. This should decrease the stability of laminar flow, and possibly increase the turbulent losses.

The effect of the electromagnetic force on the flow is determined first. Taking the curl of Eq. 5g and defining the vorticity

$$\vec{\omega} = \nabla \times \vec{v}, \quad (168)$$

gives

$$\rho \frac{\partial \vec{\omega}}{\partial t} = \rho \nabla \times (\vec{v} \times \vec{\omega}) + \eta \nabla^2 \vec{\omega} + \nabla \times (\vec{J} \times \vec{B}). \quad (169)$$

For comparison purposes consider the case of a DC magnetic field, Hartmann flow. Here \vec{B} is a constant, but \vec{J} is an exponential function of y . The curl of $\vec{J} \times \vec{B}$ is not zero, and this changes the velocity profile. The DC magnetic field stabilizes laminar flow, however, despite the nonzero curl of the electromagnetic force.

It is impossible to find a general expression for $\nabla \times (\vec{J} \times \vec{B})$ for the induction machine because \vec{J} and \vec{B} are both functions of the velocity. Consider only the case of an x-directed velocity depending only on y and a z-directed current, as in Section IV. Care must be used to take the real part before the cross-product is evaluated. Writing the time functions as

$$F(x, y, t) = \frac{1}{2} \left\{ \underline{F}(y) e^{j(\omega t - kx)} + \underline{F}^*(y) e^{-j(\omega t - kx)} \right\} \quad (170)$$

simplifies the calculation. The result is

$$\begin{aligned} \nabla \times (\vec{J} \times \vec{B}) = & \vec{i}_z \frac{j\sigma}{2} (\omega - vk) (\underline{B}_x^* \underline{B}_y - \underline{B}_x \underline{B}_y^*) \\ & + \vec{i}_z \frac{\sigma}{4} \left(\frac{\partial v}{\partial y} \right) \left(\underline{B}_y \underline{B}_y e^{j2(\omega t - kx)} + \underline{B}_y^* \underline{B}_y^* e^{-j2(\omega t - kx)} + 2 \underline{B}_y \underline{B}_y^* \right) \end{aligned} \quad (171)$$

Only for the special case of a constant velocity is this independent of time. Otherwise there is a time dependence that will be particularly large in the transition region near the wall where the turbulence is normally generated. The possibility thus exists for coupling between the traveling field and the generation or turbulent eddies in the fluid. The electromagnetic force should make laminar flow less likely because of the time-dependent curl and the pulsating force. On the other hand, it will also have a stabilizing influence because the small-scale induced currents and forces due to turbulence act to damp out turbulence as in the DC case. The net behavior depends on which mechanism predominates, and this can only be determined by experimental study.

5.4 LAMINAR BOUNDARY-LAYER THEORY

In boundary-layer theory the fluid flow is split into two parts:

1. A region near the wall in which viscosity is important, and where there are large velocity gradients normal to the wall.
2. A region away from the wall where viscous forces are negligible, no large velocity gradients occur, and the flow is essentially potential flow.

A common example is flow over a flat plate of finite length or around an obstacle of dimensions small compared with those of the flow field. The flow can be solved under the assumption of an inviscid fluid and potential flow to determine the gross behavior, and viscosity is then considered only in the thin layer along the body because the fluid velocity is zero at the wall.

In OHD flows the viscous forces in the boundary layer are balanced by inertial forces. The fluid slows down, and the boundary-layer thickness must grow along the surface to satisfy conservation of momentum. For channel flow the boundary layers will grow from the entrance until they meet, after which the viscous force is balanced by the pressure gradient, so that boundary-layer theory is valid only for determining the entry length.

In MHD channel flows electromagnetic terms are added to the force balance, and this allows the thickness of the boundary layer to stabilize at some finite value. If the boundary-layer thickness δ is small compared with the channel half-width a , the channel flow can be represented by a central core where the velocity is constant and the electromagnetic force balances the pressure gradient and a thin boundary layer where viscosity and velocity gradients are important. This description bears a qualitative relation to Hartmann flow, and the analytical results are similar.

Boundary-layer theory is introduced in OHD flows because exact or approximate solutions can be obtained for cases where the complete Navier-Stokes equation cannot be solved. These include flow over a flat plate of finite length and flow around a cylinder. It can be applied to laminar flow directly, and to turbulent flow with the use of experimental measurements. Two approaches are available – a differential form obtained from the Navier-Stokes equation with small terms neglected, and an integral form as used here. The differential form is used for laminar flow to obtain both the velocity profile in the boundary layer and the boundary-layer thickness, but solutions are difficult to obtain even for simple geometries, and only a few solutions are available. The integral form neglects the details of the boundary layer; a velocity profile is assumed and δ is determined as a function of this velocity profile. The results for this approximate method are within a few per cent for OHD laminar flows, as shown by Schlichting.⁵⁷ For turbulent flows insufficient knowledge is available to use the differential form, and the integral form can be solved only with the aid of experimental data. For a thorough discussion of boundary-layer theory applied to OHD flows, see Schlichting.⁵⁸

In the following discussion boundary-layer theory is applied to the MHD induction machine. The integral equation neglecting the entrance region is derived and solved for laminar flow in this section, and for turbulent flow in section 5.5. The advantage of boundary-layer theory is in treating turbulent flows, since the laminar solution can be obtained directly from the equations, but there are difficulties in its use for MHD flows.

The integral form of the force-balance equation for the boundary layer is obtained according to the model of Fig. 42. The x-directed forces acting on the small volume are the wall shear stress τ_o , the pressure gradient, and the electromagnetic force, $J_{fz} B_{fy}$ for the induction machine. Only the constant boundary layer, δ independent of x , is considered, so that there is no net transport of momentum into the volume. Since the fluid velocity in the central region is a constant, v_o , no shear stress acts on the upper surface of the volume. The force equation in the x-direction, taking the limit as $\Delta x \rightarrow 0$, is

$$\tau_o + \int_0^{\delta} \frac{\partial p}{\partial x} dy_1 + \int_0^{\delta} J_{fz} B_{fy} dy_1 = 0 \quad (172)$$

for a unit length in the z-direction and no dependence on z. A new variable y_1 has been defined as zero at the wall for convenience. The force balance equation for the whole channel also required is

$$\tau_o + \int_0^a \frac{\partial p}{\partial x} dy_1 + \int_0^a J_{fz} B_{fy} dy_1 = 0, \quad (173)$$

using symmetry about the center. Cancelling out the part contained in the boundary-layer equation leaves

$$\int_{\delta}^a \frac{\partial p}{\partial x} dy_1 + \int_{\delta}^a J_{fz} B_{fy} dy_1 = 0. \quad (174)$$

This determines the pressure, which is then eliminated from Eq. 172.

The general solution for the induction machine is prohibitive because the electromagnetic field depends on the velocity, requiring a self-consistent solution to the coupled equations, and there is a transverse force so that $\partial p / \partial x$ depends on y_1 . Also, since the electromagnetic force varies across the channel, the velocity should also vary as shown in Section IV, and the model used here of a constant-velocity core is no longer valid. For these reasons attention is restricted to a slit channel, which has already been established as the only case of practical interest.

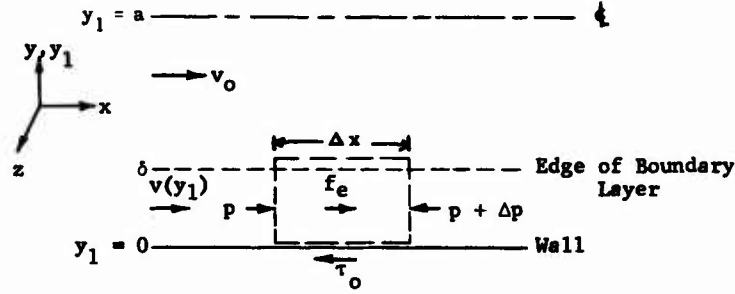


Fig. 42. Model for boundary-layer analysis.

For a slit channel the magnetic field was shown in section 4.3 to be independent of the velocity profile. In terms of the constant vector potential, the time-average pressure gradient is

$$p_0 = \sigma_f k^2 (v_s - v_0) \frac{A_f A_f^*}{2}, \quad (175)$$

from Eq. 174, which does not depend on y_1 . Restricting attention to laminar flow, the wall shear stress is

$$\tau_0 = \eta \left. \frac{dv}{dy_1} \right|_{y_1=0} \quad (176)$$

In terms of the effective Hartmann number for the AC field, Eq. 126, and by using Eqs. 175 and 176, the time average of Eq. 172 can be written as

$$\left. \frac{dv}{dy_1} \right|_{y_1=0} + \frac{M^2}{a^2} \left\{ \int_0^\delta v dy_1 - v_0 \delta \right\} = 0, \quad (177)$$

which determines δ and τ_0 for a specified velocity profile. Although derived here for the induction machine, it is equally valid for the DC machine because of the assumptions made.

The velocity profiles tested in Eq. 177 are the linear, second-order, third-order, etc., profiles, and a sinusoidal profile. The boundary conditions are that the velocity is zero at $y_1 = 0$ and v_0 at $y_1 = \delta$ for all profiles, and that the higher-order profiles have

the proper number of zero derivatives at $y_1 = \delta$. The profile equations in terms of the normalized dimension $\tilde{y}_1 = y_1/\delta$, and the results for the normalized boundary-layer thickness δ/a and the normalized wall shear stress $[\tau_0/(\eta v_0/a)]$, which are proportional to $1/M$ and M respectively, are given in Table 10.

A more convenient parameter than δ is the displacement thickness

$$\delta^* = \int_0^a \left(1 - \frac{v}{v_0}\right) dy_1, \quad (178)$$

which is the distance the channel wall would have to be moved in to maintain the same volume flow rate if the velocity was constant at v_0 . As the velocity profile becomes a better approximation and a smoother transition occurs at $y_1 = \delta$, $\delta \rightarrow \infty$ because the approach is asymptotic. This is not true for δ^* , which has the same proportionality constant as τ_0 for laminar MHD flows, since

$$\tau_0 = \left(\frac{\eta v_0 M^2}{a}\right) \left(\frac{\delta^*}{a}\right) \quad (179)$$

from Eqs. 177 and 178.

The displacement thickness and τ_0 are also given for the Hartmann profile for $M > 4$, but δ is not defined since the velocity approaches v_0 asymptotically. Both δ^* and τ_0 are low for the boundary layer or approximate solutions, and approach the Hartmann solution only for large n . As n becomes infinite the series is the expansion for the Hartmann profile, and the solution is exact. The variations among the boundary-layer solutions and the differences from the exact solution are worse than for the comparable OHD flow over a flat plate, where these amount to only a few per cent.⁵⁷

The entrance problem is also of interest. To carry this through properly the coupled interaction of the field and velocity has to be solved. For a slit channel the field does not depend on the profile, so that the field results of Section VI can be used to solve for the fluid entry length. For this solution the momentum transfer to the boundary layer has to be included, and δ and the electromagnetic force depend on x . Because of the complex field solution this is a difficult problem, and is not considered here.

Moffatt⁵⁹ has treated the entrance to a DC magnetic field with no x -variation. He finds

$$\frac{\delta}{a} = \frac{\sqrt{6}}{M} \left(1 - e^{-\left[\frac{5M^2}{R_e'} \frac{x}{a}\right]}\right)^{1/2} \quad (180)$$

Table 10. δ , δ^* , and τ_o for a laminar boundary layer.

$\frac{v}{v_o}$	$\frac{(\delta/a)}{(1/M)}$	$\frac{(\delta^*/a)}{(1/M)} = \frac{[\tau_o/(\eta v_o/a)]}{M}$
\tilde{y}_1	$\sqrt{2} = 1.414$	$\sqrt{\frac{1}{2}} = 0.707$
$2\tilde{y}_1 - \tilde{y}_1^2$	$\sqrt{6} = 2.449$	$\sqrt{\frac{2}{3}} = 0.816$
$3\tilde{y}_1 - 3\tilde{y}_1^2 + \tilde{y}_1^3$	$\sqrt{12} = 3.464$	$\sqrt{\frac{3}{4}} = 0.866$
$n^{th} \text{ order}^*$	$\sqrt{(n+1)n}$	$\sqrt{\frac{n}{n+1}}$
$\sin\left(\frac{\pi}{2}\tilde{y}_1\right)$	$\sqrt{\frac{\pi^2}{2(\pi-2)}} = 2.085$	$\sqrt{\frac{\pi-2}{2}} = 0.749$
Hartmann, $M > 4$	-	1

$^* \frac{v}{v_o} = n\tilde{y}_1 - \frac{n(n-1)}{2!}\tilde{y}_1^2 + \frac{n(n-1)(n-2)}{3!}\tilde{y}_1^3 - \dots + (-1)^{n-1}\tilde{y}_1^n$

for laminar flow using the second-order velocity profile, where $R'_e = (\rho v_o a / \eta)$ is based on the maximum velocity. Considering the exponent as an entry length, the number of wavelengths required is

$$\frac{l_e}{\lambda} = \frac{R'_e a}{10\pi M^2},$$

(181)

which may be large for reasonable power densities.

The laminar boundary-layer solution does not add to the methods available for treating the induction machine. It differs little from the Hartmann profile and approaches it for better approximations to the velocity profile in the boundary layer. The advantage of boundary-layer theory lies in treating turbulent flow, where other analytical methods are not applicable and experimental measurements are not available.

5.5 TURBULENT BOUNDARY-LAYER THEORY

The extension of boundary-layer theory to turbulent flow should include:

- 1. The use of an MHD turbulent profile in the boundary layer.
- 2. The effect of turbulent flow on the wall shear stress.

3. The additional losses, both viscous and I^2R , due to the turbulence.
4. The effect of the turbulent core on the boundary layer; i.e., the momentum transfer from the core to the boundary layer, if any, and the change in the boundary conditions on the boundary layer due to fluctuations in the core.⁶⁰

In OHD turbulent boundary-layer theory the first three points are satisfied by using available experimental data. The fourth point is not well understood, and is generally neglected. Since suitable experiments for MHD flows are nonexistent, it is not possible to properly extend the MHD theory to cover turbulent flow. Instead, MHD turbulent flow can be treated approximately by using the OHD experimental results for the velocity profile and wall shear stress. The profile shape is wrong, but is not too critical, provided δ^*/a is small. The I^2R turbulent loss, for which no OHD equivalent exists, is not included in this approach.

The $1/7^{\text{th}}$ -power velocity profile and associated wall shear stress,⁶¹

$$\frac{v}{v_o} = \left(\frac{y_1}{\delta} \right)^{1/7} \quad (182)$$

and

$$\tau_o = \rho v_o^2 (0.0225) \left(\frac{\eta}{\rho v_o \delta} \right)^{1/4}, \quad (183)$$

from experimental pipe-flow data are used as in OHD turbulent boundary layers. These are based on v_o and δ instead of \bar{v} and a , as is the custom for pipe flow. This is valid for moderate Reynolds numbers. Better accuracy might be obtained from the "universal velocity distribution" law, Eq. 166, but this is too complicated to use here.⁶²

Rewriting Eq. 177 to include this profile and solving gives

$$\frac{\delta}{a} = \frac{0.254}{M} (R_e^*)^{3/5} \quad (184)$$

$$\tau_o = \left(\frac{\eta v_o}{a} \right) M(0.0317) (R_e^*)^{3/5} \quad (185)$$

and

$$\delta^* = \frac{\delta}{8}, \quad (186)$$

where

$$R_e^* = \frac{\rho v_o}{\eta} \left(\frac{a}{M} \right) \quad (187)$$

is the Reynolds number based roughly on δ and v_0 . To relate R_e^* to R_e (Eq. 163), the ratio of the average to maximum velocities is used. This yields

$$\frac{\bar{v}}{v_0} = 1 - \frac{\delta^*}{a}, \quad (188)$$

so that

$$R_e = R_e^* (4M) \left(1 - \frac{\delta^*}{a}\right), \quad (189)$$

Here R_e , the fundamental parameter, is determined by the flow independently of the actual profile. This theory is invalid if $(\delta^*/a) > 1$ (i.e., the boundary layers meet), and is expected to be inaccurate if δ^*/a approaches 1.

The variation of δ^*/a with R_e and M is shown in Fig. 43. The range of applicability of the theory increases with M since the larger electromagnetic force limits the spread of the boundary layer. The theory becomes invalid where the curves depart from a straight line. They are almost straight up to about $\delta^*/a = 0.1$, after which the curvature increases rapidly. The continuing straight line is drawn lightly for $M = 50$ to show this. The $M = 500$ curve has a similar behavior for larger R_e . The theory is probably invalid for $\delta^*/a > 0.2$, shown dashed in the figure, where the departure becomes appreciable.

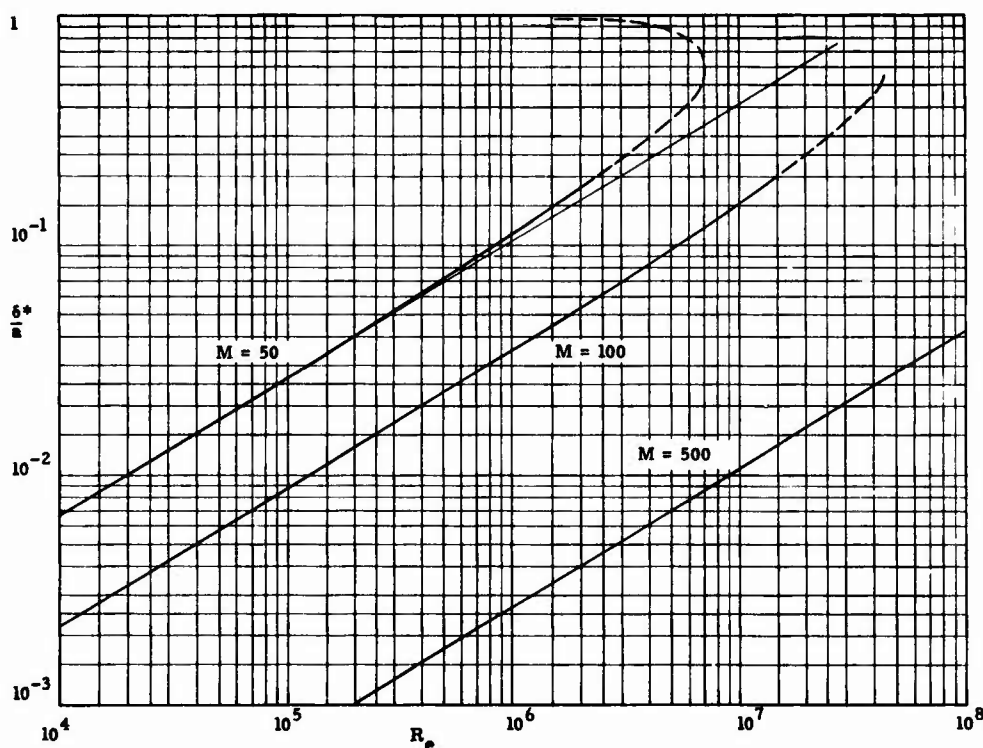


Fig. 43. δ^*/a as a function of R_e and M .

It is convenient for turbulent flows to use the friction factor, defined in Eq. D. 18, to calculate the viscous pressure drop and power loss. For this theory it is

$$f = (0.254) \frac{1}{\left(1 - \frac{\delta^*}{a}\right)^2} \frac{1}{(R_e^*)^{2/5}} \quad (190)$$

This does not include the pressure drop due to the I^2R losses in the fluid.

Graphs of f as a function of R_e for $M = 50, 100$, and 500 are given in Figs. 44 through 46. These differ from the conventional method of plotting f for MHD, but are more convenient for comparison and calculation purposes. Also shown are the friction factors for OHD turbulent flow, Eq. D.23, and for DC MHD laminar and turbulent flows, Eqs. D.21h and D.24. D-C MHD flows are turbulent for $R_e/M > 900$, while induction-driven flows are probably turbulent for a smaller ratio. Equation D.24 for turbulent flow, obtained by Harris from experimental data, is valid for $(M^2/\sqrt{fR_e}) > 0.053$, which leaves only a limited range of applicability for the equation. Because that curve lies so close to the others, its ends are marked by short vertical lines.

The boundary-layer solution lies remarkably close to the MHD turbulent curve obtained by Harris, with a difference that is probably smaller than the experimental error. Both curves lie above the OHD curve (except for large R_e), as expected, but since the experimental curve includes both viscous plus I^2R losses, it should be above the boundary-layer solution.

The boundary-layer solution breaks down, as mentioned already, when δ^*/a becomes close to 1. Arbitrarily picking the limit of validity where the friction-factor curve starts to turn up (shown dashed in the figures), gives roughly the same maximum R_e as determined from the δ^*/a curve. This may be rather liberal, and tighter restrictions are probably required.

The OHD and MHD turbulent friction-factor curves cross for large R_e . It is questionable whether this will actually occur, but further study is required. The boundary-layer solution should probably curve up, as does the f from Eq. D.24.

It is not possible to estimate the accuracy of the MHD turbulent boundary-layer solution without experimental information. It does appear reasonable, however, when compared to the previous results for the friction factor, and will be used in Section VII when applicable because it is the best that is available. There is an urgent need for further experimental measurements on both DC and induction-coupled turbulent MHD flows.

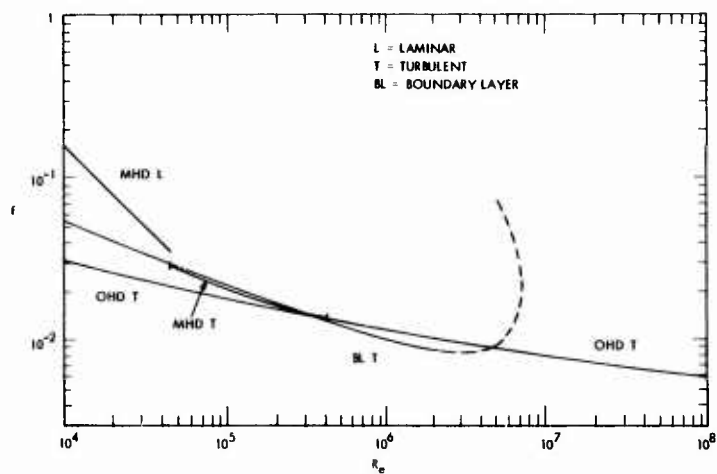


Fig. 44. Friction factors,
 $M = 50$.

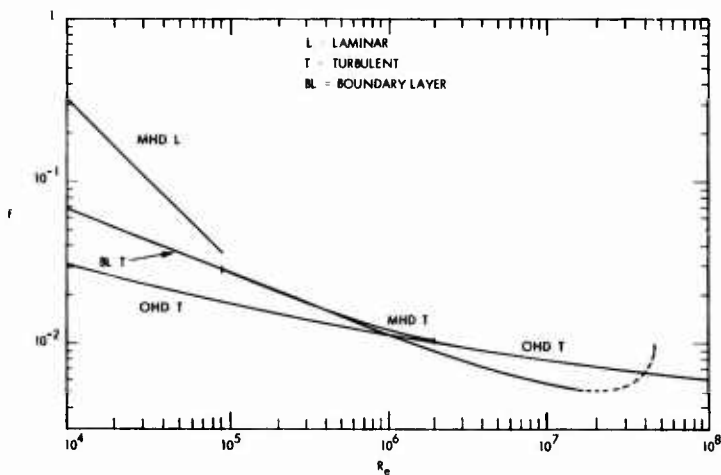


Fig. 45. Friction factors,
 $M = 100$.

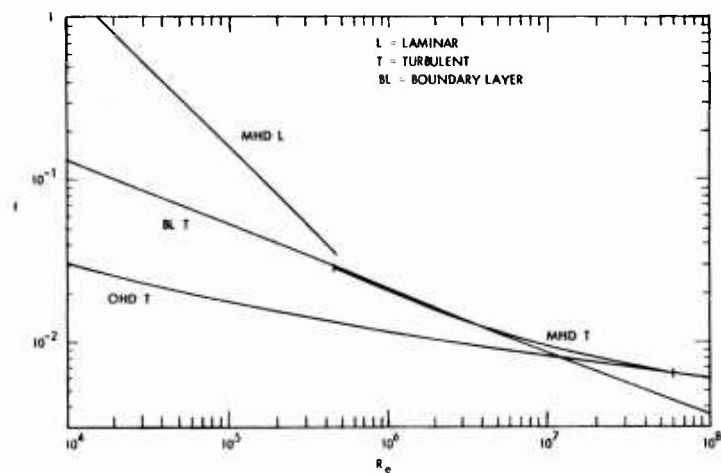


Fig. 46. Friction factors,
 $M = 500$.

VI. THE MACHINE OF FINITE LENGTH

6.1 INTRODUCTION

The regions where the fluid enters and leaves the traveling magnetic field have not been considered in the previous analysis. For a machine that is not long compared to the entry length, severe discrepancies may exist between the predictions based on an infinite-length machine and the actual operating characteristics. We shall now determine the field solution, coil impedance, and powers for two models of the finite-length machine – an ideal iron core of infinite length, and a lossless core of arbitrary permeability and infinite length. The extension of the theory to other models is discussed but not carried out because of computational difficulties.

Before turning to the mathematical details, valuable insight is provided by a qualitative examination of the problem. The vector potential for a moving fluid is determined from Eq. 9, which can be written

$$\frac{\partial \vec{A}}{\partial t} = \frac{1}{\mu\sigma} \nabla^2 \vec{A} + \vec{v} \times \nabla \times \vec{A}. \quad (191)$$

The normalized form of the equation is similar except that $\mu\sigma$ is replaced by R_{MF} , the magnetic Reynolds number based on the fluid rather than the synchronous velocity. The time rate of change of \vec{A} is due to diffusion and convection, represented respectively by the two terms on the right side of Eq. 191. If R_{MF} is small diffusion dominates, there is little change from the stationary fluid solution, and the fringing at the two ends is the same. The solution is symmetric about the ends of the coil if the core extends well past the ends.

With R_{MF} large convection dominates, the fields are different at the two ends, symmetry is destroyed, and a substantial entry length is required for the field to diffuse into the fluid. At the entrance the field is small outside the machine, and there is a considerable change in the field inside from the infinite-length field. Breaking the field into two components, the excitation field which would exist with no ends and the perturbation field owing to the ends, the perturbation field is small before the entrance and comparable to the excitation field just inside the entrance. The decay length* for the perturbation field inside the machine is appreciable, on the order of several wavelengths for practical machine parameters. For the perturbation field and associated powers to be small, a machine must be long compared to the decay length. At the exit the roles are reversed, the perturbation field is small inside the machine, large outside. The excitation field exists only inside the machine.

*The length for the field to attenuate to $1/e$ of its original value.

This gives an idea of the change in the powers due to the finite length. Since it takes a considerable distance for the field to penetrate into the fluid, the primary effect of the entrance is to reduce the power level because the field and power density are small near the entrance. There is some additional electrical loss due to the ends, but for a machine with a substantial central region where the perturbation fields are small, the decrease in the power level may be large, yet with an electrical efficiency that is almost unchanged from the infinite-length machine. (The over-all efficiency is decreased, however, because less output power is obtained for the same viscous and excitation losses.) This is primarily an entrance effect as the perturbation field inside the machine is small at the exit.

6.2 TRANSFORMED POTENTIALS

The model to be analyzed, Fig. 47, differs from that for the infinite-length machine only in the finite length $n\lambda$ of the exciting surface current, where n is in fractions of a wavelength. Consideration of a core of finite length is outside the scope of this investigation for the reasons discussed in section 6.6. The fluid velocity is assumed to be constant and x -directed to uncouple the equations and allow an analytical solution to be obtained. The field solution is independent of the velocity profile for a slit channel, the only case of practical interest, so that the fluid velocity can be determined for this case after the field solution by using the techniques of either Section IV or Section V.

The electromagnetic field equations are unchanged by the finite length. The vector potential is still in the z -direction and independent of z , and must have the same $e^{j\omega t}$ dependence as the exciting current, but now the e^{-jkx} dependence of the excitation is preserved only in the driven part of the solution. Spatial transients, determined by the natural behavior of the system, exist because of the finite length. Writing Eq. 9 for the complex amplitude $\underline{A}_f(x,y)$ gives

$$\nabla^2 \underline{A}_f - jR_M k^2 \underline{A}_f - R_{MF} k \frac{\partial \underline{A}_f}{\partial x} = 0, \quad (192)$$

and a similar equation for $\underline{A}_c(x,y)$. Here

$$R_{MF} = R_M(1 - s) = \frac{\mu_f \sigma_f v}{k}, \quad (193)$$

the magnetic Reynolds number based on the fluid velocity, is the important parameter for the perturbation field solution since it controls the ratio of convection to diffusion for the field.

The normal method of solving boundary-value problems is to determine the natural modes in each region from the geometry, and then use the boundary conditions to find the constants. Here the modes are not evident except for the special case of an ideal

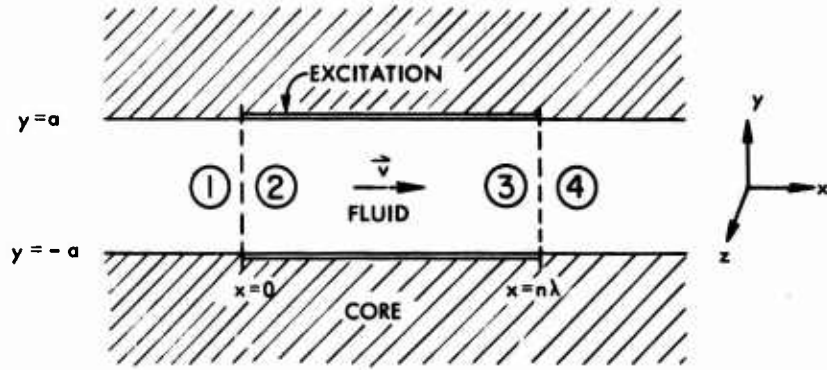


Fig. 47. The Model.

core, considered in section 6.3. Instead, the double-ended Laplace transform of the x -variation is taken, and then the boundary conditions are used. This gives the total solution at once, provided the inverse transform can be evaluated.

The transform used is

$$\underline{A}_f(p, y) = \int_{-\infty}^{\infty} \underline{A}_f(x, y) e^{-pkx} dx, \quad (194)$$

where p is the complex transform variable, normalized with respect to the wave number k of the excitation. The transformed equations are

$$\frac{\partial^2 \underline{A}_f(p, y)}{\partial y^2} + k^2 \left[p^2 - jR_M - R_{MF}p \right] \underline{A}_f(p, y) = 0, \quad (195)$$

and

$$\frac{\partial^2 \underline{A}_c(p, y)}{\partial y^2} + k^2 \left[p^2 - jR_{Mc} \right] \underline{A}_c(p, y) = 0. \quad (196)$$

These are identical in form with Eqs. 66 and 69, so that the y -dependence will again be an exponential. Using symmetry and the boundary conditions at the fluid-core interface, the solution is

$$\underline{A}_f(p, y) = \frac{\mu_f \underline{K}(p) \cosh \gamma(p) ky}{k \left[\gamma(p) \sinh \gamma(p) a + \kappa \delta(p) \cosh \gamma(p) a \right]} \quad \text{for } |y| \leq a, \quad (197)$$

and

$$\underline{A}_c(p, y) = \frac{\mu_f \underline{K}(p) e^{-\delta(p) k (|y| - a)}}{k [\gamma(p) \tanh \gamma(p) a + \kappa \delta(p)]} \text{ for } |y| \geq a, \quad (198)$$

where

$$[\gamma(p)]^2 = -p^2 + jR_M + R_{MF}p, \quad (199)$$

and

$$[\delta(p)]^2 = -p^2 + jR_{Mc} \quad (200)$$

have the same form as before but now depend on p , and $\underline{K}(p)$ is the transform of the exciting current.

For a uniform traveling current of length $n\lambda$,

$$\underline{K}(p) = \frac{NI [1 - e^{-(p+j)2\pi n}]}{k(p+j)}. \quad (201)$$

This is the sum of a positive step at $x = 0$ and a negative step at $x = n\lambda$, so that superposition can be used to find the total field solution. The field due to the positive step is calculated first. The field due to the negative step at the exit is then the negative of this, delayed in space by a length $n\lambda$, and with the appropriate phase shift required for the negative step, $e^{-j2\pi n}$. The phase shift is zero if the machine is an integral number of wavelengths long. It is not necessary to carry the negative step throughout the calculations; it is used only as needed for the exit fields and powers.

The transformed vector potential in the fluid is

$$\underline{A}_r(p, y) = \frac{\mu_f NI [1 - e^{-(p+j)2\pi n}] \cosh \gamma ky}{k^2 (p+j) (\gamma \sinh \gamma a + \kappa \delta \cosh \gamma a)}, \quad (202)$$

where the dependence of γ and δ on p is not explicitly indicated. The inverse transform of this is evaluated as a contour integral, which is the sum of the residues at the poles enclosed within the contour. The poles are the values of p at which the denominator is zero. One pole is

$$p_e = -j, \quad (203)$$

due to the excitation, and this gives the field with no ends. The other poles are determined by

$$\gamma \sinh \gamma a + \kappa \delta \cosh \gamma a = 0. \quad (204)$$

There is no general solution for Eq. 204, but an analytical solution for the poles is known for an ideal iron core,^{63,34} treated in sections 6.3 and 6.4. The solution for a lossless core of arbitrary permeability is discussed in section 6.5, and the extension to include core loss is mentioned in section 6.6. Numerical solutions are required for these cases.

6.3 THE IDEAL CORE – FIELDS AND IMPEDANCE

For an ideal iron core, $\kappa = 0$, the natural poles, determined by

$$\gamma \sinh \gamma a = 0, \quad (205)$$

occur when $\gamma a = j i \pi$, or when

$$p_i^\pm = \frac{R_{MF}}{2} \left[1 \pm \sqrt{1 + \frac{j^4}{R_{MF}^2 (1-s)} + \left(\frac{2i\pi}{a R_{MF}} \right)^2} \right]. \quad (206)$$

The \pm sign of p_i^\pm goes with the sign before the radical. The natural response depends on R_{MF} rather than R_M , as expected, because the ratio of convection to diffusion determines the end fields.

The transform is not essential for this case as the modes can be determined from the boundary conditions at the ideal iron core. The x-component of the perturbation magnetic field is antisymmetric, and must be zero at the coils since the surface current matches the excitation term. This is satisfied only by a vector potential proportional to $\cos(i\pi y/a)$, where i is an integer. Assuming an x-dependence of the form e^{pkx} and substituting in Eq. 195 gives Eq. 206 for p_i . The coefficients of the cosine terms, determined from the boundary conditions at $x = 0$ and $n\lambda$, agree with the transform results. The excitation vector potential is essentially independent of y for a slit channel, so that only the two $i = 0$ terms are required from the Fourier series to satisfy the boundary conditions. This establishes that the other terms are small for a practical machine. For a non-ideal core the field is not zero at the walls, and the transform approach is accordingly needed.

The residues at the poles are given by

$$\text{Res} \left\{ \underline{A_f}(p, y) \right\} \bigg|_{p = p_i^\pm} = k (p - p_i^\pm) \underline{A_f}(p, y) \bigg|_{p = p_i^\pm}. \quad (207)$$

To evaluate this, the denominator is expanded in a Taylor series about the pole,

$$\gamma \sinh \gamma a = (-1)^i a \left(\frac{R_{MF}}{2} - p_i^\pm \right) (p - p_i^\pm) \text{ for } i \neq 0, \quad (208)$$

plus higher order terms which make no contribution to the residue. The case $i = 0$ is not included in (208) because then $\gamma = 0$, and the series involves the ratio $0/0$. Treating this case properly results in

$$\gamma \sinh \gamma a = 2a \left(\frac{R_{MF}}{2} - p_0^\pm \right) (p - p_0^\pm). \quad (209)$$

The $i = 0$ terms will differ by a factor of 2 from the others, so that it is convenient to define

$$\Delta_i = \begin{cases} 2 & \text{for } i = 0 \\ 1 & \text{for } i \neq 0. \end{cases} \quad (210)$$

The residues could also be obtained by using small-angle formulas.

Examination of the square-root term in Eq. 206 shows that the real part is always greater than one, and that both the real and imaginary parts are positive. The $+$ poles, with positive real and imaginary parts, are the poles for negative x , since the natural response must decay away from the entrance. Similarly, the $-$ poles have negative real and imaginary parts and apply to positive x .^{*} The vector potential due to the entrance, the sum of the residues of the transformed potential, is

$$\underline{A_f}(x,y) = - \sum_{i=0}^{\infty} \frac{\mu_f NI (-1)^i \cos \frac{i\pi y}{a} e^{p_i^+ kx}}{\alpha k \Delta_i (p_i^+ + j) \left(\frac{R_{MF}}{2} - p_i^+ \right)} \quad \text{for } x < 0, \quad (211)$$

and

$$\begin{aligned} \underline{A_f}(x,y) = & \frac{\mu_f NI \cosh \gamma (-j) ky e^{-jkx}}{k\gamma (-j) \sinh \gamma (-j) a} \\ & + \sum_{i=0}^{\infty} \frac{\mu_f NI (-1)^i \cos \frac{i\pi y}{a} e^{p_i^- kx}}{\alpha k \Delta_i (p_i^- + j) \left(\frac{R_{MF}}{2} - p_i^- \right)} \quad \text{for } x > 0, \end{aligned} \quad (212)$$

where $\gamma(-j)$ is the previous definition for the excitation response, Eq. 38a. The minus sign for the $x < 0$ solution arises because the contour encircles the poles in a clockwise direction. The exit fields, centered about $x = n\lambda$, have to be added to the above.

^{*}This can also be seen from the contour integral (Appendix F) which is closed to the right for $x < 0$, and to the left for $x > 0$, so that the contribution from the semicircle is negligible.

The inverse transform and the method of handling the doubly infinite series of poles are discussed in Appendix F because it is not evident that the usual procedure works in this case. The poles extend to infinity in both directions along the real axis, as shown in Fig. F-1, so that the requirement that the function approach zero far from the imaginary axis is not satisfied. For large i the poles are proportional to i and the residues to $1/i^2$, and the series converges.

Comparing the above results with the discussion in section 6.1, it is seen that the poles and residues are symmetric about the ends of the machine provided the fluid is stationary. For a moving fluid the poles are not symmetric; the $+$ poles have a larger real part, faster decay, and smaller residues.

Further information is obtained by restricting attention to the regime of practical machine parameters; $|s| \ll 1$ for high efficiency, $\alpha \ll 1$ for a reasonable power density, and $|sR_M| \gg 1$ for the reactive power to be small compared to the real power. The value of αR_{MF} will probably be around unity, making the coefficient of i in the last term under the radical sign in Eq. 206 large and causing an appreciable increase in the poles from $i = 0$ to $i = 1$. The residues for $i \neq 0$ are small compared to the residues for $i = 0$, as in also seen from the Fourier series approach to the modes mentioned earlier, and the exponentials decay much faster. The fields and powers, with small error, can be calculated using only the excitation and $i = 0$ components for this case. The calculations of section 6.4 show that the powers due to the $i \neq 0$ terms are at least two orders of magnitude smaller than the powers due to the $i = 0$ components for reasonable parameter values.

Consider next the poles for $i = 0$. For the region of interest $4/[R_{MF}(1-s)]$ will be less than one, and Eq. 206 may be written approximately as

$$p_o^\pm = \frac{R_{MF}}{2} \left[1 \pm \left(1 + \frac{2j}{R_{MF}(1-s)} + \frac{2}{R_{MF}^2(1-s)^2} \right) \right], \quad (213)$$

retaining only the leading terms of the binomial series. The $+$ pole has a decay length, $1/[2\pi \text{Re}\{p_o^+\}]$ in wavelengths, of $1/2\pi R_{MF}$. This is small, a few hundredths of a wavelength. The $-$ pole has a decay length of $R_{MF}(1-s)^2/2\pi$, which may be several wavelengths. This clearly shows the asymmetry of the perturbation fields, and that the perturbation fields may extend an appreciable distance into the machine.

The coil impedance for a finite-length machine will be a function of the coil location. Using the methods developed in Section II, the potential in the exciting coils is found from the vector potential. Evaluating Eq. 25 for the coil voltage and calculating the impedance gives

$$\frac{Z}{R_o} = \frac{R_e}{R_o} + \frac{j}{\gamma(-j) \tanh \gamma(-j) a} + \sum_{i=0}^{\infty} \left\{ \frac{j (e^{2\pi p_i^-} - 1)}{2\pi a \Delta_i (p_i^- + j) \left(\frac{R_{MF}}{2} - p_i^- \right)} \left[\frac{e^{(p_i^- + j) kx}}{(p_i^- + j)} \pm \frac{e^{(p_i^- - j) kx}}{(p_i^- - j)} \right] \right\} \quad (214)$$

for a coil one wavelength long, where R_o and R_e are given by Eqs. 49 and 50. The \pm sign is for the two phases; + for the $\cos kx$ coils, and - for the $\sin kx$ coils. The first term is the resistance of the coil, because of its finite conductivity, the second is the impedance with no ends, and the remaining terms are the contribution from the perturbation field. The coil impedance is a function of x , where x is the location of the beginning of the coil. For the $\cos kx$ coils, x is 0, λ , 2λ , etc. The exit field is not included in this calculation, but its effect is small because the perturbation field at the exit is mainly outside the machine.

Several sets of curves of the series-equivalent resistance and inductance for the $\cos kx$ coils are included to show the magnitude of the impedance perturbation and the series of damped sinusoids. The curves only have physical significance when used with an actual coil structure; the impedance of each coil is then determined from the curve using the value of x at which the coil starts. The curves are oscilloscope pictures taken directly from the computer, and are normalized so that the asymptote of each curve is the resistance or inductance with no end effect. The range of x covered in wavelengths is given for each curve, along with the machine parameters s , R_M , and a . All curves are for perfectly-conducting exciting coils.

The resistance and inductance for a reasonable operating point, $R_M = 10$ and $a = 0.1$, are shown in Fig. 48a through 48d for several negative values of the slip. For $s = -0.01$ the resistance is positive for about the first three wavelengths, so that a short machine will not operate as a generator. As the magnitude of s increases for negative values, a large-scale oscillation develops in addition to the small-scale oscillation. This gross oscillation arises from the $e^{(p_o^- + j) kx}$ term of Eq. 214, which is the larger of the two exponentials. The real part of p_o^- is small, and the imaginary part is close to -1, from Eq. 213, so that the denominator of the first exponential is smaller than the denominator of the second. It represents an oscillation of wavelength $-[(1 - s)/s]\lambda$, where λ is the excitation wavelength. This gives the correct wavelength of the gross oscillations for the $s = -0.2$, -0.5 , and -1 curves. (Note the different x scale for the $s = -1$ curve.) The decay length for the oscillation increases with increasing negative values of s , but the net end effect decreases, as is best seen from the powers.

Increasing R_M results in a longer decay length, while for smaller R_M the decay is more rapid but the oscillations are larger. The case $s = -1$ and $R_M = 0.1$, Fig. 48e, has a much larger oscillation which becomes negligible in only a few wavelengths. This is not a good operating point.

For the cases shown the normalized curves are almost independent of α , the difference between $\alpha = 0.01$ and $\alpha = 1$ being negligible. Also, the change from the cosine to sine coils has no effect on the gross behavior and only a slight effect on the oscillations. Finally, note that the oscillations are 90° out of phase for R_s and L_s , as they should be for the real and imaginary parts of Eq. 214.

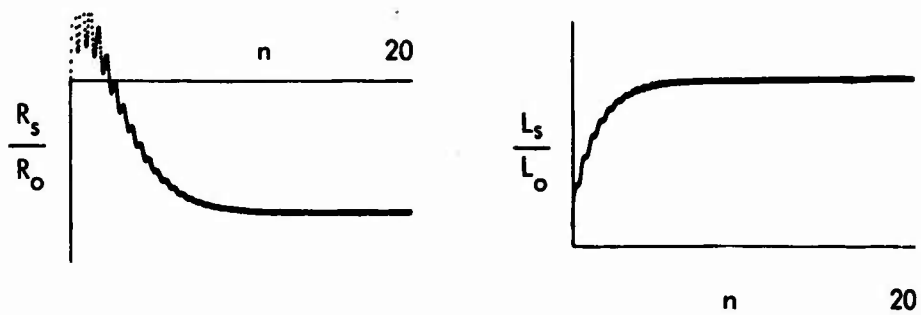
The impedance gives a poor picture of the change in the machine performance with length because of the gross oscillation and the necessity of summing over several coils (points). The powers give a better picture because the integral over the length averages the oscillation, and only one point on the curve is required.

6.4 THE IDEAL CORE – POWERS

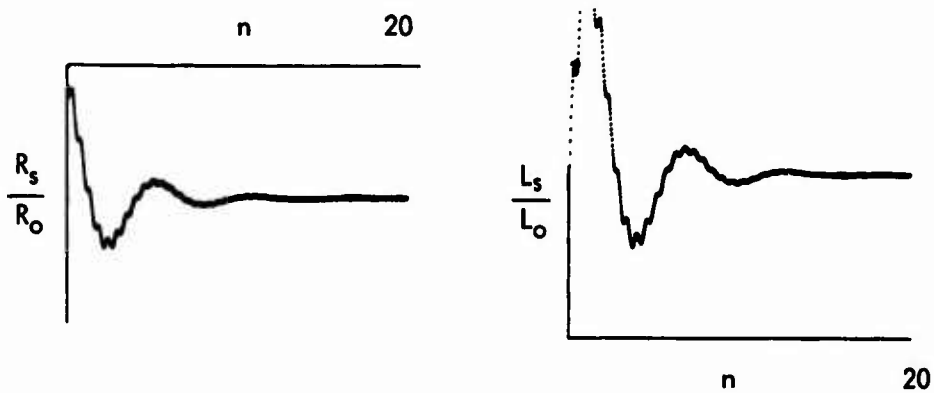
The power calculations are considerably more complicated than for the infinite-length machine because of the infinite sums and the four distinct regions of space shown in Fig. 47. Regions 1 and 2 are before and after the entrance, and regions 3 and 4 are before and after the exit. For a long machine there is also a central core where the infinite-length machine conditions exist. The complete field solution is already known in terms of the entrance solution of section 6.3 and the spatial and phase delays because of the negative step at the exit. The fields in regions 1 and 2 are the solutions obtained for $x < 0$ and $x > 0$, Eqs. 211 and 212. The fields in regions 3 and 4 are the negative of those in regions 1 and 2 respectively from the negative step, multiplied by $e^{-j2\pi n}$ from the phase shift, and centered about $x = n\lambda$.

The power calculations are simplified by breaking the powers up by regions and sources, and by using the field properties. Only P_s and P_m are considered, as P_r can then be determined. For convenience, the powers are split into four parts depending on which fields are the sources: the excitation powers, the perturbation powers resulting from cross-products between the excitation and perturbation fields, the perturbation powers that are due to fields at the entrance or exit alone, and the perturbation powers attributable to coupling between the entrance and exit fields. The excitation powers are already known from the results of Section III.

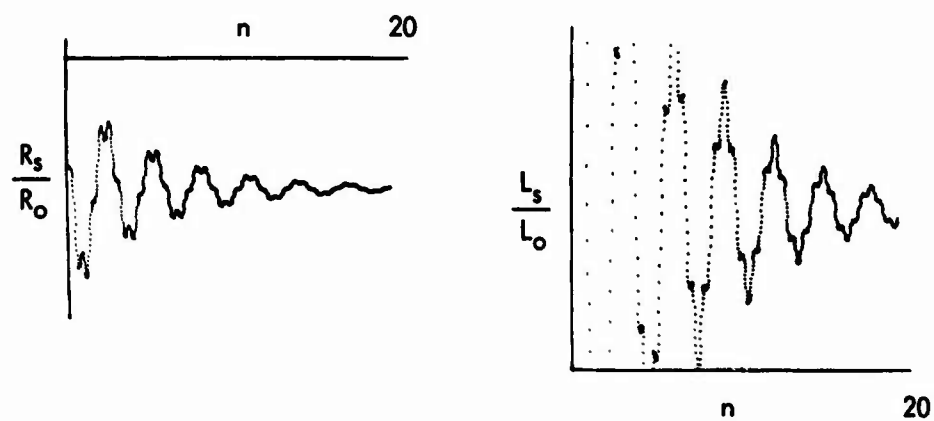
Consider first the power supplied by the exciting system to the fluid, P_s , which is the integral of the y-component of Poynting's vector at the channel wall. Since the longitudinal perturbation magnetic field B_x is zero at the wall, the perturbation power reduces to the integral of a sum of terms of the type B_x because of the excitation times E_z for the i-th pole. There are no cross terms between different values of i, and no coupling between the entrance and exit fields. The integral extends only from $x = 0$ to $x = n\lambda$ because the excitation field is zero elsewhere.



(a)



(b)



(c)

Fig. 48. Continued on next page.

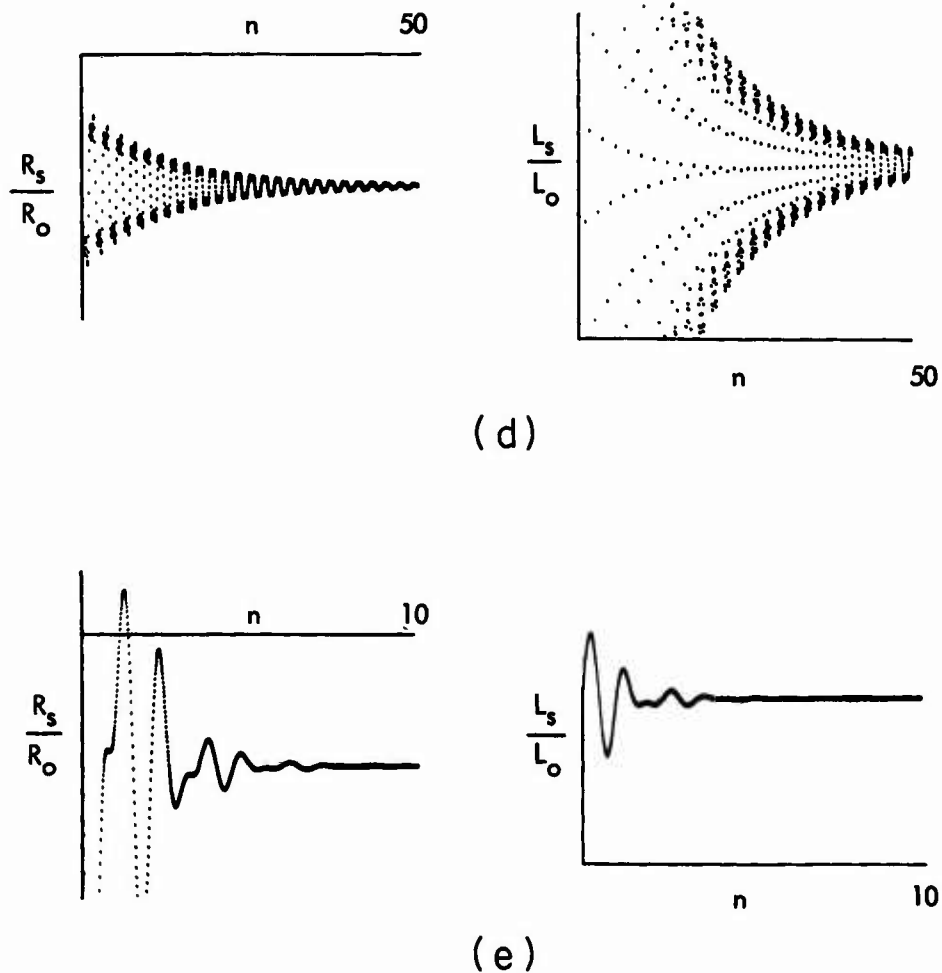


Fig. 48. Finite-length, ideal-core, series-equivalent resistance and inductance for cosine coils versus n : (a) for $s = -0.01$, $R_M = 10$, $a = 0.1$; (b) for $s = -0.2$, $R_M = 10$, $a = 0.1$; (c) for $s = -0.5$, $R_M = 10$, $a = 0.1$; (d) for $s = -1.0$, $R_M = 10$, $a = 0.1$; (e) for $s = -1.0$, $R_M = 0.1$, $a = 0.1$.

The mechanical power output, P_m , is more complicated. The fields at the entrance and exit are the same, except for the excitation field. Thus P_{m3} , the perturbation power in region 3, is the sum of P_{m1} , which is due wholly to the perturbation field, plus the coupling power between the excitation and perturbation fields. Similarly, P_{m2} is P_{m4} plus the coupling term. The values of P_{m1} and P_{m4} are independent of the length of the machine as the fields which yield them extend throughout all space within the channel boundaries. The powers are modified, however, by the addition of a second type of coupling, between entrance and exit perturbation fields, if the machine is not long. These powers, denoted by P_{m24} , P_{m23} and P_{m13} for the fields involved, are listed in order of importance since the perturbation fields are larger after the steps than before the steps. As $n\lambda$ becomes large, these quickly approach zero.

The mechanical power is the integral of field products over the volume of the channel. Because the integral over a length a of the product of two terms proportional to $\cos(i\pi y/a)$ is zero unless i is the same for both terms, there are no cross products except between the $\cosh \gamma ky$ variation of the excitation field and the perturbation field terms. For the region of practical interest ($\gamma a \ll 1$ so that $\cosh \gamma ky \approx 1$), there is coupling only between the excitation and $i = 0$ fields, denoted by the subscript $e0$. The $e0$ terms are the dominant contribution to the mechanical power, with the input-output coupling terms smallest except for a machine less than a wavelength long.

Turning next to the calculation of the powers, the formulas used, from section 2.4, are

$$\bar{P}_s = -\frac{c}{\mu_f} \int_0^{n\lambda} \operatorname{Re} \left\{ \underline{E}_{fz} \underline{B}_{fx}^* \right\} \Big|_{y=a} dx, \quad (215)$$

and

$$P_m = - \int_{\text{vol}} v \operatorname{Re} \left\{ \frac{J_{fz} B_{fy}^*}{2} \right\} dx dy dz, \quad (216)$$

where the field quantities are expressed as the sum of the excitation plus the perturbation fields. The resulting equations are presented in Table 11 for the four regions, making use of the properties mentioned previously. A slit channel is assumed so that coupling terms to the excitation field in P_m are zero unless $i = 0$. This assumption is not used elsewhere, not even in calculating the $e0$ term. The normalization constant P_0 and the powers are in terms of a machine of length $n\lambda$. This normalization is chosen so that the asymptotic powers are horizontal lines, making deviations easy to recognize.

Table 11. Powers attributable to finite machine length.

Region 1

$$\frac{P_{m1}}{P_o} = - \frac{\alpha R_{MF}}{4\pi n} \operatorname{Re} \left\{ \sum_{i=0}^{\infty} \frac{\Delta_i (j + (1-s) p_i^+) p_i^{+*}}{(p_i^+ + p_i^{+*})} \underline{C_i^+} \underline{C_i^{+*}} \right\}$$

$$\frac{P_{s1}}{P_o} = 0$$

Region 2[†]

$$P_{m2} = P_{m2e0} + P_{m4}$$

$$\begin{aligned} \frac{P_{m2e0}}{P_o} = \frac{R_{MF}}{2\pi n} \operatorname{Re} \left\{ \frac{j s p_o^{-*} \underline{C_o^{-*}}}{\gamma^2 (p_o^{-*} - j)} \left[1 - e^{(p_o^{-*} - j) 2\pi n} \right] \right. \\ \left. + \frac{j (j + (1-s) p_o^-)}{\gamma^{*2} (p_o^- + j)} \underline{C_o^-} \left[1 - e^{(p_o^- + j) 2\pi n} \right] \right\} \end{aligned}$$

$$\frac{P_{s2}}{P_o} = \frac{-1}{2\pi n} \operatorname{Re} \left\{ \sum_{i=0}^{\infty} \frac{j (1 - e^{(p_i^- + j) 2\pi n})}{\Delta_i \alpha (p_i^- + j)^2 \left(\frac{R_{MF}}{2} - p_i^- \right)} \right\}$$

Region 3[†]

$$P_{m3} = P_{m3e0} + P_{m1}$$

$$\begin{aligned} \frac{P_{m3e0}}{P_o} = \frac{R_{MF}}{2\pi n} \operatorname{Re} \left\{ \frac{j s p_o^{+*} \underline{C_o^{+*}}}{\gamma^2 (p_o^{+*} - j)} \left[1 - e^{-(p_o^{+*} - j) 2\pi n} \right] \right. \\ \left. + \frac{j (j + (1-s) p_o^+)}{\gamma^{*2} (p_o^+ + j)} \underline{C_o^+} \left[1 - e^{-(p_o^+ + j) 2\pi n} \right] \right\} \end{aligned}$$

[†]Less excitation powers.

Table 11. Powers attributable to finite machine length (Cont.).

$$\frac{P_{s3}}{P_o} = \frac{1}{2\pi n} \operatorname{Re} \left\{ \sum_{i=0}^{\infty} \frac{j \left(1 - e^{-(p_i^+ + j) 2\pi n} \right)}{\Delta_i a(p_i^+ + j)^2 \left(\frac{R_{MF}}{2} - p_i^+ \right)} \right\}$$

Region 4

$$\frac{P_{m4}}{P_o} = \frac{aR_{MF}}{4\pi n} \operatorname{Re} \left\{ \sum_{i=0}^{\infty} \frac{\Delta_i \left(j + (1 - s) p_i^- \right)}{(p_i^- + p_i^{+*})} p_i^{+*} \underline{C_i^-} \underline{C_i^{+*}} \right\}$$

$$P_{s4} = 0$$

Coupling

$$\frac{P_{m13}}{P_o} = \frac{aR_{MF}}{4\pi n} \operatorname{Re} \left\{ \sum_{i=0}^{\infty} \frac{\Delta_i \left(j + (1 - s) p_i^+ \right)}{(p_i^+ + p_i^{+*})} p_i^{+*} \underline{C_i^+} \underline{C_i^{+*}} \right. \\ \left. \left(e^{-(p_i^{+*} - j) 2\pi n} + e^{-(p_i^{+*} + j) 2\pi n} \right) \right\}$$

$$\frac{P_{m23}}{P_o} = \frac{-aR_{MF}}{4\pi n} \operatorname{Re} \left\{ \sum_{i=0}^{\infty} \left[\frac{\Delta_i \left(j + (1 - s) p_i^- \right)}{(p_i^- + p_i^{+*})} p_i^{+*} \underline{C_i^-} \underline{C_i^{+*}} e^{j2\pi n} \right. \right. \\ \left. \left(e^{p_i^- 2\pi n} - e^{-p_i^{+*} 2\pi n} \right) \right. \\ \left. \left. + \frac{\Delta_i \left(j + (1 - s) p_i^+ \right)}{(p_i^+ + p_i^{+*})} p_i^{+*} \underline{C_i^+} \underline{C_i^{+*}} e^{-j2\pi n} \left(e^{p_i^{+*} 2\pi n} - e^{-p_i^+ 2\pi n} \right) \right] \right\}$$

Table 11. Powers attributable to finite machine length (Cont.).

$$\frac{P_{m24}}{P_o} = \frac{-\alpha R_{MF}}{4\pi n} \operatorname{Re} \left\{ \sum_{i=0}^{\infty} \frac{\Delta_i (j + (1-s) p_i^-)}{(p_i^- + p_i^{-*})} p_i^{-*} \underline{C_i^-} \underline{C_i^{-*}} \right. \\ \left. \left(e^{(p_i^{-*} - j) 2\pi n} + e^{(p_i^- + j) 2\pi n} \right) \right\}$$

Totals

$$P_m = P_{me} + P_{m2e0} + P_{m3e0} + 2P_{m1} + 2P_{m4} + P_{m13} + P_{m23} + P_{m24}$$

$$P_s = P_{se} + P_{s2} + P_{s3}$$

Normalization

$$P_o = \mu_f v_s N^2 I^2 c 2\pi n / k$$

$$\underline{C_i^{\pm}} = \mp \frac{(-1)^i}{\Delta_i \alpha (p_i^{\pm} + j) \left(\frac{R_{MF}}{2} - p_i^{\pm} \right)}$$

NOTE: n is length in wavelengths

The variation of P_s/P_o , P_m/P_o , and $e_g = (P_s/P_m)$ with the length in wavelengths n is shown in Fig. 49a through 49f for several sets of machine parameters. The dashed line at the top marks the values with no end effect for reference. There is clearly a minimum length below which the machine will not operate as a generator. The rise in e_g is much faster than in P_s , showing the small change in efficiency. The end effect decreases for larger negative slips, despite the longer decay length, because the denominator is larger, making the net contribution smaller. The end effect is larger at smaller R_M for this reason, and penetrates further into the machine, as shown by the figures.

The total powers for a machine 6 wavelengths long are given in Table 12, normalized to be one if the end powers are zero. This again shows the large end effect for small s, so that there is a maximum obtainable electrical efficiency, probably around 90% for $R_M = 10$ and a 6 wavelength machine. For $s = -0.2$ and $R_M = 10$, the powers are

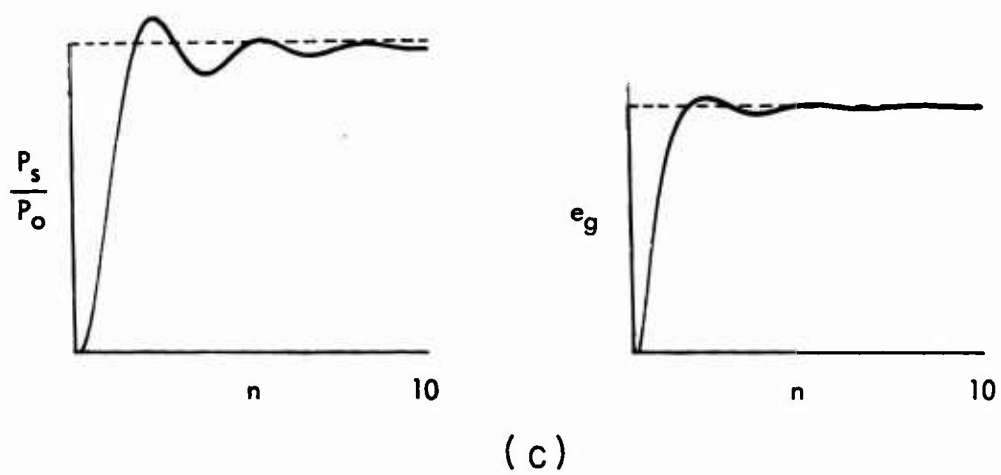
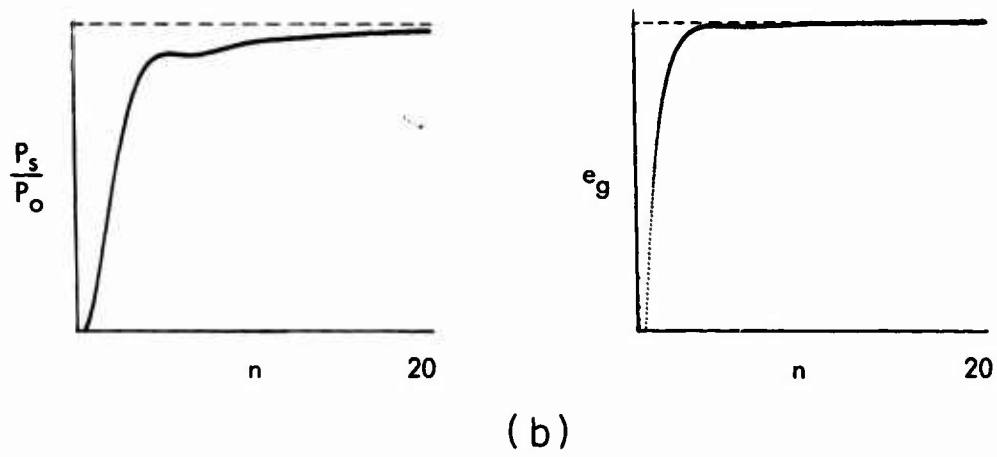
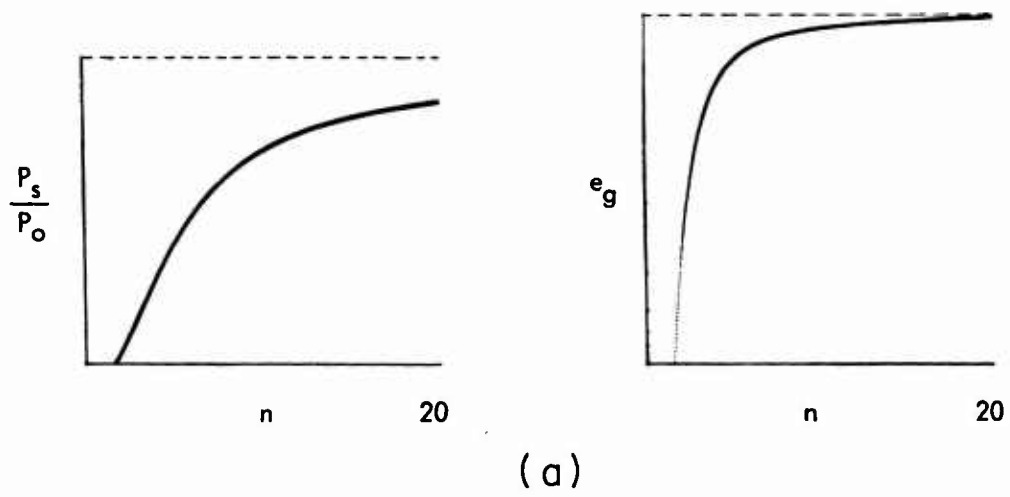


Fig. 49. Continued on next page.

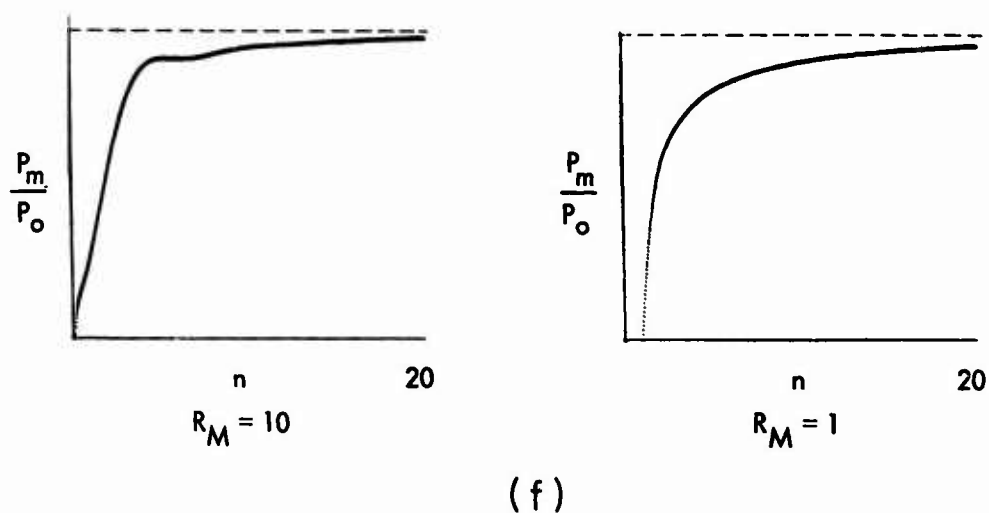
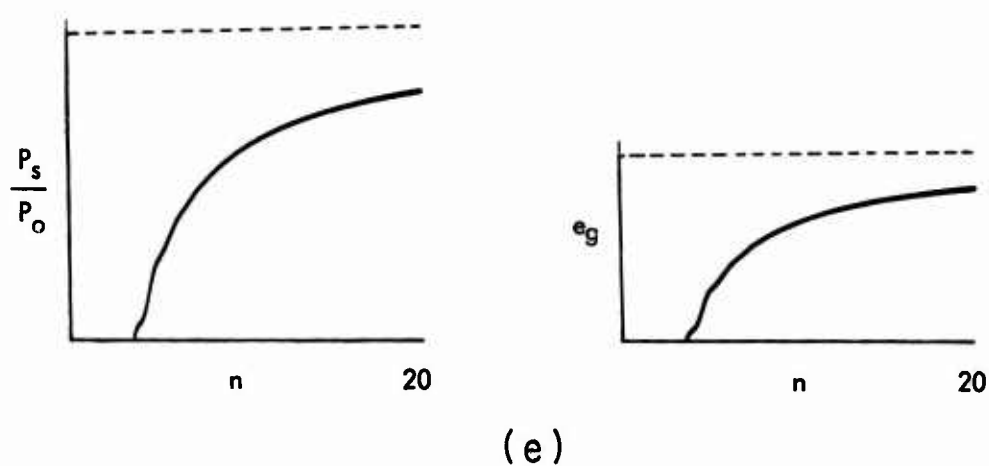
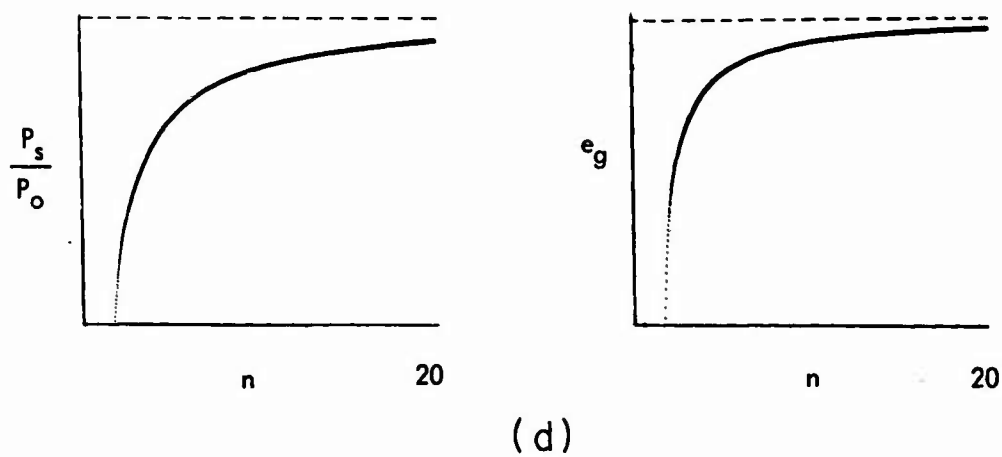


Fig. 49. Fine-length, ideal-core, P_s and e_g versus n : (a) for $s = -0.05$, $R_M = 10$, $a = 0.1$; (b) for $s = -0.2$, $R_M = 10$, $a = 0.1$; (c) for $s = -0.5$, $R_M = 10$, $a = 0.1$; (d) for $s = -0.2$, $R_M = 1$, $a = 0.1$; (e) for $s = -1$, $R_M = 0.1$, $a = 0.1$; (f) P_m vs n for $s = -0.2$, $a = 0.1$; $R_M = 10$ and 1 .

decreased by 10%, but the change in the electrical efficiency is small. This becomes worse as R_M is decreased, both the power and efficiency are smaller, showing that R_M must be large to reduce the end effects.

In the calculation of the powers, the primary contribution is from the $i = 0$ terms, and the higher-order terms are small for practical machine parameters, as is illustrated in Table 13 for the mechanical powers. The numbers are the terms of Table 11 less the exponentials of P_{m2e0} and P_{m3e0} , and without n in the normalization. The coupling powers are not included. The only terms of significant magnitude are the $e0$ and $i = 0$ terms, except for large slip. The first two columns show that P_{m2} and P_{m4} dominate over P_{m3} and P_{m1} because of the asymmetry of the fields. Comparing the total perturbation power for a long machine, all exponentials set equal to zero, with the excitation power per wavelength shows roughly how much of the length goes to counteract the end effect. For small slip this is appreciable, as expected from the results of Table 12 and Fig. 49. A similar table could be made for P_s , but it would not show anything additional.

Table 12. Total powers and efficiencies for a generator 6 wavelengths long.

s	R_M	α	P_s^*	P_m^*	e_g	e_∞^\dagger
- 0.05	10	0.1	0.483	0.537	85.6%	95.2%
- 0.1	10	0.1	0.697	0.723	87.6	90.9
- 0.2	10	0.1	0.897	0.909	82.3	83.3
- 0.3	10	0.1	0.927	0.939	75.9	76.9
- 0.5	10	0.1	0.984	0.986	66.5	66.7
- 1	10	0.1	0.997	0.997	50.0	50.0
- 5	10	0.1	1.000	1.002	16.6	16.7
- 0.01	100	0.1	0.033	0.049	66.6	99.0
- 0.1	100	0.1	0.971	0.971	90.9	90.9
- 0.2	5	0.1	0.842	0.866	81.0	83.3
- 0.2	1	0.1	0.716	0.841	71.0	83.3

* P_s , P_m are normalized to 1 if there is no end effect.

$\dagger e_\infty = \frac{1}{1-s}$ is the efficiency with no end effect.

The results of this section put further limits on the machine parameters. The slip cannot be very small or the efficiency and end effect become objectionable. If R_M is not large, say greater than unity, the end effect is again large. Finally, the machine has to be several wavelengths long.

Table 13. Mechanical power coefficients from Table 11 for $\alpha = 0.1$. *

$\frac{s}{i}$	R_M	$\frac{P_{m3}}{P_o}$	$\frac{P_{m2}}{P_o}$									
			- 0.1 10	- 0.2 10	- 0.5 10	- 1.0 10	- 0.01 100	- 0.1 100	- 0.2 1			
e0		0.106	7.98	2.52	0.217	2.35×10^{-2}	79.6	0.311	1.09			
0		$- 6.72 \times 10^{-3}$	0.351	0.130	2.03×10^{-2}	3.94×10^{-3}	0.394	7.16×10^{-3}	0.410			
1		$- 1.26 \times 10^{-4}$	$- 1.79 \times 10^{-4}$	$- 2.15 \times 10^{-4}$	$- 3.46 \times 10^{-4}$	$- 6.37 \times 10^{-4}$	$- 1.27 \times 10^{-3}$	$- 1.43 \times 10^{-3}$	$- 1.88 \times 10^{-5}$			
2		$- 1.76 \times 10^{-5}$	$- 2.10 \times 10^{-5}$	$- 2.52 \times 10^{-5}$	$- 4.01 \times 10^{-5}$	$- 7.33 \times 10^{-5}$	$- 2.07 \times 10^{-4}$	$- 2.42 \times 10^{-4}$	$- 2.33 \times 10^{-6}$			
3		$- 5.41 \times 10^{-6}$	$- 6.07 \times 10^{-6}$	$- 7.26 \times 10^{-6}$	$- 1.15 \times 10^{-5}$	$- 2.09 \times 10^{-5}$	$- 6.29 \times 10^{-5}$	$- 7.47 \times 10^{-5}$	$- 6.89 \times 10^{-7}$			
10		$- 1.53 \times 10^{-7}$	$- 1.58 \times 10^{-7}$	$- 1.88 \times 10^{-7}$	$- 2.96 \times 10^{-7}$	$- 5.29 \times 10^{-7}$	$- 1.50 \times 10^{-6}$	$- 1.79 \times 10^{-6}$	$- 1.85 \times 10^{-8}$			
$P_{m2} (P_{m3})$		9.88×10^{-2}	8.33	2.65	0.237	2.67×10^{-2}	80.0	0.316	1.50			
$P_{m4} (P_{m1})$		$- 6.87 \times 10^{-3}$	0.351	0.130	1.99×10^{-2}	3.19×10^{-3}	0.392	5.34×10^{-3}	0.410			
Total†			8.78	2.85	0.287	4.47×10^{-2}	80.4	0.322	2.20			
Excitation‡			- 5.50	- 4.80	- 2.88	- 1.98	- 5.05	- 1.09	- 2.31			

*Without n, the exponents of P_{M2eo} and $P_{M3eo'}$ and the coupling terms.

†Total mechanical perturbation power in a long machine, all exponentials set equal to zero.

‡For one wavelength.

6.5 LOSSLESS-CORE MACHINE

A machine with a lossless core of arbitrary permeability is treated by an extension of the previous theory. This model applies to an air-core machine, which has been proposed for space-vehicle applications, despite the lower power density and poor power factor, on the grounds that weight and temperature limitations make the use of iron unacceptable.^{64,65} The arbitrary-core problem is more complicated since:

1. An analytical solution for the poles is not available, although equations can be found for the fields, impedance, and powers in terms of the unknown poles.
2. The fields are no longer orthogonal for the power calculations.
3. The fields are not zero in the core.

The solution is described, but not carried through in the same detail as for the ideal-core machine.

The poles for a lossless core, $\delta = 1$, are determined from Eq. 204. Writing γ as the sum of real and imaginary parts shows that γ must be pure imaginary, $\gamma = jb$, and that

$$b \tan ba - \kappa = 0. \tag{217}$$

The roots of Eq. 217, denoted by b_i , cannot be determined analytically, although numerical methods, such as the Newton-Raphson method of iteration,⁶⁵ are available. For $\kappa a \ll 1$ or $ba \gg 1$ the roots become the same as for the ideal core, as shown by the graph of Eq. 217, Fig. 50, and the table of roots, Table 14. The arbitrary-core roots are the intersections of the two curves, the ideal core roots are the points where the tangent curve crosses the axis. The difference is small except for $i = 0$.

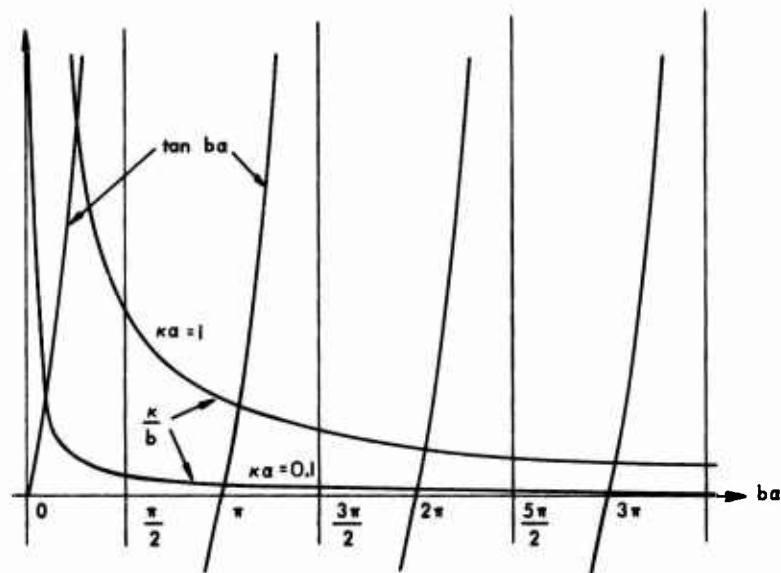


Fig. 50. Graph of Eq. 217.

Table 14. Roots of Eq. 217 or Fig. 50.

i	$b_i a$, Arbitrary Core			$b_i a$, Ideal Core
	$\kappa a = 0.01$	$\kappa a = 0.1$	$\kappa a = 1$	$i\pi$
0	0.09983	0.3111	0.8603	0
1	3.145	3.173	3.426	3.142
2	6.285	6.299	6.437	6.283
3	9.426	9.435	9.529	9.425
4	12.57	12.57	12.65	12.57
5	15.71	15.71	15.77	15.71

The poles, in terms of these roots, are

$$p_i^{\pm} = \frac{R_{MF}}{2} \left[1 \pm \sqrt{1 + \frac{j4}{R_{MF}(1-s)} + \left(\frac{2b_i}{R_{MF}} \right)^2} \right], \quad (218)$$

which is Eq. 206 if $b_i = (i\pi/a)$. The poles for an arbitrary core lie on the same curve in the p-plane as the ideal core poles but at different points.

There is one important distinction for the non-ideal core. The lowest root, b_0 , is no longer zero, but lies between zero and $\pi/2a$, as seen from Fig. 50. The real part of the square root of Eq. 218 for $i = 0$ will be larger, and the decay length for p_0^{\pm} significantly less, than for an ideal core. For the practical parameter values $s = -0.1$, $R_M = 10$, and $a = 0.1$, the decay length is 2.1 wavelengths for an ideal core, but only 0.18 wavelengths for an air core. The other roots, and thus the poles, are essentially unchanged, as shown. The zero-order field will not be much larger than the others and will not dominate the powers. The perturbation field decays faster, and may for this reason have a smaller net effect on the performance.

The residues are again found by expanding the denominator in a series about the pole, resulting in

$$\gamma \sinh \gamma a + \kappa \cosh \gamma a = \cos(b_i a) \frac{[\kappa + a(\kappa^2 + b_i^2)]}{b_i^2} \left(\frac{R_{MF}}{2} - p_i^{\pm} \right) (p - p_i^{\pm}) \quad (219)$$

plus higher order terms, which reduces to Eq. 208 for $\kappa = 0$. Here, no distinction is required for $i = 0$. The vector potential is

$$\underline{A_f}(x,y) = - \sum_{i=0}^{\infty} \frac{\mu_f N i b_i^2 \cos b_i k y e^{p_i^+ k x}}{k (\cos b_i a) [\kappa + a(\kappa^2 + b_i^2)] \left(\frac{R_{MF}}{2} - p_i^+ \right) (p_i^+ + j)} \text{ for } x < 0$$

(220)

and

$$\underline{A_f}(x,y) = \frac{\mu_f N i \cosh \gamma(-j) k y e^{-j k x}}{k (\gamma(-j) \sinh \gamma(-j) a + \kappa \cosh \gamma(-j) a)} + \sum_{i=0}^{\infty} \frac{\mu_f N i b_i^2 \cos b_i k y e^{p_i^- k x}}{k (\cos b_i a) [\kappa + a(\kappa^2 + b_i^2)] \left(\frac{R_{MF}}{2} - p_i^- \right) (p_i^- + j)} \text{ for } x > 0.$$

(221)

Because of the nonideal core both the excitation and perturbation fields are reduced. The relative end effect may be decreased due to the faster decay of the perturbation field, but a numerical check of this remains to be evaluated.

The impedance for a coil one wavelength long, calculated as before, is

$$\frac{Z}{R_0} = \frac{R_e}{R_0} + \frac{j}{\gamma(-j) \tanh \gamma(-j) a + \kappa} + \sum_{i=0}^{\infty} \left\{ \frac{j b_i^2 (e^{2\pi p_i^-} - 1) \left[\frac{e^{(p_i^- + j) k x}}{(p_i^- + j)} \pm \frac{e^{(p_i^- - j) k x}}{(p_i^- - j)} \right]}{2\pi [\kappa + a(\kappa^2 + b_i^2)] \left(\frac{R_{MF}}{2} - p_i^- \right) (p_i^- + j)} \right\}$$

(222)

where the terms are as described with Eq. 214 for the ideal core.

The calculation of the arbitrary core powers is much more complicated. There is no longer an orthogonality condition for P_m , the integral of the product of the fields for two different values of i is not zero; and there is complete cross-coupling, including to the excitation field and between entrance and exit fields. This is also true for P_s since neither the perturbation electric field nor the longitudinal perturbation magnetic field are zero at the coils. The $i = 0$ fields may not dominate the calculations as in the ideal-core machine, necessitating the retention of more terms. Finally, the power carried by the fields in the core has to be considered. There will be electrical power transferred through the core to the coils from outside the machine, regions 1 and 4, because there

is a similar x-directed power flow in the core as in the fluid, although it should be small. The lossless core machine of arbitrary permeability is not carried further here, because of these computational difficulties.

6.6 EXTENSIONS

Before leaving the machine of finite length, it is worthwhile to consider some of the possible extensions of the theory to cover other models. The case of a core with loss presents additional difficulties because the roots of Eq. 204 are not purely imaginary. One method of finding the roots would be to use an expansion about the poles for $\kappa = 0$, valid for $\kappa \delta \ll 1$. This is of limited value, and appears to be harder than a direct iterative solution. The rest of the procedure for finding the fields and powers would be the same, and could be carried through once the roots are known. An iron core is always laminated in practice, and this is equivalent to making the core lossless, $\delta \approx 1$, so that the lossless-core solution covers almost all cases of interest.

For a core of arbitrary length the transform approach cannot be applied. The procedure of finding the normal modes and then matching the boundary conditions requires a continuum of modes because of the infinite lengths. One possibility, valid for the field solution with no fluid present, is to use a spatial transformation to map the finite-length core into the previous problem. This area merits investigation, but does not appear fruitful for design purposes. The finite-length core probably has little effect at the entrance because the fields outside the machine, region 1, are small. It will be important at the exit, but the exit powers are small.

Turning next to the exciting current, the actual coil structure will not start and stop abruptly; there will be gaps due to the missing coils which would extend outside the machine. These gaps will result in a still lower power density at the ends, less exciting field there, and an increase in the net end effect. This can be included analytically by using the transform of the actual current distribution. It will change the residues, but not the natural poles, and add additional poles. The basic procedure remains the same.

Finally, there is the possibility of diminishing the end disturbance by grading the exciting winding. If \vec{K} has a zero corresponding to the p_0^- pole, this pole will not appear in the fields, and the perturbation will be appreciably reduced. In practice it may not be possible to completely cancel this pole, although a substantial reduction may be obtained. This result is particularly important for the case of a short machine. Qualitatively, the exciting winding would have to extend out past the previously sharp machine ends, so that the improvement is paid for with increased viscous and excitation losses. Further analysis is required to see if this results in an overall improvement.

VII. DISCUSSION OF GENERATOR PERFORMANCE

Consideration will now be given to the MHD induction machine in terms of attainable over-all efficiencies. Weight and cost considerations are not included. Attention is accordingly directed toward the generator case, as efficiency is a primary determining factor in selecting a generating system. The selection of a pumping system is not necessarily based on efficiency considerations, as the absence of rotating components and seals are important advantages. Also, power levels are substantially lower than those proposed for MHD power generation systems, particularly in central-station installation.

A clear statement of the model used is included in section 7.1 so that the usefulness of the results obtained may be assessed. A study of the basic interaction process in section 7.2 shows the parameter range required for reasonable operation, and this is used in section 7.3 to examine liquid metals and slightly ionized plasmas as working fluids in the induction generator. Performance calculations for a high and a medium-power generator operated on a liquid-metal flow are carried out in sections 7.4 and 7.5 based on realistic fluid and electrical conditions. They are selected to show the performance to be expected and the limitations placed on the parameter values.

7.1 THE MODEL

The previous theory started with the basic field-fluid interaction which gives the upper limit of attainable machine performance. To it were added the following.

1. Loss in the exciting system - coil, core, capacitors
2. Velocity profiles
3. Viscous loss
4. Finite machine length
5. Channel walls and insulation.

Not included were the following.

1. Details of the excitation system
2. Finite machine width
3. Gas-dynamic considerations, including compressibility and Hall effect
4. The fluid power source.

The exciting system losses are approximate, as exact values cannot be obtained until the detailed construction of the winding and core is specified. Slots, cooling, etc., are accordingly not considered in detail, but reasonable figures for coil, core, and capacitor losses (required for power-factor correction) are calculated.*

* Superconducting windings are not considered because of AC power dissipation. Cryogenic coils may be better. The coil loss is already small, and the construction problems associated with the cooling system will result in a greatly increased air gap, so that neither system appears attractive.

The channel walls and insulation, treated in Appendix G, may be highly detrimental to generator operation. Since a proper design must avoid this, they are accordingly not considered here.

The chief assumption is to neglect the finite machine width because the fluid current paths must be closed at the edges of the machine. The finite width will have little effect on machine performance if the additional resistance introduced into the current path is small compared to the resistance across the machine. This is satisfied by making the machine wide, $c \gg \lambda$, and/or by adding highly conducting copper bars along the edges of the channel. Otherwise the fluid current and the power density will be decreased by the increased path resistance, resulting in a lower efficiency. An annular geometry avoids this difficulty, but adds others in the construction and cooling of the inner core.

The induction generator, in principle, may be used in both open- and closed-cycle power systems. In the former, combustion gases serve as the working fluid,⁶⁷ in the latter, either a plasma⁶⁸ or a liquid metal^{69, 70} may be used. It is shown in section 7.3 that the plasma conductivity attainable within the limits imposed by heat-source temperatures is too low for reasonable power factors and power densities. Further discussion, accordingly, is limited to liquid-metal generators, and plasma problems such as compressibility and Hall effect are not treated.

7.2 OPTIMUM OPERATING REGIME

The conditions required to attain an efficiency of over 70% for the generator and associated equipment are reviewed. The limiting electrical efficiency, $\frac{1}{1-s}$, must be much higher to allow for other losses. This constrains s to lie in the range $-\frac{1}{4} < s < 0$, but it should not be too close to zero to avoid excessive profile and end losses.

The circulating power should be small compared with the real power for small excitation and capacitive losses, and this requires R_M to be on the order of 10. Low $|sR_M|$ values lead to less output power for the same excitation losses, and accordingly to lower efficiency. A further consideration is that $|sR_M|$ should be of the order of or greater than unity to attain a power density of the same value as the corresponding DC machine. This criterion cannot always be satisfied, as R_M is limited by attainable fluid properties, but the total efficiency decreases, and the entry length increases for a finite-length machine, as R_M becomes smaller.

The value of α should be small (0.1 or less) to keep the power density high. It is limited by the minimum value of the channel half-width set by construction problems.

For an air-core machine, R_M is replaced by $R_{M\alpha}$ as shown in Eq. 53, and the power density is decreased for the same exciting current because of the increased reluctance of the magnetic circuit. For $\alpha = 0.1$, $R_{M\alpha} \ll R_M$, and the power level, Eq. 71, is less than a tenth of its iron-core value. As the iron-core generator must be carefully designed to yield an only marginally acceptable efficiency, the air-core machine is inherently not capable of meeting the required performance, and will accordingly not be considered here. It may be of interest only when weight or temperature limitations rule out iron.

The velocity profile for a slit-channel machine may significantly decrease the efficiency for small s , as is shown in Fig. 30 for a Hartmann profile. For laminar flow and s around -0.1 , M must be much greater than 50 to prevent a 5 or 10% decrease in the efficiency. This condition is automatically satisfied for a high power density. For turbulent flow the boundary-layer analysis shows that $\frac{\delta}{a}^*$ is increased, so that a slight loss in the efficiency is encountered even for M in the range 500-1000. The non-slit-channel machine is not considered here because of its low power level and severe profile effects.

Finally, the dimensions of the machine are restricted by end and edge considerations. The machine must be several wavelengths long so that the finite length does not decrease the power level. A decrease in the power level represents a decrease in the over-all efficiency because less output power is obtained for the same viscous and excitation losses. The machine width should be larger than λ to keep edge losses small. The wavelength cannot be too small, or $\alpha \leq 0.1$ cannot be satisfied.

7.3 COMPARISON OF LIQUID METALS AND PLASMAS

The primary consideration for a fluid in the MHD induction generator is the attainable magnetic Reynolds number. Based on R_M , a quick evaluation of a given fluid is possible before adding in the other loss mechanisms. Since v and v_s are approximately the same for small s ,

$$R_{MF} = \frac{\mu \sigma v \lambda}{2\pi} \tag{223}$$

is used in place of R_M .

Practical values for a liquid metal and a plasma are listed in Table 15. The σv product for a liquid metal is large due to the high conductivity, and reasonable values of R_{MF} are obtained. The velocity is limited by viscous losses and λ by the total machine length. For a plasma the σv product is too low by more than two orders of magnitude. Unless higher conductivities are obtainable, a plasma is not suitable as a working fluid in the MHD induction machine. It may be noted that, even for a liquid metal, there is no leeway for the decrease in going from R_M to $R_{M\alpha}$ for an air-core machine.

Table 15. Liquid metal and plasma properties.

	Liquid Metal	Plasma
σ , mhos/m	10^6	10^2
v , m/sec	10-100	10^3
λ , m	1	1
$R_{MF} = \frac{\mu \sigma v \lambda}{2\pi}$	2-20	0.02

7.4 HIGH-POWER GENERATOR

A design for a generator producing an output power in the 100-megawatt range is discussed. This is not intended to be an optimum design, and is not chosen to meet any specifications, but it does give an idea of attainable efficiencies and the limits on machine parameters. The results are summarized in Table 16, where all numbers were rounded to three figures after the calculations.

Eutectic sodium-potassium (NaK), 78% potassium by weight, is chosen for the fluid. The fluid used for an actual machine will depend on thermodynamic considerations, which are not considered here. The fluid temperature will be high because of the heat source and losses. The properties⁷¹ of NaK at 700°C are

$$\begin{aligned}\sigma &= 1.1 \times 10^6 \text{ mhos/m,} \\ \eta &= 1.5 \times 10^{-4} \text{ kg/m-sec,} \\ \rho &= 7.1 \times 10^2 \text{ kg/m}^3 .\end{aligned}$$

The dimensionless parameters are chosen to be $s = -0.1$ for a high limiting efficiency, $R_M = 10$ so that $|sR_M| = 1$, and $\alpha = 0.1$ for a high power density. For an iron-core machine κ will be small, and is taken to be zero except when finding the core loss. The magnetic Reynolds number cannot be increased without increasing the relative viscous loss, as explained later. Making $|s|$ smaller runs into three difficulties: the power density drops because R_M is fixed, the profile losses become larger, and the penetration length of the field increases. The ratio α cannot be decreased because the gap between the exciting plates is already less than 1% of the length or width of the plates, and this makes construction difficult. This choice of machine parameters, dictated by the nature of the interaction, automatically leads to a high-power machine. It is necessary to move away from this optimum to lower the power level, and the result is a lower efficiency. Thus, the induction generator is inherently a high-power machine, if constrained to have a high power factor.

Since the choice of machine parameters is inter-related, only the frequency or wavelength, c , and NI remain. For example,

$$v_s = \frac{\omega}{2\pi} \lambda , \quad (224)$$

and, for NaK,

$$R_M = 0.22 \frac{\omega}{2\pi} \lambda^2 . \quad (225)$$

For a central power station, $\frac{\omega}{2\pi}$ will be 60 cps, giving 0.871 m and 52.3 m/sec, respectively, for λ and v_s . Increasing $\frac{\omega}{2\pi}$ while holding either R_M or λ constant

increases v_s , and makes the performance worse because the viscous loss increases faster than the output power. Increasing R_M without increasing v_s is desirable but leads to lower frequencies. Increasing $\frac{\omega}{2\pi}$ and holding v_s constant, necessary for a 400 cps space power system, has the disadvantage of reducing R_M . These considerations may rule out higher frequencies at high power factors. For the remaining dimensions, the machine is made 10 wavelengths long and 2 m wide to minimize end and edge effects. Note that a , 1.59 cm, is very small compared with both $n\lambda$ and c .

The final parameter, NI , should be large for a high power level, but not so large that the iron saturates. Choosing $NI = 10^5$ amp-turns/m, and operating the winding at a current density of 10^4 amps/in² (1550 amps/cm²), determines the exciting-winding thickness b to be 0.645 cm. This is not small compared to a , but putting the winding in slots avoids the decrease in power level due to the finite-thickness winding which occurred in Appendix C. The magnitude of the flux density, 0.889 wb/m², is low enough so that the iron teeth between the slots where the coils are located should not saturate.

At this point the limiting efficiency, including profile and end effects, is calculated before the other losses are added. First, $R_e = 1.49 \times 10^7$, so that the flow will probably be turbulent. For this R_e and $M = 747$, $\frac{\delta^*}{a} = 7 \times 10^{-3}$ from the turbulent boundary-layer theory of section 5.5. Comparing this with $\frac{\delta^*}{a} = \frac{1}{M}$ for a Hartmann profile gives an effective M of 143 for the turbulent profile. This agrees with the work of Harris for turbulent MHD flows (section 5.2), which required a higher M for the same flatness as the Hartmann profile. Using the effective M to calculate the profile factor gives $F_m = 1.038$.

Finite length is included by means of the ratios of P_s and P_m for finite-to-infinite length machines. The values of 0.827 and 0.842, respectively, are obtained for these parameters. The efficiency is decreased, since the ratio is less for P_s than P_m , and the over-all efficiency is further decreased because the power output is less for the same viscous and coil losses. The end and profile factors are independent for a slit channel. Using Eq. 71 for P_s together with the profile and finite-length factors gives an output electrical power of 47.3 megawatts, an input mechanical power of 55 megawatts, and an efficiency of 86% without inclusion of the other losses.

The coil, capacitor, core, and viscous losses must still be taken into account. The coil loss is calculated from the conductor volume and the conductivity, Eq. 33. For the assumed NI and current density, and using copper at 200°C, $P_e = 0.80$ megawatt. A temperature of 200°C is selected because the coils and core must be considerably cooler than the fluid so that the magnetic properties of the core are retained.

Capacitors are required for power-factor correction with the induction generator. This might be supplied by conventional synchronous generators in a large system, but allowance is made here on the basis of the loss attributable to the static capacitors for a self-contained system. The power loss is determined by the Q of the capacitors plus the associated lead loss. For conventional power-system capacitors, the best

obtainable, at present, is a Q of around 300 at 60 cps.⁷² A total Q of 50 is assumed to include losses in the leads plus the additional capacitance required to balance the normally inductive generator load. The capacitor power loss is 0.95 megawatt, since the real and reactive powers are equal for $|sR_M| = 1$. An increased Q will cause at most a 2% increase in efficiency.

The core loss depends on the core construction. A solid core is not acceptable, and a laminated core must be used as in conventional machinery to reduce the circulating currents and loss. This is equivalent to decreasing σ_c and δ while retaining κ small. The core loss is found as a function of the field strength and the lamination thickness from experimental measurements of the power loss per pound, including both I^2R and hysteresis losses. For calculation purposes, the magnetic flux density in the core is assumed to be constant for a skin depth and zero elsewhere, in the manner used to calculate the power loss in conductors with skin depth.⁷³ Since δ is now on the order of 1, the skin depth, $\frac{1}{\text{Re}\{\delta k\}}$, is 0.139 m. For a high-grade transformer steel at $B = 0.889 \text{ wb/m}^2$, the power loss is 0.41 watts per pound for 0.014 inch thick laminations.* The density is 7.55 gr/cm^3 , so that a volume of steel $2(0.139 \times 10 \lambda \times c)$ cubic meters weights 80,600 lbs. The approximate core loss, 0.033 megawatts, is negligible compared to the other powers. Evidently, the effective σ_c is essentially zero.

Finally, the viscous loss in terms of the friction factor is

$$P_v = \frac{f l \rho v^2 (2 a c v)}{2 D_h} \quad (226)$$

from Eq. D.19 for the viscous pressure drop. This may be high by a factor 2, as mentioned in Appendix D. For $R_e = 1.49 \times 10^7$ and $M = 747$, $f = 7.6 \times 10^{-3}$ for OHD turbulent flow, or 8.5×10^{-3} from the MHD turbulent boundary-layer analysis. The results are close, so that, since P_v is in question by a factor 1/2, it makes little difference which is used. Taking the OHD value of f , and neglecting the factor 1/2, $P_v = 4.47$ megawatts. This is 10% of the output power, and is the largest of the losses. Note that P_v is proportional to v^3 , while P_g is proportional to v with constant R_M , so that increasing v will make the net performance worse.

Based on these approximate results for the losses, the total power output is 45.6 megawatts, and the efficiency is 77%. This may be slightly low compared with other generating methods, but may be advantageous in allowing a higher heat-source temperature than conventional turbine systems.

The three other high-power designs of Table 16 show the increased efficiency resulting from increasing the length and NI . Only the changed figures are entered in the table. Doubling the length, design 2, increases the ratios of P_g and P_m for finite-

* Armco tran-Cor A-6.⁷⁴

to-infinite length machines to 0.913 and 0.920. This gives a slightly higher power level relative to the losses and better efficiency.

In designs 3 and 4, NI is increased by 2, which doubles the power level. This decreases the profile factor F_m to 1.022, since $\frac{\delta^*}{a} = 4.02 \times 10^{-3}$, and the effective M is 249. The efficiency is higher because the power output is increased for the same viscous loss (neglecting any change in f), and because F_m is smaller. Note that P_e varies linearly with NI , while P_s and P_m vary as the square, because of the assumed constant current density. Ideally, NI should be further increased, but this is not practical because of saturation. Already $B = 1.26 \text{ wb/m}^2$, which may be too large for the teeth. Evidently, the generator should be operated at maximum magnetic field for highest efficiency.

To complete the calculations, the total pressure difference across the machine and the coil resistance are found for the first design. The pressure difference, $P_{in}/(2acv)$, is 2699 psi or 184 atmospheres, including the viscous pressure drop. This is large but not excessive for the powers considered. It could be decreased by departing from the uniform-channel generator. If the width increases along the machine, the velocity drops and some of the dynamic head of the flow may be utilized.

To estimate the negative coil resistance due to the power transfer, neglecting the finite coil conductivity, requires a better picture of the winding. As a minimum value (i. e., minimum N), consider the coil to be made of square turns of dimensions $b \times b$, where $b = 0.645 \text{ cm}$. Then the turns density, $\frac{1}{N}$, is 155 turns/m, and $I = 645 \text{ amps}$. The series resistance per phase per wavelength, from Eq. 51, is $R_s = -13.7 \text{ ohms}$, and the coil terminal voltage is 8.8 kilovolts. This does not include the effects of finite length or the velocity profile, which decrease R_s and V and cause them to vary along the machine. If these effects are included, the average values along the machine, calculated from P_s , are -11.4 ohms and 7.4 kilovolts. V and R_s can be cut in half by connecting the top and bottom exciting coils in parallel instead of in series. The current can be decreased by increasing N , but it may be best to keep the voltage in the machine low and then use an external transformer. The machine is itself a variable-ratio transformer since N can be adjusted in the design.

7.5 MEDIUM-POWER GENERATOR

A slightly different procedure is used for a generator with an output power around one megawatt because operation at the optimum point is no longer possible. Instead, certain dimensions, set by the reduced volume, and the magnetic field are specified. It was shown in the previous section that operation at the highest possible magnetic field, limited only by core saturation, is best because the power output increases faster than the losses. The magnitude of the field is specified as 1 wb/m^2 , probably large enough for saturation in the teeth.

The generator volume is reduced to produce a more compact machine and to reduce the viscous and excitation losses along with the output power. The minimum wavelength is limited to around $1/3 \text{ m}$ by construction difficulties at these power levels

Table 16. High-power generator designs.

Parameters	Units	1	2	3	4
s		-0.1			
R_M		10			
α		0.1			
κ		0			
$\omega/2\pi$	cps	60			
v_s	m/sec	52.3			
v	m/sec	57.5			
a	m	0.0139			
c	m	2			
λ	m	0.871			
k	1/m	7.21			
ℓ	m	8.71	17.4	8.71	17.4
R_e		1.49×10^7			
NI	amp-turns/m	10^5		$\sqrt{2} \times 10^5$	
b	m	0.00645		0.00912	
B	wb/m ²	0.889		1.26	
M		747		1060	
P_s	megawatts	47.3	105.	94.6	209.
P_m	megawatts	55.0	120.	108.	237.
e_g - Limit	%	86.0	86.9	87.3	88.2
P_e	megawatts	0.80	1.60	1.13	2.26
P_{cap}	megawatts	0.95	2.09	1.89	4.18
P_{core}	megawatts	-	-	-	-
P_v	megawatts	4.47	8.94	4.47	8.94
P_{out}	megawatts	45.6	101.	91.6	203.
P_{in}	megawatts	59.5	129.	113.	246.
e_g - Total	%	76.6	78.0	81.2	82.4
Δp	psi	2699	5860	5120	11200

and to keep R_M reasonably large. Here, λ and c are chosen as $\frac{1}{2}$ m each, and the machine length as 4 wavelengths. This leads to increased end and edge effects, but appears to be unavoidable. The values $\alpha = 0.1$ and $\frac{\omega}{2\pi} = 60$ cps are again used, and NaK is retained as the fluid. Higher frequencies may give poorer results, as mentioned. For this design $v_s = 30$ m/sec, $R_M = 3.3$, and $M = 482$.

The only unspecified parameter is s . Three designs showing the effect of varying s at constant magnetic field are given in Table 17. The exciting current is increased with increasing $|s|$ to hold B constant, because of the larger reaction field, as mentioned in sections 3.2 and 3.3. For this case, P_s is found from Eq. 73 for a constant

Table 17. Medium-power generator designs.

Parameter	Units	1	2	3
s		-0.1	-0.2	-0.3
R_M		3.3		
α		0.1		
κ		0		
$\omega/2\pi$	cps	60		
v_s	m/sec	30		
v	m/sec	33	36	39
a	m	0.00796		
c	m	0.5		
λ	m	0.5		
k	1/m	12.6		
ℓ	m	2		
R_e		4.82×10^6	5.25×10^6	5.69×10^6
NI	amp-turns/m	0.838×10^5	0.953×10^5	1.12×10^5
b	m	0.00541	0.00615	0.00723
$ B $	wb/m ²	1		
M		482		
P_s	megawatts	0.429	1.17	1.97
P_m	megawatts	0.592	1.53	2.71
$e_g - \text{Limit}$	%	72.5	76.1	72.7
P_e	megawatts	0.038	0.044	0.051
P_{cap}	megawatts	0.0086	0.023	0.039
P_{core}	megawatts	-	-	-
P_v	megawatts	0.059	0.075	0.095
P_{out}	megawatts	0.38	1.10	1.88
P_{in}	megawatts	0.65	1.61	2.80
$e_g - \text{Total}$	%	58.7	68.4	67.1
Δp	psi	359	814	1310

magnetic field, but otherwise the calculations proceed as before. The ratios of P_s and P_m for finite-to-infinite-length machines and the profile factors F_m are listed in Table 18 for $s = -0.1$, -0.2 , and -0.3 . The efficiency before adding the other losses goes through a peak around $s = -0.2$. This is due primarily to the finite-length effect, which increases with smaller $|s|$. F_m also increases, but not as rapidly until $|s|$ becomes still smaller. This shows the limitation on s and the efficiency; the efficiency cannot be made arbitrarily large as in the ideal model.

Table 18. End and profile factors, and friction factors for medium-power generators.

	Factor	$s = -0.1$	-0.2	-0.3
End	P_s	0.5451	0.7404	0.8333
	P_m	0.6564	0.7925	0.8667
Profile	$\frac{\delta^*}{a}$	0.00722	0.00762	0.00799
	F_m	1.040	1.023	1.017
Friction	OHD	0.009	0.0088	0.0087
	MHD	0.012	0.0108	0.0106

The power dissipations in the exciting winding, capacitors, and fluid are calculated as in section 7.4, and the core loss is assumed to be negligible. The OHD turbulent and MHD turbulent boundary-layer friction factors are listed in Table 18. The value of P_v is less than 10% of P_m , and the percentage decreases with increasing $|s|$.

The total efficiency is lowest for $s = -0.1$ and climbs to a more reasonable figure with increasing $|s|$. There is a peak, probably around $s = -0.24$. The peak total efficiency occurs at a higher slip than the peak limiting efficiency because the additional losses do not increase as fast as the electromagnetic powers. The efficiencies, both limiting and total, are less than those for the high-power machine, because of the lower R_M and increased end losses. For small R_M the end effect for a short machine increases; thus a short machine with high efficiency may not be possible without compensation to reduce the end losses. This rules out decreasing λ because the increased number of wavelengths in the machine is at least partially offset by the smaller R_M and increased end effect.

VIII. CONCLUDING REMARKS AND SUGGESTIONS FOR FURTHER STUDY

8.1 CONCLUDING REMARKS

The objective of this investigation was to provide a clear picture of the terminal properties of and power flow in the MHD induction machine. The previous theory has been extended to include velocity profiles and finite machine length, the results have been carefully interpreted both physically and numerically, and an attempt has been made to clear up existing misconceptions regarding MHD induction machines. The emphasis has been on generator properties and design because pump performance is less critical. Also, it is easier to build and study the operation of experimental pumps in the kilowatt power range than experimental generators in the megawatt power range.

The theory of the fluid-field interaction, including viscosity and ends, gives a definite limited range for the dimensionless parameters s , R_M , α , κ , and M where machine operation appears attractive. This leads to restrictions on the fluid properties which eliminate plasmas from further consideration. Liquid metals look practical for power generation, but additional study, including experiments, is required before a final assessment can be made.

The numerical study of Section VII gives an idea of attainable performance based on several representative but nonoptimum calculations. Efficiencies of around 80% were obtained for a high-power machine, which is an encouraging result for an initial investigation. For a medium-power machine the efficiencies were over 10% lower, and this is, at best, marginally satisfactory for space-vehicle applications. At lower power levels, the induction generator does not appear to be acceptable. It may not be possible to make the dimensions small and still keep R_M sufficiently large.

8.2 THEORETICAL EXTENSIONS

It is necessary to consider finite width before proceeding further because it could make the linear induction generator impractical if the effect on the efficiency is larger than expected. This may be avoided by using an annular geometry, but this introduces flow and cooling problems. Finite machine width has been treated elsewhere,⁷⁵ but a better model is needed. In an actual machine, the coils will probably extend past the edges of the channel to make full use of the fluid with only a slight increase in the already small coil loss. Thus, the model should consist of a fluid of finite width flowing between exciting plates with z -independent currents. The reaction field depends on z , but the applied field is independent of the z -coordinate.

More attention must be paid to the constructional details of the exciting system, probably by using the empirical methods developed for rotating machinery. Methods of eliminating the channel wall, which was shown to be highly detrimental to the operation, will also have to be considered.

Concurrently, the preliminary analysis of Section VII should be developed into a proper design procedure. Except for the lack of better information about the fluid behavior and the lack of experimental results, the necessary information is available for this purpose. It is possible to write one complete program to perform all of the analysis, but this has not yet been done.

There is still much room for theoretical investigations of the fluid behavior, but the next phase of the study of liquid-metal flows is primarily experimental in character. The turbulent boundary-layer analysis can be extended when experimental MHD profiles are available, and the empirical and random-theory methods of analysis may be useful (see Harris⁵³ and Poduska⁷⁶). The whole area of compressible fluids and plasmas has been neglected here as not of interest for a practical machine, but it is an interesting and complex theoretical problem.

8.3 EXPERIMENTAL EXTENSIONS

There is a pressing need for more experimental investigation of both DC and induction-coupled turbulent MHD flows. There is no available information on the velocity profiles needed for machine evaluation, and the few friction-factor measurements available at present are not sufficient by themselves to separate out viscous and circulating-current I^2R contributions. Measurements at the larger values of R_e and M envisioned for a practical machine are non-existent. The turbulent boundary-layer analysis should be checked experimentally to see if the OHD and MHD friction factors cross, and the theory should be redone using the experimental MHD velocity profile. Measurements of the location of the laminar-to-turbulent transition for induction-coupled flows are also needed. This will be more complicated than in the DC case, and will probably depend on α and ω in addition to R_e and M . The lack of better fluid information makes design difficult because viscous losses and profile effects are two of the biggest and least well-known losses in the machine.

An experimental induction machine is presently being tested by Porter²⁸ to evaluate the theoretical work. Additional well-designed test models will be necessary for further comparison before any consideration is given to the possibility of constructing a full-scale power-generation system.

APPENDIX A

Continuity of the Tangential Electric Field in MHD Machines

In the analysis of some models for an MHD machine it is possible to obtain a discontinuity in the tangential electric field across a boundary. This apparent violation of Maxwell's equations is due to the use of a model where current would normally flow across a boundary, but is constrained not to by conditions specified in the problem statement; for example, between two materials of different electrical conductivity in direct contact. This situation occurs in the MHD induction machine without the thin insulating strips to prevent current in the y-direction. The addition of the insulating strips, required by the problem statement, explains the source of the discontinuity. As the thickness of a strip approaches zero, it is found to support a tapered dipole charge layer (double layer) across which, as shown by Stratton,⁷⁷ there is a discontinuity in the tangential electric field of

$$\vec{E}_+ - \vec{E}_- = -\frac{1}{\epsilon_0} \nabla \tau, \quad (\text{A.1})$$

which is equivalent to the discontinuity

$$\phi_+ - \phi_- = \tau / \epsilon_0 \quad (\text{A.2})$$

in the scalar potential. Here, \vec{E}_+ is the electric field on the positive side of the dipole layer, and τ is the dipole surface density. The normal electric field is continuous across a dipole layer.

Another view of the source of the discontinuity is provided by the mathematical approach used in MHD. The fields are determined from Maxwell's equations without the equation for $\nabla \cdot \vec{E}$, to be consistent with neglecting displacement currents. The volume charge density is zero; but surface charges, or dipole layers in the limit of thin strips, may be required to satisfy the boundary conditions. The difficulty is not that the solution is incorrect, but that it is incomplete because the required charge densities have not been included. The insulator is needed on the boundary to prevent current flow across it and to support the dipole layer.

As an example, consider the MHD induction machine with a constant fluid velocity. The model to be analyzed, Fig. A-1, differs from that of Chapter 3 in replacing the thin insulating and exciting strips by sheets of finite thickness to avoid discontinuities in the fields. The excitation becomes a current density,

$$\vec{J}_e = \vec{i}_z \frac{NI}{b} \cos(\omega t - kx), \quad (\text{A.3})$$

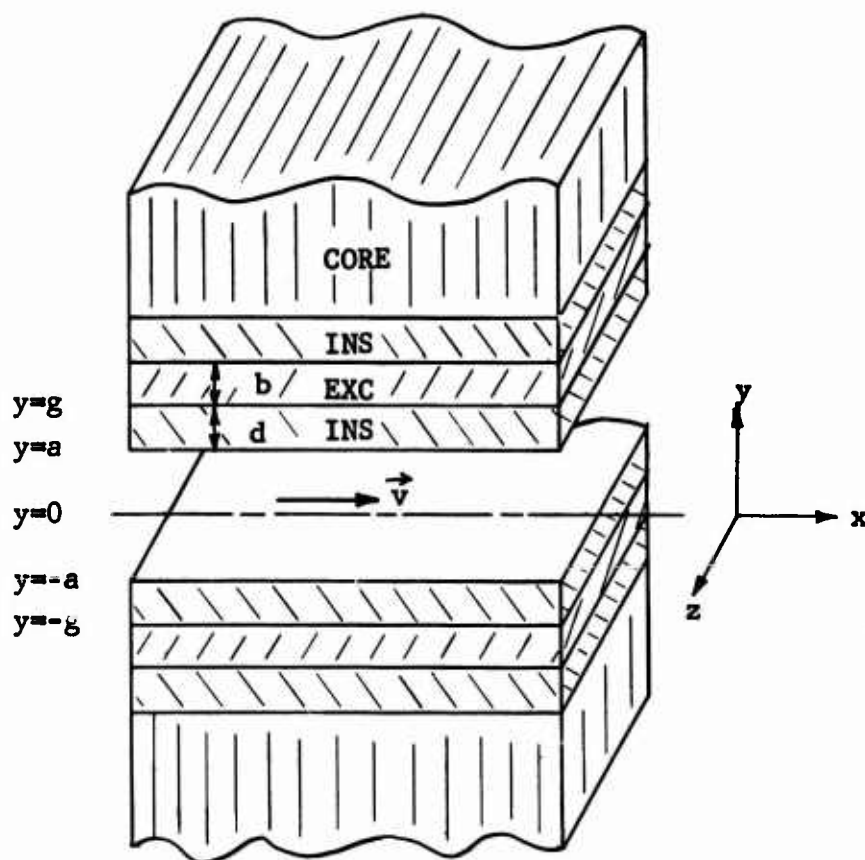


Fig. A-1. The Model

where b is the exciting-layer thickness. For simplicity the fluid, insulators, and exciting sheets are assumed to have the same permeability μ_0 .

It is not necessary to obtain the complete electromagnetic field solution with all the arbitrary constants. Attention is confined to the fluid, the exciting sheets, and the pair of insulators separating them. This part of the total solution is determined in terms of the magnetic field at the center of the channel, and then the limit taken as the insulator thickness d approaches zero to show the discontinuity in the tangential electric field across the insulator and the dipole layer on the insulator. This demonstrates the source of the discontinuity but reduces the mathematical complexity. A similar discontinuity also exists across the outer pair of insulators.

The fields are determined from Eqs. 8-11. Equation 11 is required in the insulators because Eq. 8 does not constrain ϕ to be zero. The equations are linear, so that all variables must possess the same $e^{j(\omega t - kx)}$ dependence as the excitation. Again the complex amplitudes are used, and the vector potential and current are in the z -direction and independent of z . The solution retaining all three components of the vector potential, analogous to the case treated in Appendix B, does not change the conclusions.

The potentials in the fluid and insulators are:

$$\underline{A}_f = \underline{A}_{f1} \cosh \gamma ky, \quad (\text{A.4})$$

$$\underline{\phi}_f = 0, \quad (\text{A.5})$$

$$\underline{A}_i = \underline{A}_{i1} \cosh ky + \underline{A}_{i2} \sinh ky, \quad (\text{A.6})$$

and

$$\underline{\phi}_i = (\underline{\phi}_{i1} z + \underline{\phi}_{i3}) \cosh ky + (\underline{\phi}_{i2} z + \underline{\phi}_{i4}) \sinh ky. \quad (\text{A.7})$$

The symmetric excitation forces \underline{A}_f to be symmetric. The form of the coefficients for $\underline{\phi}_i$ is chosen because any measurable quantity must either be independent of or linear in z due to the infinite length in the z -direction. The fields represented by these potentials are obtained from Eqs. 6 and 7.

In the exciting sheets the current is constrained by the source. The vector potential, a function of y for the finite thickness, is found either from

$$\nabla^2 \underline{A}_e = - \frac{\mu_o NI}{b}, \quad (\text{A.8})$$

or by combining Eqs. 5a and 5b to obtain

$$-jk \underline{B}_{ey} - \frac{1}{jk} \frac{\partial^2 \underline{B}_{ey}}{\partial y^2} = \frac{\mu_o NI}{b}. \quad (\text{A.9})$$

The result is

$$\underline{A}_e = \frac{\mu_o NI}{k^2 b} + \underline{A}_{e1} \cosh ky + \underline{A}_{e2} \sinh ky. \quad (\text{A.10})$$

The z -component of the electric field is constrained to be

$$\underline{E}_{ez} = \frac{NI}{\sigma_e b} \quad (\text{A.11})$$

by the current source, which is assumed to be located at infinity rather than distributed in the winding as in section 2.3. The scalar potential, using Eq. 7, is

$$\underline{\phi}_e = \frac{NI}{\sigma_e b} z \left(1 + \frac{j \mu_o \sigma_e v_s}{k}\right) - j\omega z (\underline{A}_{e1} \cosh ky + \underline{A}_{e2} \sinh ky). \quad (\text{A.12})$$

The complex coefficients are calculated from the boundary conditions on the electric and magnetic fields in terms of \underline{A}_{f1} , the magnetic field at the center of the channel, which remains finite. \underline{A}_{f1} could be determined in terms of the excitation and machine parameters, but only with considerable difficulty. At $y = a$ and $y = g$ both components of the magnetic field and the tangential electric field are continuous. From these conditions,

$$\underline{A}_{i1} = F_1 \underline{A}_{f1}, \quad (\text{A.13})$$

$$\underline{A}_{i2} = F_2 \underline{A}_{f1}, \quad (\text{A.14})$$

$$\underline{\phi}_{i1} = \frac{\frac{-NI}{\sigma_e b} - j\omega \underline{A}_{f1} (F_1 \cosh kg + F_2 \sinh kg)}{\cosh kg - \coth \alpha \sinh kg}, \quad (\text{A.15})$$

$$\underline{\phi}_{i2} = -\underline{\phi}_{i1} \coth \alpha, \quad (\text{A.16})$$

$$\underline{A}_{e1} = F_1 \underline{A}_{f1} - \frac{\mu_0 NI}{k^2 b} \cosh kg, \quad (\text{A.17})$$

$$\underline{A}_{e2} = F_2 \underline{A}_{f1} + \frac{\mu_0 NI}{k^2 b} \sinh kg, \quad (\text{A.18})$$

and $\underline{\phi}_{i3}$ and $\underline{\phi}_{i4}$ are zero; where

$$F_1 = \cosh \gamma \alpha \cosh \alpha - \gamma \sinh \gamma \alpha \sinh \alpha, \quad (\text{A.19})$$

and

$$F_2 = \gamma \sinh \gamma \alpha \cosh \alpha - \cosh \gamma \alpha \sinh \alpha, \quad (\text{A.20})$$

are independent of the insulating-strip thickness d .

The change in the z component of the electric field across the insulator,

$$\underline{\Delta E}_z = \underline{E}_z(g) - \underline{E}_z(a) = \frac{NI}{\sigma_e b} + j\omega \underline{A}_{f1} \cosh \gamma \alpha, \quad (\text{A.21})$$

is independent of d except for the variation of \underline{A}_{f1} . The discontinuity remains in the limit as d becomes zero, provided that the insulator is not removed, so that the tangential electric field can be discontinuous across an insulating strip of infinitesimal thickness. There is a similar discontinuity in the x component of the electric field.

Further insight is obtained by examination of the fields inside the insulator and the surface charge densities on the insulator as functions of d . For small d , $kd \ll 1$, the electric field is approximately

$$\begin{aligned} \underline{\underline{E}}_i = \underline{\underline{\phi}}_{i1} \frac{k}{\sinh \alpha} [-\underline{\underline{i}}_x jk(y-a)z + \underline{\underline{i}}_y z + \underline{\underline{i}}_z (y=a)] \\ -\underline{\underline{i}}_z j\omega \underline{\underline{A}}_{f1} (F_1 \cosh ky + F_2 \sinh ky), \end{aligned} \quad (\text{A.22})$$

where

$$\underline{\underline{\phi}}_{i1} = \frac{\sinh \alpha}{kd} [NI/\sigma_e b + j\omega \underline{\underline{A}}_{f1} (\cosh \gamma \alpha + \gamma kd \sinh \gamma \alpha)]. \quad (\text{A.23})$$

In the limit as d approaches zero, the x and z components remain finite and become the required steps across the insulator. The y component, however, becomes infinite, so that the line integral of the conservative electric field around any closed path is zero.

The surface charge densities on the two interfaces, from the discontinuity in the normal electric field, are

$$\underline{\underline{\sigma}}(y = a) = \frac{\epsilon_o kz \underline{\underline{\phi}}_{i1}}{\sinh \alpha}, \quad (\text{A.24})$$

and

$$\begin{aligned} \underline{\underline{\sigma}}(y = g) = \epsilon_o kz \underline{\underline{\phi}}_{i1} (\sinh kg - \coth \alpha \cosh kg) \\ + j\omega \epsilon_o kz \underline{\underline{A}}_{f1} (F_1 \sinh kg + F_2 \cosh kg). \end{aligned} \quad (\text{A.25})$$

As d approaches zero the first term of $\underline{\underline{\sigma}}(y = g)$ becomes equal in magnitude but opposite in sign to $\underline{\underline{\sigma}}(y = a)$, and both vary as $\frac{1}{d}$, representing a tapered dipole layer. The second term of $\underline{\underline{\sigma}}(y = g)$ accounts for the discontinuity in the normal electric field across the insulator.

The discussion above shows that the discontinuity in the tangential electric field across the insulators is consistent with Maxwell's equations, provided that a tapered dipole layer is included as part of the solution. It is the presence of the dipole layer that enables all boundary conditions to be satisfied.

APPENDIX B

Field Solution Retaining all Components of the Vector Potential

In section 2.2 the vector potential was assumed to have only a z-component because of the excitation and geometry. Now the same electromagnetic fields are obtained without this assumption from different potentials. The vector and scalar potentials are defined by Eqs. 6 and 7:

$$\vec{B} = \nabla \times \vec{A}$$

and

$$\vec{E} = -\nabla \phi - \frac{\partial \vec{A}}{\partial t}.$$

The gradient of any scalar Ψ can be subtracted from \vec{A} to define a new vector potential

$$\vec{A}' = \vec{A} - \nabla \Psi \tag{B.1}$$

without changing \vec{B} . Eq. 2.2.10 then requires a new scalar potential

$$\phi' = \phi + \frac{\partial \Psi}{\partial t}. \tag{B.2}$$

This method of defining a new set of potentials, called a gauge transformation, leaves the fields invariant.⁷⁸

The derivation retaining all components of the vector potential for a constant fluid velocity differs little from the solution of section 3.1 and will not be repeated in full detail. The model used is the same, but $\nabla \cdot \vec{A}$ is no longer zero, so that Eqs. 8, 9, and 11 are required. The potentials satisfying Eqs. 9 and 11 are determined, constraint (8) is applied to the coefficients, and the fields are calculated and compared with the results of section 3.1. Although done only for the fluid, the same procedure can be applied to all regions.

The complex amplitude of the scalar potential in the fluid, from Eq. 11, is

$$\underline{\phi}_f = (\underline{\phi}_1 z + \underline{\phi}_3) \cosh \beta ky + (\underline{\phi}_2 z + \underline{\phi}_4) \sinh \beta ky, \tag{B.3}$$

where

$$\beta^2 = 1 + jR_M. \tag{B.4}$$

The form of the z -dependence is chosen to make all measurable quantities either independent of z or linear in z , as required for the infinite machine.

Working with components for the vector potential, the equation for $\underline{A_{fx}}$ is identical to that for $\underline{\phi_f}$, so that

$$\underline{A_{fx}} = (\underline{A_{x1}} z + \underline{A_{x3}}) \cosh \beta ky + (\underline{A_{x2}} z + \underline{A_{x4}}) \sinh \beta ky . \quad (\text{B. 5})$$

For the y and z -components there is both a natural response and a forced response due to $\underline{A_{fx}}$. Thus,

$$\begin{aligned} \underline{A_{fy}} = & (\underline{A_{y1}} z + \underline{A_{y3}}) \cosh \gamma ky + (\underline{A_{y2}} z + \underline{A_{y4}}) \sinh \gamma ky \\ & + j\beta \left[(\underline{A_{x1}} z + \underline{A_{x3}}) \sinh \beta ky + (\underline{A_{x2}} z + \underline{A_{x4}}) \cosh \beta ky \right] , \end{aligned} \quad (\text{B. 6})$$

and

$$\underline{A_{fz}} = \underline{A_{z1}} \cosh \gamma ky + \underline{A_{z2}} \sinh \gamma ky + \frac{j}{k} \left[\underline{A_{x1}} \cosh \beta ky + \underline{A_{x2}} \sinh \beta ky \right] , \quad (\text{B. 7})$$

where $\underline{A_{fz}}$ must be independent of z because the magnetic field cannot depend on z .

Equation 8 now provides constraints on the potentials. Equating the coefficients of each y and z -variation to zero gives

$$\underline{\phi_i} = v_s \underline{A_{xi}} , \quad (\text{B. 8})$$

and

$$\underline{A_{yi}} = 0 , \quad (\text{B. 9})$$

where $i = 1$ through 4.

From these potentials, the electromagnetic fields are

$$\underline{B_{fx}} = \gamma k (\underline{A_{z1}} \sinh \gamma ky + \underline{A_{z2}} \cosh \gamma ky) , \quad (\text{B. 10x})$$

$$\underline{B_{fy}} = jk (\underline{A_{z1}} \cosh \gamma ky + \underline{A_{z2}} \sinh \gamma ky) , \quad (\text{B. 10y})$$

and

$$\underline{E_{fz}} = j\omega (\underline{A_{z1}} \cosh \gamma ky + \underline{A_{z2}} \sinh \gamma ky) . \quad (\text{B. 11})$$

The remaining components are zero. The $\underline{A_{xi}}$ coefficients do not appear in the fields; they represent a natural response which cannot be measured. Comparison with the potentials in the fluid of section 3.1 before application of the boundary conditions,

$$\underline{\vec{A}}_f = \underline{\vec{i}}_z (\underline{A_{f1}} \cosh \gamma ky + \underline{A_{f2}} \sinh \gamma ky) , \quad (3.1.8)$$

and

$$\underline{\phi}_f = 0 , \quad (2.2.15)$$

shows that the identical fields are obtained.

The case in which \vec{v} is zero, as in the core, is slightly different. The three components of the vector potential are not coupled, and all have the same spatial dependence. Applying Eq. 8 and making the magnetic field independent of z and the z -component zero reduces this to the previous results.

The gauge transformation is defined by Eqs. B.1 and B.2. Consider the potentials of section 3.1 to be the unprimed set and the potentials derived here to be the primed set. Then

$$\underline{\Psi} = \frac{1}{jk} \left[(\underline{A_{x1}} z + \underline{A_{x3}}) \cosh \beta ky + (\underline{A_{x2}} z + \underline{A_{x4}}) \sinh \beta ky \right] , \quad (B.12)$$

and this is a particular gauge transformation.

APPENDIX C

Exciting Winding of Finite Thickness

Limitations on the current density in the exciting winding of a practical MHD induction machine may result in a winding whose thickness b is not small compared to the channel half-width a . This degrades the performance because, for the same total exciting current, the fluid magnetic field and power density are decreased. The degrading factor for the magnetic field is calculated and its effect on performance shown. The terminal voltage is found to possess an additional term that can be identified as a leakage reactance.

The analysis is the same as in section 3.1, except that the exciting sheet thickness b is not small. The model of Fig. 8 is used with an exciting current density

$$\vec{J}_e = \vec{i}_z \frac{NI}{b} \cos(\omega t - kx) . \quad (C.1)$$

The vector potentials in the fluid and core, as before, are

$$\underline{A}_f = \underline{A}_{f1} \cosh \gamma ky \quad \text{for } y \leq a , \quad (C.2)$$

and

$$\underline{A}_c = \underline{A}_{c1} e^{-\delta k|y|} \quad \text{for } y \geq a + b , \quad (C.3)$$

with \underline{A}_{f1} and \underline{A}_{c1} to be determined. The vector potential in the exciting plates is

$$\underline{A}_e = \frac{\mu_o NI}{k^2 b} + \underline{A}_{e1} \cosh ky + \underline{A}_{e2} \sinh ky , \quad (A.10)$$

using the results of Appendix A.

The boundary conditions on the magnetic field at $y = a$ and $y = a + b$ give four equations to solve for the four unknown constants. The result for the potential in the field is

$$\underline{A}_{f1} = \left\{ \frac{\mu_f NI}{k(\gamma \sinh \gamma a + \kappa \delta \cosh \gamma a)} \right\} F_D , \quad (C.4)$$

where the term in brackets is the potential when b is zero, and F_D is the derating factor due to the finite width,

$$F_D = \frac{\sinh \alpha_e + \delta \kappa_e (\cosh \alpha_e - 1)}{\alpha_e \left[\cosh \alpha_e + \sinh \alpha_e \frac{(\delta \kappa_e \gamma \tanh \gamma \alpha + \frac{\kappa}{\delta})}{(\gamma \tanh \gamma \alpha + \kappa \delta)} \right]} \quad (C. 5)$$

Here,

$$\alpha_e = bk, \quad (C. 6)$$

and

$$\kappa_e = \frac{\mu_e}{\mu_c}. \quad (C. 7)$$

Normally $\mu_f = \mu_e$, simplifying Eq. C. 5. Unless $\alpha_e = 0$, $F_D < 1$.

Since the vector potential in the fluid is decreased by F_D , all electromagnetic powers are decreased by $F_D F_D^*$, and the dependence of $F_D F_D^*$ on α_e for a given machine is of major importance. If F_D is small, the power level of the machine will be much less than the theory of Section III predicts.

For the special cases of an air core and an ideal iron core F_D can be simplified to

$$F_{D1} = \frac{\sinh \alpha_e + \cosh \alpha_e - 1}{\alpha_e (\sinh \alpha_e + \cosh \alpha_e)} \quad \text{for } \kappa = 1, \quad (C. 8)$$

and

$$F_{DO} = \frac{\sinh \alpha_e}{\alpha_e (\cosh \alpha_e + \frac{\sinh \alpha_e}{\gamma \tanh \gamma \alpha})} \quad \text{for } \kappa = 0, \quad (C. 9)$$

both for $\mu_f = \mu_e$ and no core loss. The former depends only on α_e while F_{DO} for $\gamma \alpha$ and α_e both much less than one is a function of the ratio of b to a . They are plotted in Fig. C-1 for several values of α . As α decreases, F_{DO} drops off much faster with increasing α_e .

The terminal voltage calculation is more complex for a winding of finite width because the source voltage per wire, ΔV_s of section 2. 3, is a function of both x and y . A model for the coil is required to take care of this. Assume the coil has a two-dimensional turns distribution of turns densities $N_1 \begin{Bmatrix} \cos kx \\ \sin kx \end{Bmatrix}$ and N_2 per unit length in the x and y directions for the two phases. There are $N_1 N_2$ turns per unit area, and the current density is

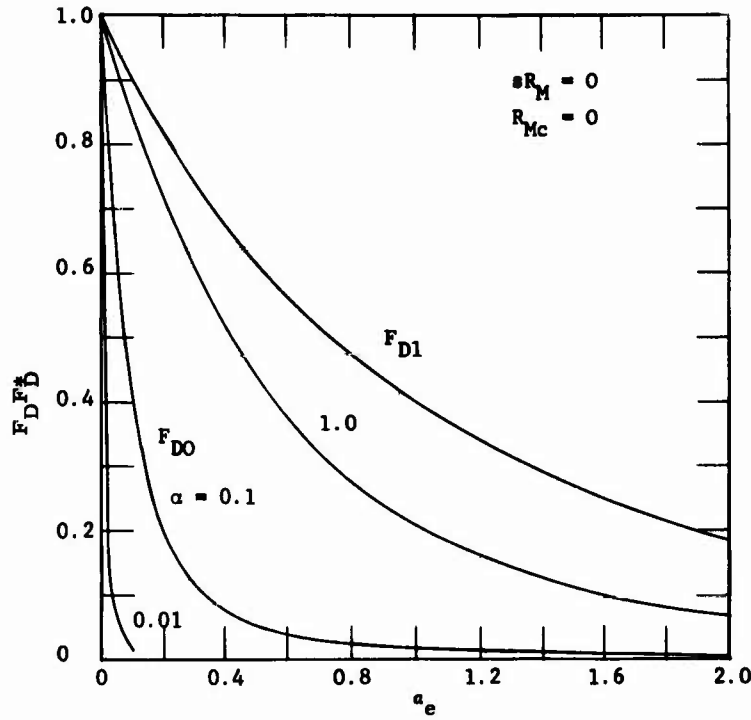


Fig. C-1. $F_D F_D^*$ as a function of α_e for four sets of machine parameters.

$$\vec{J}_e = \vec{i}_z N_1 N_2 I \cos(\omega t - kx) \quad (C. 1a)$$

for currents of $I \begin{Bmatrix} \cos \omega t \\ \sin \omega t \end{Bmatrix}$ per turn. The total number of turns per unit length in the x-direction is

$$N = N_1 N_2 b, \quad (C. 10)$$

where N corresponds to the previous turns density.

The terminal voltage is the sum of the voltage across each turn,

$$V = 2 \int_x^{x+\lambda} \int_a^{a+b} \left\{ \Delta V_s(x, y) e^{j\omega t} \right\} N_2 N_1 \cos kx \, dy dx, \quad (C. 11)$$

where N_1 and N_2 are assumed large so that the sum can be replaced by an integral. The result is

$$\begin{aligned} \underline{V} = R_e I + j \frac{\omega \mu_e 2 \pi c N^2 I}{k^3 b} \left(1 - \frac{\sinh \alpha_e}{\alpha_e} \right) \\ + j \frac{\omega 2 \pi c N}{k} \underline{A_{f1}} \cosh \gamma \alpha \left\{ \frac{\sinh \alpha_e}{\alpha_e} + \frac{\mu_e \gamma}{\mu_f} \tanh \gamma \alpha \frac{(\cosh \alpha_e - 1)}{\alpha_e} \right\}. \end{aligned} \quad (C. 12)$$

Comparison with section 3.2 shows that the first term is the resistance of the coil, and the last term represents the interaction with the fluid. The second term, with no previous equivalent, is a leakage reactance caused by some of the magnetic field not penetrating into the fluid.⁴¹ The last term is decreased by F_D times the expression in brackets. The ratio of the real part of this term to that when $\alpha_e = 0$, or equivalently the resistance ratio, is equal to $F_D F_D^*$ when there is no core loss.

The coil thickness will be important in air-core machines because a large excitation current is required for a reasonable power level. The problem is sharply reduced for an iron core by placing the winding in slots, as is conventionally done for rotating machines. This eliminates thickness effects completely, provided the iron teeth do not saturate, except that leakage still occurs.

APPENDIX D

Viscous Power Loss

The viscous power loss will be important at the velocities and Reynolds numbers expected for a practical MHD induction machine, and the flow will probably be turbulent. However, the viscous power must be small compared to the power output in order to obtain a reasonable efficiency. The viscous loss is first found for laminar flow, where analytical expressions are available, and then the extension to turbulent flow is discussed. It is shown that the use of a friction factor for MHD flows, as is done for OHD (ordinary hydrodynamics) flows, may lead to erroneous results for the viscous power loss.

The mechanical input power to the fluid volume of Fig. D-1 for a flow independent of x and z is

$$P_{in} = -2c \int_0^a \Delta p v dy, \quad (D.1)$$

where Δp is the pressure difference across the volume, defined as positive if p increases with x , and c is the depth in the z -direction. If Δp is independent of y , this becomes

$$P_{in} = -Q \Delta p, \quad (D.1a)$$

where

$$Q = 2ac\bar{v} \quad (D.2)$$

is the volume flow rate, and \bar{v} is the average velocity.

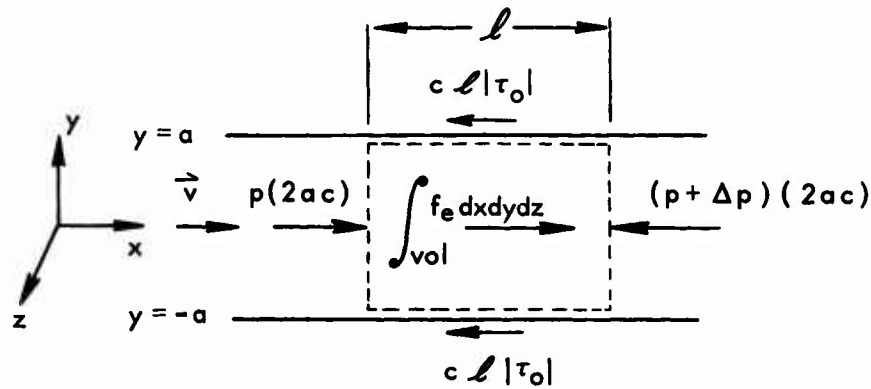


Fig. D-1. Forces acting on a fluid volume extending across the channel of depth c .

D.1 LAMINAR FLOW

The viscous power loss can be evaluated analytically for laminar flow. The contribution to the pressure gradient due to viscosity, from Eq. 5g, is $\eta \frac{d^2 v}{dy^2}$ for no x-dependence, but

$$dP = -\eta v \frac{d^2 v}{dy^2} \quad (D.3)$$

is not the viscous power density, as is shown below.

Consider the small fluid volume of Fig. D-2. The forces acting on the volume are pressure, the fluid shear stress on the top and bottom surfaces,

$$\tau = \eta \frac{dv}{dy} , \quad (D.4)$$

and the body force density f_e . For no x and z-dependence the mechanical power input is

$$\begin{aligned} \Delta P_{in} = & -\left[p\left(x + \frac{\Delta x}{2}, y\right) - p\left(x - \frac{\Delta x}{2}, y\right)\right] v(y) \Delta y \Delta z \\ & + \left[\tau\left(y + \frac{\Delta y}{2}\right) v\left(y + \frac{\Delta y}{2}\right) - \tau\left(y - \frac{\Delta y}{2}\right) v\left(y - \frac{\Delta y}{2}\right)\right] \Delta x \Delta z \\ & + f_e(y) v(y) \Delta x \Delta y \Delta z. \end{aligned} \quad (D.5)$$

Dividing this by the volume and taking the limit as the volume shrinks to a point gives the input power density,

$$dP_{in} = -v \frac{\partial p}{\partial x} + \tau \frac{dv}{dy} + v \frac{d\tau}{dy} + f_e v. \quad (D.6)$$

This must be the viscous power as there is no other mechanism for dissipating mechanical power. Writing the force balance equation for the fluid volume gives

$$\frac{\partial p}{\partial x} = \frac{d\tau}{dy} + f_e , \quad (D.7)$$

and Eq. D.6 becomes

$$dP_v = \tau \frac{dv}{dy} = \eta \left(\frac{dv}{dy}\right)^2 . \quad (D.8)$$

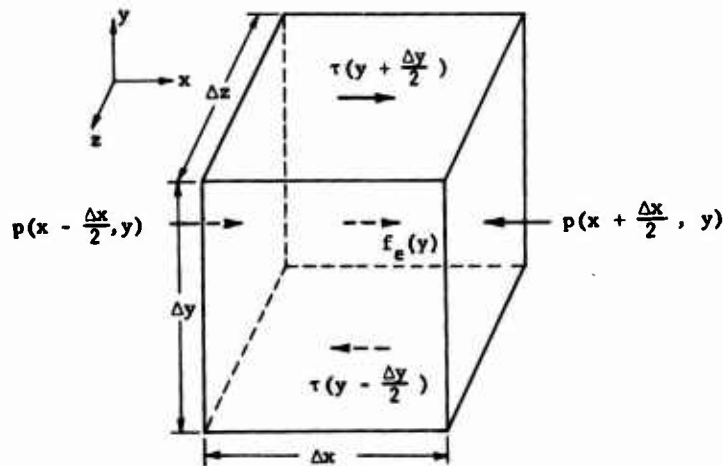


Fig. D-2. Forces and stress acting on an elemental volume of fluid centered at (x, y, z) .

The total viscous power loss in a length ℓ of the channel is

$$P_v = 2c\ell\eta \int_0^a \left(\frac{dv}{dy}\right)^2 dy. \quad (D.9)$$

This could be extended to the general three-dimensional case by including the additional terms.

The error in Eq. D.3 is that some of the power carried into the volume due to the viscous pressure gradient flows out across the sides due to the viscous shear stress. This does not occur if the viscous power is integrated over the whole channel because the velocity is zero at the walls. In fact,

$$P_v = -2c\ell\eta \int_0^a v \frac{d^2y}{dy^2} dy \quad (D.9a)$$

is identical to Eq. D.9 for this case only, as is seen if Eq. D.9a is integrated by parts, although conceptually it is in error.

The viscous power loss for OHD channel flow, with the parabolic profile

$$v = \bar{v} \frac{3}{2} \left[1 - \left(\frac{y}{a}\right)^2\right], \quad (D.10)$$

is

$$P_v = \frac{6c\ell\eta\bar{v}^2M}{a}. \quad (D.11)$$

For the Hartmann profile, Eq. 137, the viscous loss is

$$P_v = \frac{c \ell \eta \bar{v}^2 M}{a} \frac{\left[\tanh M - \frac{M}{\cosh^2 M} \right]}{\left[1 - \frac{\tanh M}{M} \right]^2} . \quad (D. 12)$$

As M approaches zero this reduces to Eq. D. 11, while for large M it becomes

$$P_v = \frac{c \ell \eta \bar{v}^2 M}{a} . \quad (D. 12a)$$

The MHD viscous loss is always greater than the OHD viscous loss because of the sharper velocity gradient near the wall. Eq. D. 12 and the asymptote, Eq. D. 12a, are plotted in Fig. D-3.

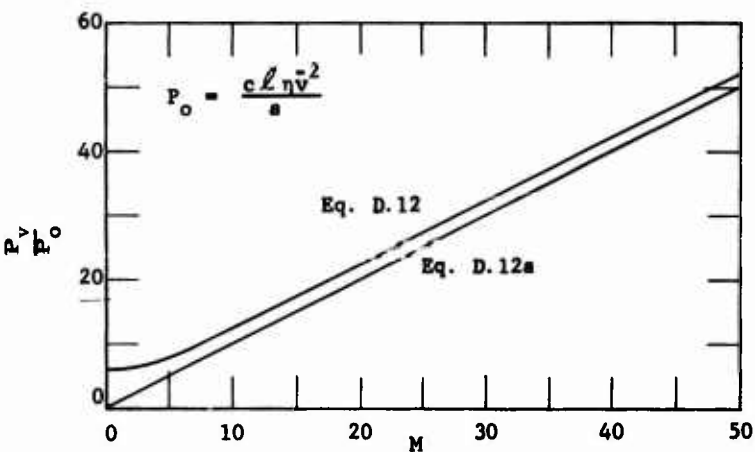


Fig. D-3. Viscous power loss for Hartmann profile as a function of M .

D.2 WALL SHEAR STRESS

It is convenient in OHD flow problems to work in terms of the wall shear stress

$$\tau_o = \eta \left. \frac{dv}{dy} \right|_{y=a} . \quad (D. 13)$$

Writing the force balance equation for the volume of Fig. D-1 gives

$$2ac \Delta p = -2c \ell |\tau_o| + \int_{vol} f_e dx dy dz , \quad (D. 14)$$

where Δp is independent of y , f_e is the body force density, and $|\tau_o|$ is used to avoid sign confusion. The viscous power loss, using only the contribution to Δp due to the wall shear stress, is

$$P_{v\tau} = 2c\ell\tau_o\bar{v} \quad (D.15)$$

from Eq. D.1a, if the viscous pressure difference Δp_v is constant across the channel. This is valid for OHD flows with no body forces, but is not correct for MHD flows because f_e varies across the channel, and, since the sum is constant, Δp_v must also vary. Equation D.15 is then the product of the averages, which is different from the average of the product.

This is easily shown for Hartmann flow. The wall shear stress is

$$\tau_o = \frac{\eta\bar{v}M}{a} \frac{\tanh M}{\left[1 - \frac{\tanh M}{M}\right]}, \quad (D.16)$$

and the viscous loss from Eq. D.15 is

$$P_{v\tau} = \frac{2c\ell\eta\bar{v}^2}{a} \frac{M \tanh M}{\left[1 - \frac{\tanh M}{M}\right]}. \quad (D.17)$$

For small M this reduces to Eq. D.11 for OHD flow, but for large M it becomes

$$P_{v\tau} = \frac{2c\ell\eta\bar{v}^2 M}{a}, \quad (D.17a)$$

which is twice the correct asymptote, Eq. D.12a. The wall shear stress can be used to obtain the average viscous pressure drop, but not the viscous power loss in MHD flows.

D.3 FRICTION FACTOR

In fluid mechanics a friction factor f defined by

$$f = \frac{8\tau_o}{\rho\bar{v}^2} \quad (D.18)$$

is conventionally used to express the pressure drop due to viscosity as

$$\Delta p_v = \frac{f\ell\rho\bar{v}^2}{2D_h}; \quad (D.19)$$

where

$$D_h = \frac{4 \text{ (cross-section area of flow)}}{\text{(wetted perimeter)}}, \quad (\text{D. 20})$$

the hydraulic diameter for a channel of arbitrary cross section, is defined so that f is independent of the channel shape for turbulent flow. This is not true for laminar flow, where

$$f_r = \frac{64}{R_e} \quad (\text{D. 21r})$$

for a round pipe, and

$$f_p = \frac{96}{R_e} \quad (\text{D. 21p})$$

for flow between two parallel plates. Here,

$$R_e = \frac{\rho \bar{v} D_h}{\eta} \quad (\text{D. 22})$$

is the Reynolds number. The friction factor for Hartmann flow between two parallel plates is

$$f_H = 32 \frac{M}{R_e} \frac{\tanh M}{\left[1 - \frac{\tanh M}{M}\right]}. \quad (\text{D. 21h})$$

This reduces to Eq. D. 21p as M approaches zero.

D.4 TURBULENT FLOW

The friction factor is introduced because it is convenient for turbulent flow, where analytical expressions for the viscous pressure drop and power loss are not available. It has been measured experimentally as a function of R_e for various conditions, and both graphs and approximate equations are available. For OHD flows this gives the pressure drop and the power loss. Unfortunately, it gives the correct average pressure drop but the wrong viscous power loss for MHD flows because f is based on the wall shear stress. This leaves no method of calculating the viscous power loss for turbulent MHD flows until further experimental measurements are made. Since the friction factor for laminar flow gives a viscous loss of the correct order of magnitude but high by a factor of about 2, the friction factor can be used for turbulent flows to give order

of magnitude results. This is used as the best, and only, alternative. It is valid only for small MHD forces, which is not of interest for energy conversion.

Using experimental data, the friction factor for OHD turbulent flow is ⁷⁹

$$\frac{1}{\sqrt{f}} = 2.0 \log_{10} (R_e \sqrt{f}) - 0.8 \quad (D.23)$$

for smooth walls, where the flow is turbulent for R_e greater than about 2000. It is usually more convenient to use a graph, such as that given by Schlichting,⁸⁰ by Moody,⁵⁰ or in section 5.5. Sufficient experimental measurements are available so that this relation is well established.

For turbulent MHD flows only a limited amount of experimental data is available, all for DC magnetic fields.^{52,54,56} Harris⁸¹ obtained an analytical expression for f based on some of this data,

$$\frac{1}{\sqrt{f}} = 4.0 \log_{10} \left(\frac{\sqrt{f} R_e}{M} \right) - \frac{\sqrt{f} R_e}{32M^2} - 2.772, \quad (D.24)$$

valid for $\frac{M^2}{\sqrt{f} R_e} > 0.053$. The flow is turbulent for $\frac{R_e}{M} > 900$.⁵² These measurements made no distinction between the pressure drop due to viscosity and that due to circulating currents, both are included in f . Since the circulating-current losses are already included in P_m and P_r for the induction machine, this friction factor is of limited value for the present investigation. Friction factors are studied in section 5.5 using turbulent boundary-layer theory, and the results are compared with Eqs. D.21h, D.23, and D.24 in Figs. 44-46.

Before leaving this discussion of turbulent flow and losses, it is interesting to compare the OHD turbulent and MHD laminar profiles, as shown in Figs. 39 and 27 and discussed in section 5.1. Both have the same characteristic shape, flat in the center of the channel with sharp velocity gradients near the walls, and both have higher viscous loss than OHD laminar flow because of these large gradients. The transition from MHD laminar to MHD turbulent flow and the addition of turbulent mixing will have little effect on the profile in the center of the channel, which is already relatively flat. It is not clear what the transition will do to the profile shape near the wall, which is already steep, and to the viscous loss. The viscous loss will be higher than for MHD laminar flow, but not necessarily higher than for OHD turbulent flow. The turbulent boundary-layer calculations of section 5.5, if valid, show that f is larger for MHD turbulent flow than for OHD turbulent flow at small values of R_e , but smaller at large values of R_e .

Many questions remain about turbulent MHD flows. Careful experimental measurements of losses and velocity profiles are required before theoretical predictions can be made with reasonable accuracy.

APPENDIX E

Numerical Methods

The numerical methods used in Section IV to solve the differential equations and evaluate the integrals are presented. Several techniques were tried for each, and the best selected from tests on the electromagnetic fields and powers for a constant fluid velocity, for which analytical solutions are known.

E.1 DIFFERENTIAL EQUATIONS

The equation to be solved is a second-order differential equation of the form

$$\frac{d^2 F}{dy^2} + A(y) \frac{dF}{dy} + B(y) F = C(y), \quad (E.1)$$

where $A(y)$, $B(y)$, and $C(y)$ may be constants or zero, and all may be complex numbers. Two fundamental approaches are available:

1. Break Eq. E.1 into two coupled first-order equations,

$$\frac{dF}{dy} = DF, \quad (E.2)$$

and

$$\frac{d(DF)}{dy} = -A(y) DF - B(y) F + C(y), \quad (E.3)$$

and determine both F and DF together.

2. Solve the second-order equation directly by using special techniques available when the first derivative is not present, $A(y) = 0$. This gives F , and DF , if required, is then calculated by numerical differentiation.

The six methods tested are outlined below along with the equations, error estimates, and relevant comments. Only the last method uses the second approach. After the presentation of all six their results are compared. These methods were selected as being the simplest ones with reasonable accuracy, and as they gave good results, more complex methods were not required. For a more detailed discussion see Hildebrand.⁸²

Method 1

Euler's method using the equation

$$F_{n+1} = F_n + hF'_n + \frac{h^2}{2} F''(\xi), \quad (E.4)$$

where the subscript n denotes the value of y , the prime the derivative with respect to y , and h is the constant point spacing, $y_{n+1} - y_n$. The last term is the truncation error due to neglecting higher order terms; double prime indicates the second derivative, and ξ is some value of y between the largest and smallest values in the equation, y_{n+1} and y_n in this case. This method is self-starting, only the initial value is needed, and is the simplest but least accurate.

Method 2

A modification of method one using

$$F_{n+1} = F_{n-1} + 2hF'_n + \frac{h^3}{3} F'''(\xi). \quad (E.5)$$

It is considerably more accurate and gives appreciably better results, but may be unstable, as discussed later. It is not self-starting; the initial value plus one additional point is needed.

Method 3

Adams method retaining first differences,

$$F_{n+1} = F_n + \frac{h}{2} (3F'_n - F'_{n-1}) + 5 \frac{h^3}{12} F'''(\xi). \quad (E.6)$$

The accuracy is about the same as in method 2, but it requires one additional term in the equations. It is also not self-starting.

Method 4

An iterative procedure using method 2 as the initial predictor and

$$F_{n+1} = F_{n-1} + \frac{h}{3} (F'_{n+1} + 4F'_n + F'_{n-1}) - \frac{h^5}{90} F^{(5)}(\xi) \quad (E.7)$$

to iterate, where $F^{(5)}(\xi)$ is the fifth derivative. This has a smaller error because it uses third differences, but it may be unstable. It generally requires an initial prediction to obtain F'_{n+1} , and can be used alone only in special cases. Two iterations were usually sufficient.

Method 5

A second iterative procedure using method 3 as the initial predictor and

$$F_{n+1} = F_n + \frac{h}{12} (5F'_{n+1} + 8F'_n - F'_{n-1}) - \frac{h^4}{24} F^{(4)}(\xi) \quad (E.8)$$

to iterate. This is not quite as accurate as method 4, although it has the same number of terms, because it uses only second differences. Method 4 is preferable except when unstable.

Method 6

For the special case of no first derivative, $A(y) = 0$, the second-order differential equation can be solved directly by using

$$F_{n+1} = 2F_n - F_{n-1} + \frac{h^2}{12} (F''_{n+1} + 10F''_n + F''_{n-1}) - \frac{h^6}{240} F^{vi}(\xi). \quad (E.9)$$

Substituting Eq. E.1 in Eq. E.9 and simplifying gives

$$F_{n+1} = \frac{2F_n(1 - \frac{5}{12}h^2B_n) - F_{n-1}(1 + \frac{h^2}{12}B_{n-1}) + \frac{h^2}{12}(C_{n+1} + 10C_n + C_{n-1})}{(1 + \frac{h^2}{12}B_{n+1})}. \quad (E.10)$$

This has the smallest truncation error and is the easiest to use because there are no iterations, but it requires a numerical differentiation for DF , which is to be avoided if at all possible.⁸³ It is self-starting using symmetry, and is used to start the other methods.

The method of starting the solutions requires special comment. The initial values F_1 and DF_1 are specified, but all methods except the first also require F_2 and DF_2 . A series, as normally used, is not convenient because the coefficients may be known only at points, necessitating numerical differentiation. Symmetry about $y = 0$ can be used to solve Eq. E.9, giving

$$F_2 = \frac{F_1(1 - \frac{5h^2}{12}B_1) + \frac{h^2}{12}(C_2 + 5C_1)}{(1 + \frac{h^2}{12}B_2)} \quad (E.11)$$

for the case when A is zero. This is used to start all methods because now DF_2 is easily obtained. Using any of the other methods with symmetry is not practical for finding F_2 .

The six methods outlined were tested on Eq. 127 for the vector potential in the fluid with a constant fluid velocity since the exact solution is known, Eq. 41. The results are given in Table E.1 for several values of \bar{s} , R_M , and α . The core properties and boundary conditions enter only into the constants. The number of figures of accuracy, i.e., the maximum number of correct digits after rounding, is given for the real and imaginary parts of F and DF at $\tilde{y} = 1$, which is more convenient for comparison purposes than numerical values. The computer uses 8 digits, or 16 with double-precision. The additional accuracy of double-precision was not required in solving Eq. 127, and was not tried because then the complex statements could not be used, which would result in a vastly more complicated program. It was used for the velocity profile solutions, as described in section 4.5, where the numbers are real and the additional accuracy was needed.

Table E.1 Numerical solution tests of Eq. 127.

					Number of Digits of Accuracy at $\tilde{y} = 1$.			
s	R_M	α	No. Points	Method	Re(F)	Im(F)	Re(DF)	Im(DF)
-1	1	0.1	100	1	4	2	6	4
				2	7	5	6	5
				3	6	5	6	5
				4	7	6	6	5
				5	6	4	6	5
				6	4	4	1	4
-1	100	0.1	100	1	1	1	1	2
				2	4	4	4	4
				3	3	4	4	4
				4	5	6	6	6
				5	5	6	6	6
				6	3	4	3	3
-1	100	0.1	1000	2	5	5	5	4
				4	5	5	5	4
				5	5	5	5	4
				6	2	2	1	2
-1	10	1	100	1	1	0	1	1
				2	2	2	3	3
				3	2	2	3	2
				4	6	6	6	6
				5	6	5	5	5
				6	5	4	4	3
-1	10	1	1000	2	4	5	6	4
				4	6	5	6	5
				5	5	5	5	5
				6	3	2	3	1
-1	10	10	100	1	0	0	0	0
				2	0	0	1	0
				3	0	0	0	0
				4	2	3	3	1
				5	1	1	1	0
				6	3	3	3	1
-1	10	10	1000	2	3	1	2	0
				4	5	4	5	3
				5	4	4	3	3
				6	3	3	3	2

Method 1 is immediately discarded as being too inaccurate. Methods two and three are about the same. The most accurate is method four, which is used whenever possible. Method 6 suffers from round-off error; the results improve as the number of points decreases for the small $\gamma\alpha$ cases. This could be eliminated by using double-precision, except for the problem of complex numbers. One hundred or more points are required to pick up the sharp velocity variation at the walls, and for the solution of Eq. 128.

If the solution of the differential equation is close to a decaying exponential, methods 2 and 4 are unstable; they generate parasitic solutions to the approximate

difference equation which grow and quickly swamp out the desired result. In this case method 5 is substituted; it is only slightly poorer than method four, and is stable.

E.2. INTEGRATION

The numerical evaluation of integrals is required for finding the powers and for calculating averages. The integration methods tested are the Newton-Cotes two-point (trapezoidal rule), three-point (parabolic or Simpson's rule), and six-point formulas. The equations are

$$\int_{y_n}^{y_{n+1}} F(y) dy = \frac{h}{2} (F_n + F_{n+1}) - \frac{h^3}{12} F''(\xi), \tag{E.12}$$

$$\int_{y_n}^{y_{n+2}} F(y) dy = \frac{h}{3} (F_n + 4F_{n+1} + F_{n+2}) - \frac{h^5}{90} F^{iv}(\xi), \tag{E.13}$$

and

$$\begin{aligned} \int_{y_n}^{y_{n+5}} F(y) dy = & \frac{5h}{288} (19F_n + 75F_{n+1} + 50F_{n+2} + 50F_{n+3} + 75F_{n+4} \\ & + 19F_{n+5}) - \frac{275}{12096} h^7 F^{vi}(\xi), \end{aligned} \tag{E.14}$$

using the same notation as in section E.1. The last term in each equation is the error estimate. These three formulas were selected because the choice of a convenient number of points, dictated by the differential equation solution, always gave a number divisible by 1, 2, and 5.

Table E.2. Numerical integration tests of Eq. 133, 100 Points.

			Number of Digits of Accuracy		
$\bar{\epsilon}$	R_M	α	2-point	3-point	6-point
-1	1	0.01	6	6	6
		0.1	6	6	6
		1	4	6	5
		10	2	5	6
-0.04	25	1	4	7	7
-0.1			4	6	6
-0.4			3	6	6
-1.0			3	6	7
-10.0			2	5	5
-0.04	25	10	3	5	6
-0.1			2	4	5
-0.4			0	3	4
-1.0			1	3	3

The methods were tested by evaluating the integral for P_r , Eq. 133, with a constant fluid velocity. The results are given in Table E.2 for several sets of parameters using the same method as in Table E.1, all for 100 points across the channel half-width. Except for $\gamma \alpha$ small, the results became worse as the number of points was decreased. The six-point formula, Eq. E.14, was selected as the preferred method.

APPENDIX F

Inverse Transform

The calculation of $\underline{A}_f(x, y)$ from the known transformed vector potential requires the evaluation of the inversion integral

$$\underline{A}_f(x, y) = \int_{d-j\infty}^{d+j\infty} \underline{A}_f(p, y) e^{pkx} \left(\frac{kdp}{2\pi j} \right) , \quad (F.1)$$

where d is a constant determined by the region of convergence of $\underline{A}_f(p, y)$. The normal procedure of evaluating the integral is to close the path with a semicircle (or other appropriate curve) of large radius, as shown in Fig. F-1, resulting in a closed contour integral whose value is the sum of the residues of the poles inside the contour. This is equal to the integral of Eq. F.1 only if the contribution from the semicircle is zero.

The doubly infinite series of poles for $\underline{A}_f(p, y)$ extends to infinity in both directions along the real axis, so that the semicircle must always cut the line of poles. To see that the integral over the semicircle is zero, first make approximations for large i ,

$$p_i^{\pm} \approx \pm \frac{i\pi}{2} , \quad (F.2)$$

and

$$\gamma \approx jp . \quad (F.3)$$

Next choose a curve, not necessarily a semicircle although that is conceptually the easiest, such that the magnitude of p is large and the curve crosses the line of poles at

$$p = \pm \frac{(i + \frac{1}{2}) \pi}{\alpha} . \quad (F.4)$$

By choosing p (or i) sufficiently large, the integral along the curve can be made arbitrarily small, approaching zero in the limit, and the inverse transform is thus the sum of the residues. This type of problem arises in the study of heat conduction, and is treated in more detail in the standard texts.^{86,87}

The choice of d is determined from the excitation and the natural response. The transform for the exciting current, Eq. 201, requires $\text{Re}\{p\}$ positive for the inverse transform to give the original function. For the natural response, $\text{Re}\{p\}$ must lie

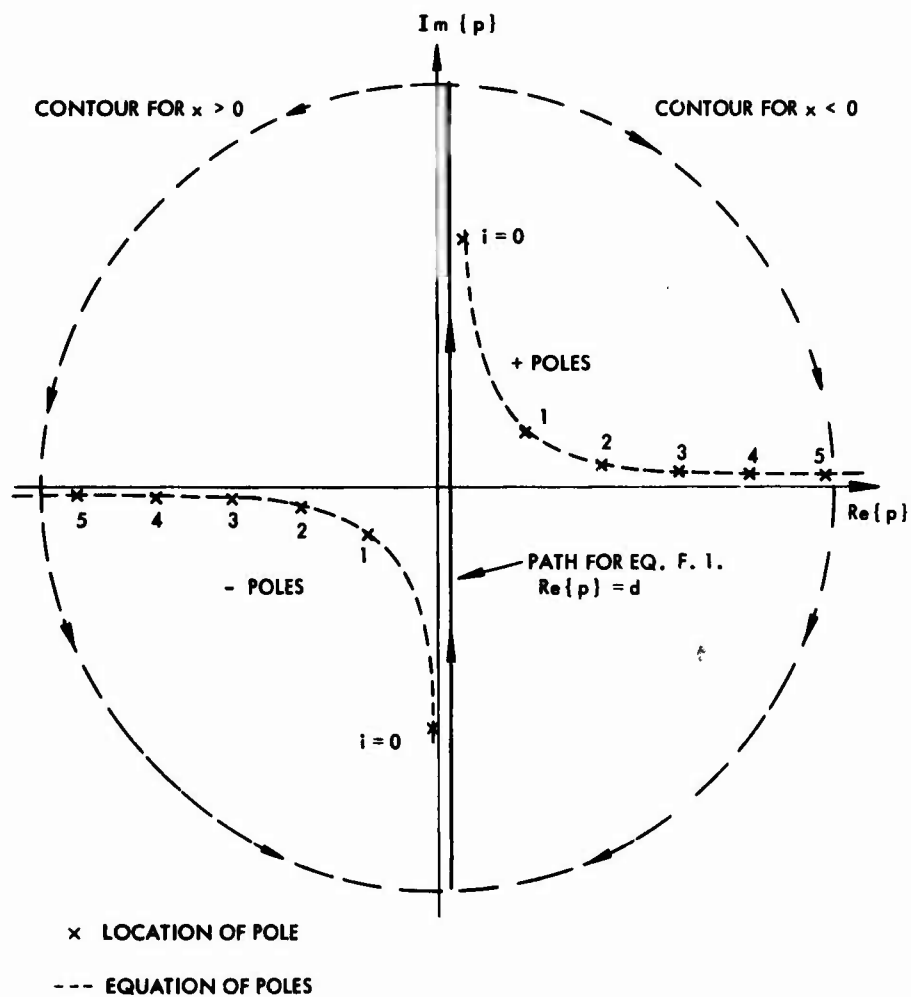


Fig. F-1. Sketch of poles and contours for inverse transform.

between the two 0-order roots. For the net system response, it must lie in the joint region, between 0 and p_0^+ . It makes no contribution to the integral except to determine the poles for a given region of space.

APPENDIX G

Conducting Channel Walls and Insulators of Finite Thickness

The presence of conducting channel walls and insulation in addition to the fluid between the exciting coils will degrade the machine performance because of the currents induced in the channel walls, which are a pure loss, and the increased air gap or reluctance of the magnetic circuit. These have not been considered in the previous analysis because they are not fundamental to the induction machine, but their effect may be disastrous if not allowed for in constructing the machine.

The model, Fig. G-1, differs from that analyzed in Section III by including channel walls and insulation of finite thickness a_w and a_i , respectively. Only the slit-channel machine is of practical interest for a generator, so that attention is accordingly restricted to this case. This avoids having to find solutions in four regions and then satisfy conditions at three boundaries, as in Appendices A and C. For the slit-channel approximation, $(a + a_w + a_i)k \ll 1$, the magnetic field is completely transverse. For this case a_i is the total insulation thickness, it makes no difference if some of it is located between the wall and fluid, or core and excitation. The insulation may be either electrical or thermal, provided that it does not conduct electricity. The permeabilities of the fluid, wall, and insulation are taken to be that of free space.

The slit-channel approximation rules out the use of the differential laws. Instead, the integral form of Eq. 5a,

$$\int_c \frac{\vec{B}}{\mu} \cdot d\vec{l} = \int_{\text{surf}} \vec{J} \cdot \vec{n} da, \quad (G.1)$$

is used to find either the magnetic field or the vector potential. The magnetic field between the core sections is y-directed and independent of y, and the vector potential is a constant,

$$\vec{A} = \text{Re} \left\{ \vec{i}_z A_1 e^{j(\omega t - kx)} \right\}. \quad (G.2)$$

The form of the vector potential in the core,

$$\vec{A}_c = \text{Re} \left\{ \vec{i}_z A_{c1} e^{-\delta k |y|} e^{j(\omega t - kx)} \right\}, \quad (G.3)$$

is unchanged. From the continuity of the normal magnetic field at the edge of the core,

$$\underline{A_{c1}} = \underline{A_1} e^{\delta \alpha_1}, \quad (G.4)$$

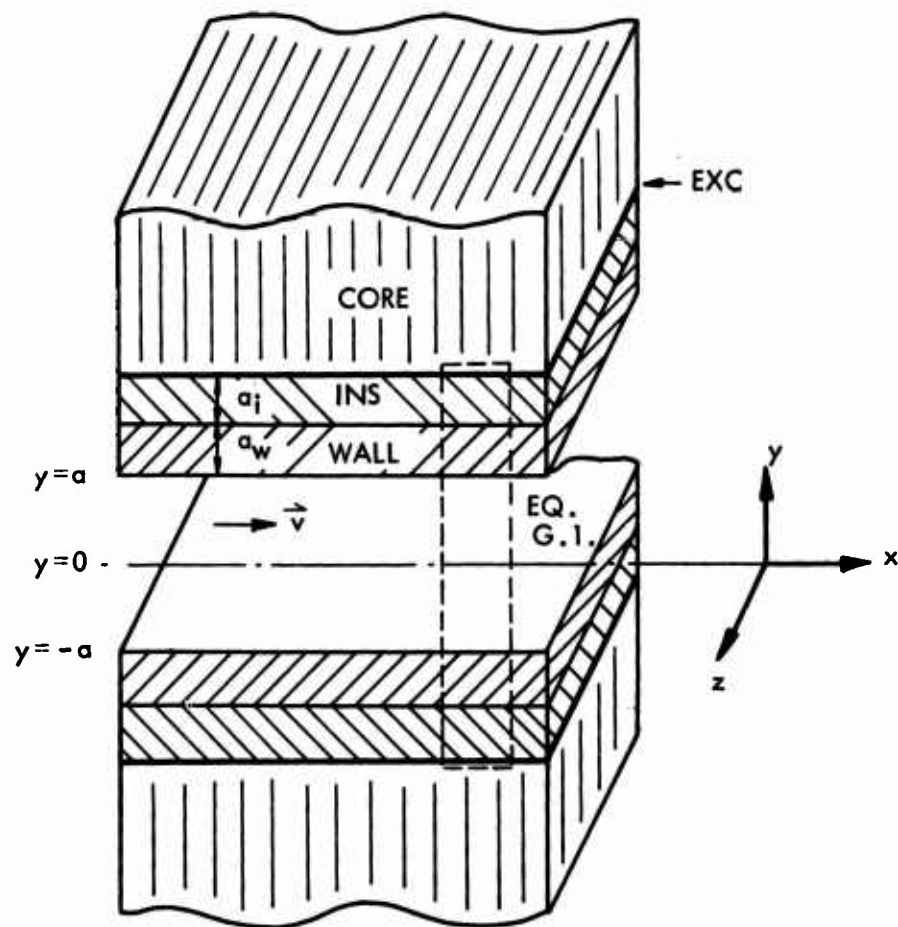


Fig. G-1. The Model.

where

$$\alpha_1 = (a + a_w + a_i)k \quad . \quad (G.5)$$

Solving for \vec{B} and \vec{J} in terms of the vector potential and integrating Eq. G. 1 along the dashed contour shown in Fig. G-1 gives

$$\frac{A_1}{k} = \frac{\mu_o NI}{k[\gamma^2 \alpha + \gamma_w^2 \alpha_w + \alpha_i + \kappa \delta]} \quad . \quad (G.6)$$

This is the simplest contour because the current in the core does not enter. Equation G. 6 is similar to the approximate form of Eq. 41, with the addition of

$$\gamma_w^2 = 1 + j R_{Mw} \quad (G.7)$$

$$R_{Mw} = \frac{\mu_o \sigma_w v_s}{k} \quad (G. 8)$$

$$\alpha_w = \alpha_w k \quad (G. 9)$$

$$\alpha_i = \alpha_i k \quad (G. 10)$$

Defining a derating factor F_D for the vector potential, as in Appendix C, gives

$$A_1 = \left\{ \frac{\mu_o NI}{k(\gamma^2 \alpha + \kappa \delta)} \right\} F_D \quad (G. 11)$$

where the term in brackets is the potential without the walls and insulation, and

$$F_D = \frac{1}{1 + \left[\frac{\gamma_w^2 \alpha_w + \alpha_i}{\gamma^2 \alpha + \kappa \delta} \right]} \quad (G. 12)$$

The power density and Hartmann number in the fluid are changed by $F_D F_D^*$ provided NI is the same. Plotting F_D is not convenient because it depends on seven parameters: sR_M , R_{Mw} , R_{Mc} , α , α_w , α_i , and κ . For a practical set of generator parameters: $sR_M = -1$, $R_{Mw} = 10$, since R_{Mw} is of the same size as R_M , $\alpha = 0.1$, $\alpha_w = \alpha_i = \frac{\alpha}{10}$, and $\kappa = 0$; the result is $F_D = 0.833 (1-j)$, and $F_D F_D^* = 1.388$. The field in the fluid may be larger with the walls for a generator because the induced currents in the walls and fluid are out of phase and partly cancel. Unfortunately, the performance is not improved. There is no similar effect for a pump.

The machine performance is best indicated by the power flow. The mechanical power output P_m and the powers dissipated in the fluid and walls, P_r and P_w , calculated from Eqs. 28 and 30, are

$$P_m = \frac{cn\lambda v_s k^2 A_1 A_1^*}{\mu_o} \alpha s (1-s) R_M \quad (G. 13)$$

$$P_r = \frac{cn\lambda v_s k^2 A_1 A_1^*}{\mu_o} \alpha s^2 R_M \quad (G. 14)$$

and

$$P_w = \frac{cn\lambda v_s k^2 A_1 A_1^*}{\mu_o} \alpha_w R_{Mw} \quad (G. 15)$$

The power supply to the machine by the excitation P_s cannot be found from Poynting's Theorem due to the approximate solution. However,

$$P_s = P_m + P_r + P_w \quad (G. 16)$$

from conservation of energy, which gives

$$P_s = \frac{cn\lambda v_s k^2 A_1 A_1^*}{\mu_0} [\alpha_s R_M + \alpha_w R_{Mw}] \quad (G. 17)$$

Core loss, shown in Section VII to be negligible in practice, is not considered.

The ratio of P_s with to without the walls and insulation, denoted by F_P , and the efficiency determine the change in performance. Two cases are distinguished, depending on whether the magnetic field, corresponding to saturation of the core, or the excitation NI is held constant. The ratios, differentiated by subscripts B and I, are

$$F_{PB} = 1 + \frac{\alpha_w R_{Mw}}{\alpha_s R_M} = 1 + \frac{a_w \sigma_w}{as \sigma_f} \quad (G. 18)$$

where the second term is the ratio of the power dissipated in the walls to that supplied to the fluid; and

$$F_{PI} = (F_D F_D^*) F_{PB} \quad (G. 19)$$

The walls may increase the magnetic field for a generator, $F_D F_D^* > 1$, but the wall loss decreases the output power for a generator, $F_{PB} < 1$, and increases the input power for a pump, $F_{PB} > 1$. The efficiencies for either B or NI constant, always decreased, are

$$e_g = \left(\frac{1}{1-s} \right) F_{PB} \text{ for } s < 0, \quad (G. 20)$$

and

$$e_p = \left(\frac{1-s}{F_{PB}} \right) \text{ for } s > 0. \quad (G. 21)$$

For the practical parameters used to find F_D , $F_{PB} = 0$, and the power generated in the fluid just supplies the wall loss. For a generator or pump where efficiency is important,

$$\left| \frac{\alpha_w R_{Mw}}{\alpha_s R_M} \right| = \left| \frac{a_w \sigma_w}{as \sigma_f} \right| \ll 1 \quad (G. 22)$$

so that the wall loss does not dominate.

This analysis throws a sobering light on the construction of a high-efficiency induction machine. The primary problem is the conducting wall, the insulation has relatively little effect. Since most wall materials are good conductors, and since from the numbers of Section VII it will be very hard to make $a_w \ll a$, it appears that the only solution is a machine without a channel wall. This might be accomplished by using the core to provide structural strength and placing a thin thermal and electrical insulator between the fluid and core.

References

1. White, D. C., and Woodson, H. H., Electromechanical Energy Conversion, John Wiley and Sons, Inc., New York, 1959, Section 3.6.4.
2. Fitzgerald, A. E., and Kingsley, C., Electric Machinery, McGraw-Hill Book Co., Inc., New York, 2nd Edition, 1961, Section 3.6, Chapters 6 and 10.
3. Laithwaite, E. R., and Barwell, F. T., "Linear Induction Motors for High-Speed Railways," Electronics and Power, **10**, 100-103, 1964.
4. Laithwaite, E. R., "Rotor Windings for Induction Motors with Arc-Shaped Stators," Proc. Inst. Elec. Engrs. (London), **111**, 315-321, 1964.
5. Martin, T., Faraday's Diary, G. Bell and Son, London, 1932, Vol. 1, 409-413.
6. Northrup, E. F., "Some Newly Observed Manifestations of Forces in the Interior of an Electric Conductor," Phys. Rev., **24**, 474, 1907.
7. Kolin, A., "Electromagnetic Flowmeter: Principle of Method and its Application to Blood Flow Measurements," Proc. Soc. Exptl. Biol. and Med., **35**, 53-57, 1936.
8. Shercliff, J. A., The Theory of Electromagnetic Flow-Measurement, Cambridge University Press, London, 1962.
9. Jackson, W. D., "The Electromagnetic Flowmeter," Ph.D. Thesis, University of Glasgow, 1960.
10. Chubb, L. W., United States Patent Specification 1,298,664, April 1919.
11. Einstein, A., and Szilard, L., British Patent Application 303,065, December 24, 1928; British Patent Specification 344,881, March 1931.
12. Watt, D. A., "Electromagnetic Pumps for Liquid Metals," Engineering, **181**, 264-268, April 27, 1956.
13. Blake, L. R., "Conduction and Induction Pumps for Liquid Metals," Proc. Inst. Elec. Engrs. (London), **104A**, 49-63, 1957.
14. Woodrow, J., The D-C Electromagnetic Pump for Liquid Metals, A.E.R.E. E/R 452, United Kingdom, 1949.
15. Barnes, A. H., "D-C Electromagnetic Pumps," Nucleonics, **11**, 16-21, 1953.
16. Baker, R. S., Design and Performance of Induction Pump for SRE Moderator System, NAA-SR-MEMO-3295 (rev.), December 20, 1958.
17. Barnes, A. H., Smith, F. M., and Whitham, G. K., Electromagnetic Pumps for Liquid Metals, AECD-3431, July 15, 1949.
18. Watt, D. A., Design of Travelling Field Induction Pumps for Liquid Metals, A.E.R.E. R/M 144, United Kingdom, September 1957.
19. Applied Magneto-hydrodynamics, Transactions of the Institute of Physics of the Latvian Academy of Sciences, Vol. VIII, 1956; or AEC-tr-3602, United States Atomic Energy Commission, April 1959.
20. Problems of Magnetohydrodynamics and Plasma Dynamics, Proceedings of the Conference on Magnetohydrodynamics, Riga, July 2-10, 1958; or AEC-tr-4509, United States Atomic Energy Commission, September 1961.
21. Grindell, A. G., Performance Characteristics for a GE G-3 Electromagnetic Pump, Y-F17-9, United States Atomic Energy Commission, October 24, 1951.
22. "British Thomson-Houston Electromagnetic Pumps for Liquid Metals," Engineer, **201**, 409, April 27, 1956.
23. Okhremenko, N. M., "Magnetohydrodynamic Effects in Induction Pumps for Liquid Metals," Izvestiya Vysshikh Uchebnykh Zavedenii, Electromekhanika (Bulletin of Higher Educational Institutions, Electromechanics), **6**, 593-601, 1962; translated by Faraday Translations, New York.

24. Harris, L. P., Hydromagnetic Channel Flows, John Wiley and Sons, Inc., New York, 1960, Chapters 8 and 9.
25. Penhune, J. P., Energy Conversion in Laminar Magnetohydrodynamic Channel Flow, ASD Technical Report 61-294, Research Laboratory of Electronics, M.I.T., Cambridge, Massachusetts, August 1961.
26. Reid, M. H., "Experimental Investigation of a Liquid Metal Induction Generator," S.M. Thesis, Department of Electrical Engineering, M.I.T., Cambridge, Massachusetts, September 1963.
27. Hoag, E. D., "Progress Report on Induction Driven Plasma Pump," Internal Memorandum No. 56, Energy Conversion Group, M.I.T., August 1961.
28. Porter, R. P., "A Coil System for an MHD Induction Generator," S.M. Thesis, Department of Electrical Engineering, M.I.T., Cambridge, Massachusetts, May 1965.
29. Jackson, W. D., and Pierson, E. S., "Operating Characteristics of the M.P.D. Induction Generator," Magnetoplasma-dynamic Electrical Power Generation, I.E.E. Conference Report Series No. 4, 1963.
30. Fishbeck, K. H., "On The Theory of AC Induction Plasma Motors and Generators," Ph.D. Thesis, Department of Electrical Engineering, University of Pennsylvania, Philadelphia, Pennsylvania, June 1961.
31. Fanucci, J. B., et al., Electrodeless MHD Generator Research, Part I: Theoretical Analysis, ASD-TDR-62-411, Part I, Radio Corporation of America, Moorestown, New Jersey, October 1962.
32. Electrodeless MHD Generator Research, Part II: Laboratory Facility and Experimental Results, ASD-TDR-62-411, Part II, Radio Corporation of America, Moorestown, New Jersey, March 1963.
33. Lyons, J. M., and Turcotte, D. L., A Study of Magnetohydrodynamic Induction Devices, AFOSR 1864, Graduate School of Aeronautical Engineering, Cornell University, Ithaca, New York, February 1962.
34. Sudan, R. N., "Interaction of a Conducting Fluid Stream with a Traveling Wave of Magnetic Field of Finite Extension," J. Appl. Phys., **34**, 641-650, 1963.
35. Peschka, W., Kelm, S., and Engeln, F., "Penetration Effects at the MHD Induction Engine of Semi-Infinite Length," International Symposium on Magnetohydrodynamic Electrical Power Generation, Paris, July 1964.
36. Neuringer, J. L., and Migotsky, E., "Skin Effect in Magneto-Fluid Dynamic Traveling Wave Devices," Phys. Fluids, **6**, 1164-1168, 1963.
37. Lengyel, L. L., The Analysis of a Vortex Type Magnetohydrodynamic Induction Generator, Technical Report A-10, Case Institute of Technology, October 1962.
38. White, D. C., and Woodson, H. H., op. cit., Chapter 10.
39. Stratton, J. A., Electromagnetic Theory, McGraw-Hill Book Company, Inc., New York, 1941, p. 23.
40. Fano, R. M., Chu, L. J., and Adler, R. B. Electromagnetic Fields, Energy, and Forces, John Wiley and Sons, Inc., New York, 1960, Chapters 7 and 8.
41. Fitzgerald, A. E., and Kingsley, C., op. cit., p. 20, pp. 295-299, p. 466.
42. Fano, R. M., Chu, L. J., and Adler, R. B., op. cit., Section 4.7.
43. Penhune, J. P., op. cit., p. 84-90.
44. Ibid., p. 88.
45. Ibid., pp. 50-52.
46. Ibid., pp. 75-78.
47. Harris, L. P., op. cit., p. 13.

48. Schlichting, H., Boundary Layer Theory, McGraw-Hill Book Co., Inc., New York, 1960, pp. 504-505.
49. Gebhart, B., Heat Transfer, McGraw-Hill Book Co., Inc., New York, 1961, p. 159.
50. Moody, L. F., "Friction Factors for Pipe Flow," Trans. Amer. Soc. Mech. Engs., 66, 671, 1944.
51. Schlichting, H., op. cit., p. 507.
52. Murgatroyd, W., "Experiments on Magneto-Hydrodynamic Channel Flow," Phil. Mag., 44, 1348-1354, 1953.
53. Harris, L. P., op. cit.
54. Hartmann, J., and Lazarus, F., "Hg-Dynamics II" Kgl. Danske Videnskab Selskab, Mat.-fys. Medd., 15, 7, 1937.
55. Harris, L. P., "Hydromagnetic Channel Flows," Sc.D. Thesis, Department of Electrical Engineering, M.I.T., Cambridge, Massachusetts, June 1959, p. 71.
56. Brouillette, E. C., and Lykoudis, P. S., Measurements of Skin Friction for Turbulent Magnetofluidmechanic Channel Flow, Report No. A and ES 62-10, School of Aeronautical and Engineering Sciences, Purdue University, 1962.
57. Schlichting, H., op. cit., pp. 238-243.
58. Ibid., loc. cit.
59. Moffatt, W. C., Boundary Layer Effects in Magnetohydrodynamic Flows, Report No. 61-4, Magnetogasdynamics Laboratory, Dept. of Mechanical Engineering, M.I.T., 1961.
60. Schlichting, H., op. cit., p. 126.
61. Ibid., pp. 534-539.
62. Ibid., p. 539.
63. Fanucci, J. B., Kijewski, L. J., Ness, N., and McCune, J. E., "Fringing Effects in an A.C. MHD Generator," Third Symposium on the Engineering Aspects of Magnetohydrodynamics, Rochester, March 1962; or see reference 31, Chapter 5.
64. Bernstein, I. B., et al., "An Electrodeless MHD Generator," in Engineering Aspects of Magnetohydrodynamics, Columbia University Press, 1962, p. 255.
65. Carpetis, C., Kelm, S., and Peschka, W., "Self-Excitation of an AC MPD Generator," International Symposium on Magnetohydrodynamic Electrical Power Generation, Paris, July 1964.
66. Hildebrand, F. B., Introduction to Numerical Analysis, McGraw-Hill Book Co., Inc., New York, 1956, p. 447.
67. Kantrowitz, A., and Sporn, P., "Magnetohydrodynamics - Future Power Process?," Power, 103, 62, 1959.
68. Gunson, W. E., Smith, E. E., Tsu, T. C., and Wright, J. H., "MHD Power Conversion," Nucleonics, 21, 43, 1963.
69. Brown, G. A., Jackson, W. D., Lee, K. S. and Reid, M. H., "MHD Power Generation with Liquid Metals," Fifth Symposium on the Engineering Aspects of Magnetohydrodynamics, Cambridge, April 1964.
70. Elliott, D. G., "Two-Fluid Magnetohydrodynamic Cycle for Nuclear-Electric Power Conversion," ARS Journal, 32, 924, 1962.
71. Liquid Metals Handbook - Sodium (NaK) Supplement, Jackson, C. B., Ed.-in-Chief, Atomic Energy Commission and the Bureau of Ships, United States Navy, 1956.
72. Woodson, H. H., "Magnetohydrodynamic A-C Power Generation," Pacific Energy Conversion Conference Proceedings, Berkeley, California, August 1962.

73. Adler, R. B., Chu, L. J., and Fano, R. M., Electromagnetic Energy Transmission and Radiation, John Wiley and Sons, Inc., New York, 1960, p. 433.
74. "Armco Hot-Rolled Electrical Steels," Armco Steel Corporation, Middletown, Ohio, 1961.
75. Fanucci, J. B., et al., op. cit., Chapter 4.
76. Poduska, J. W., "Random Theory of Turbulence," Sc.D. Thesis, Department of Electrical Engineering, M.I.T., Cambridge, Massachusetts, September 1962.
77. Stratton, J. A., op. cit., p. 188-192.
78. Morse, P. M., and Feshbach, H., Methods of Theoretical Physics, Vol. 1, McGraw-Hill Book Co., Inc., New York, 1953, p. 210.
79. Schlichting, H., op. cit., p. 515.
80. Ibid., pp. 504, 515, 521, 528.
81. Harris, L. P., op. cit., p. 55.
82. Hildebrand, F. B., op. cit., Chapter 6.
83. Ibid., pp. 64-68.
84. Ibid., pp. 202-208.
85. Ibid., pp. 71-76.
86. Churchill, R. V., Operational Mathematics, 2nd Ed., McGraw-Hill Book Co., Inc., New York, 1958, p. 201-206.
87. Carslaw, H. S., and Jaeger, J. C., Operational Methods in Applied Mathematics, Oxford University Press, London, 1951, p. 94-96.
88. Pierson, E. S., and Jackson, W. D., "Channel Wall Limitations in the MHD Induction Generator," ANL-7148, Argonne National Laboratory, Argonne, Illinois, 1966.

UNCLASSIFIED

Security Classification

DOCUMENT CONTROL DATA - R&D		
(Security classification of title, body of abstract and indexing annotation must be entered when the overall report is classified)		
1. ORIGINATING ACTIVITY (Corporate author) Massachusetts Institute of Technology Research Laboratory of Electronics Cambridge, Massachusetts		2a. REPORT SECURITY CLASSIFICATION Unclassified
		2b. GROUP None
3. REPORT TITLE The MHD Induction Machine		
4. DESCRIPTIVE NOTES (Type of report and inclusive dates) Technical Report		
5. AUTHOR(S) (Last name, first name, initial) Pierson, Edward S. and Jackson, William D.		
6. REPORT DATE May 1966	7a. TOTAL NO. OF PAGES 171	7b. NO. OF REFS 88
8a. CONTRACT OR GRANT NO. AF 33(615)-1083	9a. ORIGINATOR'S REPORT NUMBER(S) AFAPL-TR-65-107	
b. PROJECT NO. 5350		
c. Task No. 535004	9b. OTHER REPORT NO(S) (Any other numbers that may be assigned this report)	
10. AVAILABILITY/LIMITATION NOTICES This document is subject to special export controls and each transmittal to foreign governments may be made only with the prior approval of the Aerospace Power Division, Air Force Aero Propulsion Division, Wright-Patterson Air Force Base, Ohio.		
11. SUPPLEMENTARY NOTES Distribution limited (U.S. Export Control Act of 1949(63STAT 7), as amended (50USC APP 2020.2031), as implemented by AFR 400-10).		12. SPONSORING MILITARY ACTIVITY Air Force Aero Propulsion Laboratory Research and Technology Division Air Force Systems Command Wright-Patterson Air Force Base, Ohio
13. ABSTRACT <p>The magnetohydrodynamic (MHD) induction machine is analyzed to determine the terminal properties, the power flow relations, and the steady-state performance characteristics. The theory for a machine of infinite length and width is first developed, including velocity-profile effects. Solutions are obtained for laminar (Hartmann) flow in a narrow channel, and numerical results are presented for the arbitrary-channel case. Turbulent flow is treated by using a boundary-layer theory. The influence of finite length on generator performance is also considered. In each case considered, results are presented in terms of the electrical efficiency and the power density.</p> <p>The performance and design implications of the results are discussed for several examples of MHD induction generators operated on liquid-metal flows. We conclude that over-all efficiencies in the range 70-85% may be attained in practical high-power generators, but that it may not be possible to achieve the lower efficiency limit at power levels below approximately 1 megawatt.</p>		

DD FORM 1473
1 JAN 64

UNCLASSIFIED

Security Classification

UNCLASSIFIED

Security Classification

14. KEY WORDS	LINK A		LINK B		LINK C	
	ROLE	WT	ROLE	WT	ROLE	WT
	Induction Machine Magnetohydrodynamics Energy Conversion Space Power Systems					

INSTRUCTIONS

1. ORIGINATING ACTIVITY: Enter the name and address of the contractor, subcontractor, grantee, Department of Defense activity or other organization (corporate author) issuing the report.

2a. REPORT SECURITY CLASSIFICATION: Enter the overall security classification of the report. Indicate whether "Restricted Data" is included. Marking is to be in accordance with appropriate security regulations.

2b. GROUP: Automatic downgrading is specified in DoD Directive 5200.10 and Armed Forces Industrial Manual. Enter the group number. Also, when applicable, show that optional markings have been used for Group 3 and Group 4 as authorized.

3. REPORT TITLE: Enter the complete report title in all capital letters. Titles in all cases should be unclassified. If a meaningful title cannot be selected without classification, show title classification in all capitals in parenthesis immediately following the title.

4. DESCRIPTIVE NOTES: If appropriate, enter the type of report, e.g., interim, progress, summary, annual, or final. Give the inclusive dates when a specific reporting period is covered.

5. AUTHOR(S): Enter the name(s) of author(s) as shown on or in the report. Enter last name, first name, middle initial. If military, show rank and branch of service. The name of the principal author is an absolute minimum requirement.

6. REPORT DATE: Enter the date of the report as day, month, year, or month, year. If more than one date appears on the report, use date of publication.

7a. TOTAL NUMBER OF PAGES: The total page count should follow normal pagination procedures, i.e., enter the number of pages containing information.

7b. NUMBER OF REFERENCES: Enter the total number of references cited in the report.

8a. CONTRACT OR GRANT NUMBER: If appropriate, enter the applicable number of the contract or grant under which the report was written.

8b, 8c, & 8d. PROJECT NUMBER: Enter the appropriate military department identification, such as project number, subproject number, system numbers, task number, etc.

9a. ORIGINATOR'S REPORT NUMBER(S): Enter the official report number by which the document will be identified and controlled by the originating activity. This number must be unique to this report.

9b. OTHER REPORT NUMBER(S): If the report has been assigned any other report numbers (either by the originator or by the sponsor), also enter this number(s).

10. AVAILABILITY/LIMITATION NOTICES: Enter any limitations on further dissemination of the report, other than those

imposed by security classification, using standard statements such as:

- (1) "Qualified requesters may obtain copies of this report from DDC."
- (2) "Foreign announcement and dissemination of this report by DDC is not authorized."
- (3) "U. S. Government agencies may obtain copies of this report directly from DDC. Other qualified DDC users shall request through _____."
- (4) "U. S. military agencies may obtain copies of this report directly from DDC. Other qualified users shall request through _____."
- (5) "All distribution of this report is controlled. Qualified DDC users shall request through _____."

If the report has been furnished to the Office of Technical Services, Department of Commerce, for sale to the public, indicate this fact and enter the price, if known.

11. SUPPLEMENTARY NOTES: Use for additional explanatory notes.

12. SPONSORING MILITARY ACTIVITY: Enter the name of the departmental project office or laboratory sponsoring (paying for) the research and development. Include address.

13. ABSTRACT: Enter an abstract giving a brief and factual summary of the document indicative of the report, even though it may also appear elsewhere in the body of the technical report. If additional space is required, a continuation sheet shall be attached.

It is highly desirable that the abstract of classified reports be unclassified. Each paragraph of the abstract shall end with an indication of the military security classification of the information in the paragraph, represented as (TS), (S), (C), or (U).

There is no limitation on the length of the abstract. However, the suggested length is from 150 to 225 words.

14. KEY WORDS: Key words are technically meaningful terms or short phrases that characterize a report and may be used as index entries for cataloging the report. Key words must be selected so that no security classification is required. Identifiers, such as equipment model designation, trade name, military project code name, geographic location, may be used as key words but will be followed by an indication of technical context. The assignment of links, rules, and weights is optional.

UNCLASSIFIED

Security Classification